NOAA Technical Memorandum ERL PMEL-84

A MULTIPLY-CONNECTED CHANNEL MODEL OF TIDES AND TIDAL CURRENTS IN PUGET SOUND, WASHINGTON AND A COMPARISON WITH UPDATED OBSERVATIONS

J.W. Lavelle
H.O. Mofjeld
E. Lempriere-Doggett
G.A. Cannon
D.J. Pashinski
E.D. Cokelet
L. Lytle

S. Gill

NOAA National Ocean Service, Sea and Lake Levels Branch
Rockville, Maryland

Pacific Marine Environmental Laboratory
Seattle, Washington
November 1988

UNITED STATES
DEPARTMENT OF COMMERCE

C.William Verity
Secretary

NATIONAL OCEANIC AND
ATMOSPHERIC ADMINISTRATION

William E. Evans
Under Secretary for Oceans
and Atmosphere/Administrator

Environmental Research
Laboratories

Vernon E. Derr,
Director

NOTICE

Mention of a commercial company or product does not constitute an endorsement by NOAA/ERL. Use of information from this publication concerning proprietary products or the tests of such products for publicity or advertising purposes is not authorized.

Contribution No. 967 from NOAA/Pacific Marine Environmental Laboratory

For sale by the National Technical Information Service, 5285 Port Royal Road
Springfield, VA 22161

CONTENTS

A Multiply-Connected Channel Model of Tides and Tidal Currents in Puget Sound, Washington and a Comparison with Updated Observations

J.W. Lavelle[1], H.O. Mofjeld[1], E. Lempriere-Doggett[1], G.A. Cannon[1], D.J. Pashinski[1], E.D. Cokelet[1], L. Lytle[1] and S. Gill[2]

ABSTRACT. Tides and tidal transports within Puget Sound have been calculated using a model in which the Sound is represented by 79 channels connected at 43 junctions. Linearized equations of motion were used to determine channel cross-sectionally averaged quantities for the principal tidal constituents (M_2, K_1, S_2, N_2, O_1, P_1, M_4). For the M_2 tide the amplitudes and phases at the entrances to the Sound and the friction coefficients in the channels were adjusted to bring observed and modeled tidal distributions into best agreement; for other constituents, only the tidal amplitudes and phases at the entrances were adjusted. Data from 47 tide stations in Puget Sound were used for fitting model parameters. Tidal amplitudes and phases match observations with an average difference of less than 1 cm and 2° respectively for each of the constituents indicated. Transport values from the model were subsequently compared to transports calculated from currents measured on four sections across the Sound at both M_2 and K_1 frequencies. Tidal transports at the M_2 frequency match the transports calculated from the data with average difference of less than 3% for amplitude and 4.3° for phase. The model was also used to calculate cross-sectionally averaged tidal currents, tidal prisms, and tidal dissipation rates for the composite tide and for constituents. As an example of those results, the composite tide and the M_2 and K_1 constituents have tidal prisms of 7.69, 4.74 and 3.73 km^3 and dissipation rates of 733, 528 and 78 MW, respectively.

1. INTRODUCTION

Puget Sound (Fig. 1), a glacially carved estuary, is a network of deep channels. The Sound extends from its principal entrance at Admiralty Inlet into a main basin and three major sub-basins: Hood Canal, Whidbey basin, and the southern basin. A second, but smaller entrance to the system is Deception Pass at the northern end of Whidbey basin. A third, but negligible entrance for the purposes of these calculations is Swinomish Channel. The Sound is connected through its entrances to the Straits of Juan de Fuca-Georgia, a system studied by Redfield (1950). A description of tides and tidal currents in the overall region is given by Mofjeld and Larsen (1984). The distribution of tides and tidal currents specifically within Puget Sound is the subject of this report.

Tides in the Sound are of a mixed, semidiurnal type with large tidal ranges and in some channels rather large currents. Tides are characterized by rapid changes of amplitude and phases in the narrower, shallower, dissipative reaches and slowly changing amplitudes and phases in the deeper, broader regions. Diurnal tidal ranges of 2.6, 3.4, and 4.4 m occur at Port Townsend,

[1] NOAA/Pacific Marine Environmental Laboratory, 7600 Sand Point Way NE, Seattle, WA 98115-0070.

[2] NOAA/National Ocean Service, Sea and Lake Levels Branch, 6001 Executive Blvd., Rockville, MD 20852.

Seattle, and Olympia, respectively (Mofjeld and Larsen, 1984). The amplitude amplification of the M_2 tide between Admiralty Inlet (Port Townsend) and southern basin (Olympia) is ~220%. Tidal current amplitudes are a function of the tidal prism landward of a point of interest and of the channel cross-sectional area. Tidal currents in the main basin, a region with depths of 200 m or more, are typically less than 0.25 m/s. Tidal currents in Admiralty Inlet and in The Narrows, regions with depths of 40-80 m, can be as large as 2.2 and 3.3 m/s, respectively (NOAA, 1984).

Though there have been many observations of tides and tidal currents in the Sound (see, for example, Mofjeld and Larsen, 1984), theoretical descriptions have not been given commensurate effort. The geographical complexity of the system stymies analytical and dictates numerical descriptions. Bauer (1928) first noted that tides in Puget Sound consist of nearly standing waves. Others (University of Washington, 1954) theorized that Whidbey basin increases the effective length of the main basin for tidal waves. The few numerical treatments of tides in Puget Sound have generally been empirical in nature (Pease, 1980) or have described only limited regions of the system. Jamart and Winter (1978) using a vertically-integrated, finite-element, harmonic decomposition model examined tidal motions in northern Hood Canal. More recently Jamart (1983) used the same model to study flow in East Passage around the once favored location of a sewage outfall at Three Tree Point. Roberts (1980) modeled vertically-averaged flow in the Nisqually reach near Olympia. Tidal flow off Seattle, in East Passage, and around Vashon Island has been studied in two and three dimensions by Liou *et al.* (1988) and Chu *et al.* (1988). Several unpublished efforts have also been directed at understanding flow in localized regions: Whidbey basin, Everett Harbor, Budd Inlet, and off Duwamish Head near Seattle. Physical model studies of tidal motions over the whole of the Sound (McGary and Lincoln, 1977) and in Commencement Bay and The Narrows (Ebbesmeyer *et al.*, 1986) complement these approaches.

Only two attempts have been made to study tidal flow over the entire Sound numerically. Schmalz (1986) used a vertically-averaged, two-dimensional, non-linear, barotropic model. More recent work with a three-dimensional model by Nakata (personal communication) has begun to identify tidal eddies within Admiralty Inlet and elsewhere. Sound-wide models generally allow only a few days of simulation, however, because of the large number of grid points and the necessarily short time step for integration. The economics of running time-dependent free-surface-wave models for geographically complex, deep estuaries has been one reason for the paucity of numerical models of Puget Sound.

In this work, tides and tidal transports for the entire Sound are examined numerically. The approach avoids the large number of computational cells by treating Puget Sound not in two dimensions, but as a network of one-dimensional channels. The approach also obviates the need for short computational time steps by linearizing the equations of motion. This allows Fourier decomposition of the equations of motion into ordinary, time-independent differential equations for the tidal amplitude and transport at each tidal frequency. The result is an efficient model of

tides, tidal transports, and cross-sectionally averaged tidal currents throughout the region and one that can serve as the basis for understanding its tidal dynamics.

The price paid for the economy of a network channel model is that description of some aspects of tidal flow in the Sound must be forsaken. By virtue of the model's one-dimensional nature, these include: cross-channel variations of tides and tidal currents (e.g. Jamart, 1983), tidal eddies generated at promontories (e.g. McGary and Lincoln, 1977; Nakata, personal communication), and vertical tidal current shear (e.g. Mofjeld and Lavelle, 1984; Mofjeld and Larsen, 1984). Within the context of a one-dimensional model, the neglect of the convective acceleration term in the momentum equation and the linearization of friction also preclude results on tidal residual currents. Ignoring convective accelerations is not likely to degrade model results at tidal frequencies, however, because horizontal tidal current amplitude gradients are small with respect to tidal frequencies for most reaches of Puget Sound. The linearization of friction is also likely of little consequence for flow at tidal frequencies because the channels of Puget Sound are deep. In his vertically-averaged two-dimensional model of the Straits of Juan de Fuca-Georgia, Crean (1978) reported no discernible differences in results between linearized and quadratic friction parameterizations.

2. MODEL DESCRIPTION

Linearized equations of mass and momentum conservation for cross-sectionally averaged variables are:

$$b\frac{\partial \eta}{\partial t} + \frac{\partial U}{\partial x} = 0 \tag{1}$$

$$\frac{\partial U}{\partial t} + gA\frac{\partial \eta}{\partial x} + \frac{r}{h}U = 0 \tag{2}$$

where b is the channel width, η is the tidal height, t is the time, x is the along-channel coordinate (positive seaward), U is the tidal transport, g is the acceleration of gravity, A is the cross-sectional area of the channel, r is a friction coefficient, and h is the channel depth. The characteristics of the channel (A, b, h, r) can vary along the channel, though in the application to be described r will be constant along each channel. Because the equations of motion are linear in η and U, the full solution may be found by summing solutions for each constituent frequency. For a single frequency, ω, let:

$$\eta = \overline{\eta}(x)e^{-i\omega t} \tag{3}$$

$$U = \overline{U}(x)^{-i\omega t} \tag{4}$$

where i is the usual complex-algebraic constant ($i = \sqrt{-1}$). The understanding in this and follow-

ing equations is that the actual solution consists only of the real part of the final complex-algebraic expression. Substituting Eqs. 3 and 4 into Eqs. 1 and 2 result in:

$$-i\omega b\overline{\eta} + \frac{d\overline{U}}{dx} = 0 \tag{5}$$

$$-i\omega\overline{U} + gA\frac{d\overline{\eta}}{dx} + \frac{r}{h}\overline{U} = 0 \tag{6}$$

Thus at each given frequency of motion, the down-channel dependence of the amplitude, $\overline{\eta}$, and the transport, $\overline{U}$, are related through ordinary differential equations. The general solution in each channel is the sum of two independent solutions:

$$\overline{\eta} = B\overline{\eta}_B(x) + C\overline{\eta}_C(x) \tag{7}$$
$$\overline{U} = B\overline{U}_B(x) + C\overline{U}_C(x) \tag{8}$$

where B and C are complex-algebraic amplitude coefficients. The coefficients are determined by two boundary conditions.

When the channel characteristics (A, b, h, and r) vary along the channel, Eqs. 5 and 6 must be solved numerically for $\overline{\eta}$ and $\overline{U}$. Numerical integration proceeds by center differencing:

$$\overline{U}_{i+1} = \overline{U}_i + i\omega(b_i + b_{i+1})\Delta x_i\overline{\eta}_i/2 \tag{9}$$
$$\overline{\eta}_{i+1} = \overline{\eta}_i + (\Delta x_i + \Delta x_{i+1})(i\omega - r_i/h_i)\overline{U}/(2gA_i) \tag{10}$$

$\overline{\eta}$ and $\overline{U}$ are evaluated on a staggered grid (Fig. 2). Δx_i represents the distance between transport lines $\overline{U}_i$ and $\overline{U}_{i+1}$, and the channel parameters (A_i, b_i, h_i, and r_i) are evaluated at the $\overline{U}_i$ positions. The index increases in the seaward direction.

Independent solutions are derived using Eqs. 9 and 10 by imposing two (independent) sets of conditions at the landward end of the channel:

$$\overline{\eta}_B(0) = (1.0, 0.0) \text{ and } \overline{U}_B(0) = (0.0, 0.0), \; x = 0 \tag{11}$$
$$\overline{\eta}_C(0) = (0.0, 0.0) \text{ and } \overline{U}_C(0) = (1.0, 0.0), \; x = 0 \tag{12}$$

where complex-algebraic notation is used for the constants. The $\overline{\eta}$ and $\overline{U}$ of each independent solution are one-dimensional arrays. The length of the arrays corresponds to the number of transects along the channel for $\overline{U}$; the $\overline{\eta}$ array has one additional element.

Suppose now that Puget Sound were represented by a network of N one-dimensional channels. Each would have its own particular solution pair ($\overline{\eta}_B$, $\overline{U}_B$) and ($\overline{\eta}_C$, $\overline{U}_C$) and each would have two yet unspecified complex coefficients B and C. *En toto*, 2N complex-algebraic

coefficients (B_j, C_j, j = 1,2....N) need to be constrained by boundary conditions before the entire general solution can be determined.

Most of the constraints occur at channel junctions. There two conditions must be satisfied. First, the tidal amplitudes of all waves entering a common junction must be equal. Let J represent the set of channel indices common to the junction. Then, conditions on the set of general solutions are of the form:

$$\overline{\eta}^i_\ell = \overline{\eta}^j_\ell \tag{13}$$

for all i and j pairs contained in J, where the subscript ℓ indicates a value of $\overline{\eta}$ at a terminus of a channel (a junction center). At any junction the number of constraints is equal to the number of channels entering the junction less one.

Second, the instantaneous transport in and out of the junction must sum to the instantaneous increase of fluid stored within the junction. Thus:

$$\sum_{i\varepsilon J} U^i_\ell e^{-i\omega t} = \tilde{A}\,\frac{\partial \eta}{\partial t} \tag{14}$$

where the summation is made for all i contained in J, $\tilde{A}$ is the surface area of the junction, and where ℓ indicates the $\overline{U}^i$ value through the transect forming one side of the junction. Substituting for η using Eq. 3 results in:

$$\sum_{i\varepsilon J} \overline{U}^i_\ell = i\omega\tilde{A}\overline{\eta} \tag{15}$$

summed over all i contained in J. One such equation for every junction provides additional constraints on the set of solution coefficients (B_j and C_j, j = 1,N).

The remaining conditions come at the open and closed ends of channels not connected to a junction. At open boundaries, complex-algebraic numbers representing the amplitudes and phases of the tides must be specified. At closed boundaries, i.e. the closed end of terminal channels, the transport is specified as zero (or a given constant if riverine input enters there).

These conditions constitute 2N complex linear equations relating the 2N complex amplitude coefficients. The set of equations can be solved numerically by standard algebraic methods. For large N, however, the high rank on the equation matrix requires high numerical precision. Once the complex amplitudes are determined, however, the tidal amplitudes and transports can be evaluated for each channel using the independent solutions for that channel (Eqs. 7 and 8).

Besides the tides and tidal transports, several derived quantities are also useful in characterizing the motion. Cross-sectionally averaged tidal velocities are simply the tidal transports

divided by cross-sectional areas. The tidal prism, P, for an individual tidal constituent is the amount of water stored in the network landward of the evaluation point between low and high tide. Thus:

$$P = \int_0^{T/2} \mathrm{Re}(\overline{U})\, dt = T|\,\overline{U}\,|/\pi \qquad (16)$$

where T is the tidal period and Re denotes the real part of the expression. The average volume flux of water, Q, passing a point is the tidal prism landward of that point divided by the interval of accumulation of that prism. Hence, $Q = 2P/T = 2|\overline{U}|/\pi$.

The tidal prism of the complete tide, the sum of the constituent tides, is not so easily defined. In the model application to be described, seven amplitude and phase pairs at the network entrances will be derived by fitting model results to seven observed tidal distributions (M_2, N_2, S_2, K_1, O_1, P_1, M_4; Table 1). Entrance amplitudes and phases for 14 additional tidal constituents ($2Q_1$, Q_1, ρ, M_1, J_1, OO_1, $2N_2$, μ_2, ν_2, λ_2, L_2, T_2, R_2, K_2) are then determined from the seven using the equilibrium tide relationships between major and minor constituents (Schureman, 1958). Distributions of the minor constituents through all channels can then be evaluated. Tides and tidal transports for 20 constituents (M_4 not included) will then be summed at any time t to create the instantaneous tidal distribution of what will hereafter be called the composite tide.

TABLE 1. Model tidal amplitudes and phases at entrances to Puget Sound. Phases are Greenwich phase lags.

Tide	Frequency (cycles/day)	McCurdy Pt.-Pt. Partridge Transect (Admiralty Inlet)		Rosario Head-West Point* (Deception Pass)	
		Amplitude (m)	Phase (degrees)	Amplitude (m)	Phase (degrees)
M_2	1.93227	0.604	341.76	0.944	18.07
K_1	1.00274	0.728	269.00	0.82	279.0
S_2	2.00000	0.139	4.99	0.235	43.50
N_2	1.89598	0.120	314.19	0.196	346.30
O_1	0.92954	0.407	247.50	0.45	256.60
P_1	0.99726	0.241	267.00	0.271	277.32
M_4	3.86455	0.025	81.00	**	**

* Model is unable to reproduce steep amplitude and phase gradients through Deception Pass. These amplitudes and phases are more representative of those of Yokeko Point just to the east of Deception Pass (three model segments from entrance).

** Model uses zero transport through Deception Pass for M_4.

The tidal prism of the composite tide is based on a time average of the differences in the incoming and outgoing volume transported through a model transect. A time series of volume transported is first created by analytically integrating the composite tidal transport over time. 19-year averages of all maximum incoming volumes transported and 19-year averages of the daily maximum outgoing volume transported are then calculated. The difference in the two means is defined to be the tidal prism of the model composite tide. These results will be compared to tidal prisms that are based on areal integrals of over 57 subregions of Puget Sound of the difference between mean high water and mean lower low water.

The instantaneous rate of energy input into the system, F_e, is (Proudman, 1953; Gill, 1982):

$$F_e = \rho g \mathrm{Re}(U)\mathrm{Re}(\eta) \tag{17}$$

where ρ is the density of water. The time average rate of dissipation of energy, $\langle F_e \rangle$, in the system landward of a model transect is:

$$\langle F_e \rangle = \frac{\rho g}{T} \int_0^T \mathrm{Re}(U)\,\mathrm{Re}(\eta)\,dt \tag{18}$$

which for an individual constituent of period T is:

$$\langle F_e \rangle = \rho g \mathrm{Re}(\overline{U}/\overline{\eta})\,|\overline{\eta}|^2/2 \tag{19}$$

The energy flux of the composite tide is calculated using Eq. 18 when the tidal height and transport are those of the composite tide and the average is over a 19-year period.

3. MODEL APPLICATION TO PUGET SOUND

Puget Sound has been represented as a network of 79 channels and 43 junctions (Fig. 3). Channels were segmented into sections having an average length of 1.4 km. On each of 589 transects (Fig. 3, solid lines) channel widths and depths were specified. At these locations the channel cross-section was assumed to be rectangular. Tidal transport was calculated at the segments, and tidal heights were calculated at midpoints between segments and within the junction regions (solid areas, Fig. 3).

Most channel widths and average depths at transects (Fig. 3) were evaluated using shoreline and bathymetric databases to be described in detail elsewhere; for some areas of Hood Canal, channel widths and depths were taken from NOAA charts. The shoreline database is a digital representation of the mean lower low water datum as specified on NOAA navigational charts of Puget Sound. The bathymetric database consists of a compilation of over 1.2 million

bathymetric soundings within the Sound and vicinity taken in NOAA hydrographic surveys. These data were gridded onto areas 250×250 m, data within each grid element carefully screened for outlying points, and an average depth within each grid element was then calculated.

Both databases were simultaneously accessed and transect endpoints selected from an interactive graphics display. Transect widths were based on a Cartesian distance between transect end points as represented on an oblique azimuthal stereographic map projection. Bathymetric grid elements through which the transect traversed were then used to compute the maximum depth, the transect cross-sectional area, and an average depth. Junction centers were visually determined also from the interactive graphics display.

Once these transect and junction data were assembled, only segment lengths, junction areas, and friction coefficients needed to be specified. Lengths between segments (Δx, Fig. 2) were specified as the distance between the midpoints of neighboring transects. Segment lengths at ends of channels entering junctions (Fig. 2) were based on the normal distance between the transect and junction centers. Junction areas were defined by connecting the endpoints of the channel transects that border the junction. Each polygon thus formed was divided into quadrilateral areas. The area of each junction, $\tilde{A}$, was calculated by summing the component quadrilateral areas.

An attempt was made to use as few frictional parameters as possible. Thus, the friction coefficients, r_i, were made constant within each channel. Additionally, friction coefficients for all channels in the network were assigned a nominal value of 2×10^{-3} m/s, a value in the range found for coastal flow in four separate experiments (0.3 to 2.1×10^{-3} m/s; Winant and Beardsley, 1979). In some channels (e.g. Admiralty Inlet, The Narrows) the friction coefficients were adjusted upward by factors of 2-3 (Table 2) to give a good fit of the model results to the observed

TABLE 2. Friction coefficients in channels named. All other channels have friction coefficients of 2.0×10^{-3} m/s.

Channel Name	Friction Coefficient (m/s) $\times 10^{-3}$
Admiralty Inlet North	4.5
Admiralty Inlet South	4.5
Bush Point	4.5
Mutiny Bay	4.5
Deception Pass	5.0
Dyes Inlet	5.0
The Narrows	6.0
Nisqually	5.0
Rich Passage	5.0
Dana Passage	5.0

tidal heights. It is no surprise that friction should be higher in Admiralty Inlet and The Narrows because currents are strong there and current shear is significant over a sizeable fraction of the water column (Mofjeld and Lavelle, 1984; Mofjeld and Larsen, 1984).

The absolute value of these friction coefficients range from reasonable to somewhat high. Consider the approximate relationship between the bottom drag coefficient, C_d, and the friction coefficient, r, for a pure oscillatory flow: $r = 8C_d\langle u\rangle/(3\pi)$ (e.g. Dronkers, 1964). If $\langle u\rangle$ is nominally 1 m/s, and r has a value of 5×10^{-3} m/s, then C_d has a magnitude of $\sim 6 \times 10^{-3}$. For high velocity channels like Admiralty Inlet and The Narrows such a value for the C_d is not unreasonable. On the other hand, for lower velocity regions like the main basin where $\langle u\rangle$ is more like 0.2 m/s, a value of r of 2×10^{-3} m/s requires a C_d value of $\sim 1 \times 10^{-2}$. This value for the drag coefficient is 4-5 times that normally expected, though Crean (1978) was forced to use a drag coefficient, C_d, of 3×10^{-2} for the narrow passages of his two-dimensional model of the Straits of Juan de Fuca-Georgia system. Redfield (1950) also noted usually strong dissipation in discussing the same system. Causes of enhanced frictional resistance in the system can only be speculated upon.

The final values for the friction parameters were fixed using an intercomparison of M_2 tidal amplitudes and phases for model results and observations, changing as few friction coefficients from the 2.0×10^{-3} m/s value as necessary. Subsequently, six additional tide and transport distributions were calculated adjusting only the incident amplitudes and phases at Admiralty Inlet and Deception Pass to give the best correspondence between model and data distributions (Table 1). In the case of the M_4 tide, for which few data values are available in the area of Deception Pass, tidal calculations were made as if Deception Pass were closed to flow. Because of the relatively small tidal prism contributed to Whidbey basin by Deception Pass, M_4 regional distribution should be only slightly affected.

Tidal amplitudes and phases, tidal transports and their phases, and cross-sectionally averaged tidal velocities for each of nearly 600 segments were thus calculated at seven tidal frequencies. Results in tabular form are available from the authors. Some of the more important results are described below.

4. OBSERVATIONAL CONSIDERATIONS

The tides in Puget Sound have been observed over a relatively dense array (Fig. 4; Table 3) of 51 stations from surveys by the National Ocean Service and the Pacific Marine Environmental Laboratory. For the present study, the observed tidal harmonic constants were either obtained from the literature, from databases of harmonic constants or computed through tidal analysis of existing data sets (see Table 4 for sources). When using the observed harmonic constants to calibrate and test the model, it is important to have estimates of the accuracy, or conversely the

TABLE 3. Latitude and longitude for stations depicted in Figure 4.

Station	Latitude (N)	Longitude (W)	Station	Latitude (N)	Longitude (W)
0000	47° 36.0'	122° 20.0'	6281	47° 23.0'	122° 49.4'
10	48° 8.0'	122° 46.0'	6451	47° 18.1'	122° 40.9'
11	48° 6.8'	122° 45.0'	6486	47° 16.3'	122° 33.1'
12	48° 9.5'	122° 40.1'	6500	47° 16.5'	122° 45.5'
13	48° 17.0'	122° 43.7'	6539	47° 15.4'	122° 38.9'
20	48° 24.9'	122° 39.1'	6545	47° 15.3'	122° 25.9'
21	48° 24.4'	122° 38.5'	6800	47° 8.5'	122° 54.2'
22	48° 25.0'	122° 37.0'	6828	47° 7.1'	122° 39.9'
165	47° 37.0'	122° 40.0'	6969	47° 3.0'	122° 54.0'
178	47° 13.0'	123° 5.0'	7265	47° 41.3'	122° 23.7'
5016	47° 55.6'	122° 37.0'	7427	47° 48.8'	122° 23.0'
5059	47° 51.5'	122° 34.8'	7659	47° 58.8'	122° 13.4'
5088	47° 48.9'	122° 39.4'	7814	47° 56.4'	122° 21.4'
5246	47° 45.7'	122° 51.0'	7854	48° 2.0'	122° 36.2'
5269	47° 42.7'	122° 49.3'	7881	48° 5.9'	122° 31.2'
5293	47° 39.9'	122° 54.7'	7952	48° 17.2'	122° 37.0'
5296	47° 38.5'	122° 49.6'	PS8000	47° 35.8'	122° 24.0'
5441	47° 25.1'	122° 54.0'	8094	48° 8.2'	122° 22.0'
5478	47° 21.5'	123° 5.9'	PS8313	47° 27.0'	122° 26.3'
5526	47° 55.1'	122° 32.7'	PS8314	47° 26.5'	122° 22.5'
5639	47° 47.8'	122° 29.6'	PS8315	47° 20.6'	122° 27.1'
5717	47° 43.5'	122° 38.3'	PS8316	47° 19.3'	122° 25.7'
5958	47° 33.7'	122° 37.4'	PS8317	47° 25.7'	122° 31.8'
6025	47° 30.7'	122° 27.8'	PS8318	47° 25.4'	122° 30.8'
6248	47° 24.0'	122° 19.7'	8558	48° 23.5'	122° 29.8'
6254	47° 23.7'	122° 27.8'			

uncertainty, of the constants. A number of factors affect the accuracy including the accuracy of the tidal analyses, conversion factors from bottom pressure to equivalent sea level height for bottom pressure measurements, noise at tidal frequencies and calibration and time base accuracy. The most reliable harmonic constants can be expected from long time series. For Puget Sound, these are from the NOS reference stations (Fig. 4) at Seattle (Station No. 0000), Port Townsend (Station Nos. 10 and 11) and Yokeko Point (Station No. 22), all of which allowed 369-day harmonic analyses and from the PMEL bottom pressure stations in the southern main basin which allowed 233 to 291-day response analyses. The rest of the observed tidal harmonic constants generally come from 29-day harmonic analyses of relatively short time series (Table 4). Averages were taken where more than one analysis was available for a station.

To estimate the uncertainties in the observed tidal harmonic constants as functions of the method of analysis and series length, it is convenient to focus on observed harmonic constants

TABLE 4. Sources of observed tidal harmonic constants used for calibrating and evaluating the model. The observations were taken over a variety of periods since 1898.

Stations [Years]	Type	General Locations	Method of Analysis	Sources
0000 [1921-1939]	Tide	Seattle Reference Station	Average of 19 369-day harmonic analysis	Zetler, Long, and Ku (1985)
5016, etc. (4 digits) [various]	Tide	Throughout Puget Sound	29-day harmonic analyses with minor corrections for short analysis biases	NOS Database
PS8000 [1980]	Pressure	Elliott Bay	29-day harmonic analysis; Unit conversion factor from pressure to tidal amplitude	PMEL Database
PS8313, etc. (PS + 4 digits) [1983-1984]	Pressure	southern main basin	233 to 291-day Response analyses (except 85-day for PS8313) with 3 weights and the tidal potential as the reference series; Unit conversion factor from pressure to tidal amplitude	PMEL Database
10, etc. (2 digits) [various]	Tide	northern Puget Sound, Strait of Juan de Fuca	369-day harmonic analyses for 10, 11, 22; 29-day harmonic analyses for 12, 13, 20, 21	Parker (1977)
165 178 [unknown]	Tide	Dyes Inlet Oakland Bay	Not Given	UW (1954) Mofjeld & Larsen (1984)

NOS = National Ocean Service
PMEL = Pacific Marine Environmental Laboratory
UW = University of Washington

from a representative bottom pressure station: PS8314. A comparison (Table 5) of harmonic constants from response and harmonic analyses (see Pugh, 1987, for a general description of the analysis methods) at PS8314 shows that the difference between the means of the M_2 and K_1 harmonic constants derived from successive 29-day harmonic analyses and those of the full-length response analyses is small compared with the standard deviations. This lack of bias is in contrast to those reported by Parker (1977) for the nearby Straits of Juan de Fuca-Georgia. Biases do occur in the inferred harmonic constants (obtained from amplitude ratios and phase differences of directly observed constants) in the 29-day harmonic analysis because of equilibrium assumptions in the harmonic analysis method (Schureman, 1958); a comparison of equilibrium and observed amplitude ratio for Puget Sound is given by Mofjeld and Larsen (1984). In the present study, no bias correction in the inferred constituents (e.g. P_1) obtained from 29-day harmonic analyses because the biases are relatively small compared with other sources of error.

A major source of error of tidal harmonic constants are fluctuations at tidal frequencies due to non-tidal processes such as internal waves and meteorological forcing. They introduce an uncertainty in the harmonic constants that can be estimated from a standard deviation σ_r for a given (i.e., diurnal or semidiurnal) tidal band that is derived from the ratio μ of the residual variance V_{res} left in the band after tidal analysis to the observed variance V_{obs} in that band. Following Mofjeld and Wimbush (1977),

$$\sigma_r = [\mu L_o/2L]^{1/2} \quad , \quad \mu = V_{res}/V_{obs} \tag{20}$$

where σ_r is the ratio of the amplitude standard deviation to the amplitude as well as the standard deviation in radians of the phase lag, L is the series length in days, and $L_o = 27.55$ days. For data taken at PS8314, this line of analysis shows that the standard deviations estimated from the reductions in variance are comparable with those derived from the scatter of results from the set of 29-day harmonic analyses (Table 5).

For bottom pressure series, an additional uncertainty arises from the conversion factor β that must be applied to convert bottom pressure (p) to equivalent sea surface elevation (η) where $\eta = \beta p$. Assuming the hydrostatic approximation, this factor is given by

$$\beta = 1/\rho g \tag{21}$$

where g is the regional acceleration of gravity (9.8073 m/s^2) and ρ is the mean density of the water above the pressure gage. While the density was not monitored during the pressure gage deployments, its mean value and variation can be estimated from the climatological range of surface density of 1.019 to 1.023 kg/m^3 since the gages were deployed in shallow water (<15 m). This range of density leads to a conversion factor β of essentially unity (0.999 ± 0.002 m/Pa).

TABLE 5. Estimates of uncertainties in M_2 and K_1 tidal harmonic constants obtained from tidal analyses of a 252-day bottom pressure series at PS8314 (47° 26.5'N, 122° 22.5'W) in the southern main basin. The standard deviations σ of the response analysis come from a full-length analysis series using three weights (0, ±48 hr) and the tidal potential as the reference series (e.g. Pugh, 1987). The standard deviations σ for the 29-day harmonic analyses come from the scatter of harmonic constants from 15 overlapping analyses (successive start times every 15 days); the standard deviations σ' are averages of the individual standard deviations for each harmonic analysis as are the amplitudes and phase lags.

Observed M_2 Tide at PS8314

	Amplitude H (m)	Standard Dev. σ (m)	Standard Dev. σ' (m)	Phase Lag G (deg)	Standard Dev. σ (deg)	Standard Dev. σ' (deg)
Response	1.081	0.015	-----	11.5	0.8	----
Harmonic	1.078	0.008	0.027	11.5	0.6	1.4

Observed K_1 Tide at PS8314

	Amplitude H (m)	Standard Dev. σ (m)	Standard Dev. σ' (m)	Phase Lag G (deg)	Standard Dev. σ (deg)	Standard Dev. σ' (deg)
Response	0.820	0.012	-----	278.3	0.9	----
Harmonic	0.827	0.037	0.030	278.0	1.5	2.1

The uncertainty in the value of β produces uncertainty in tidal amplitude estimates from pressure gage data that are a factor of five less than the sum of those from other sources.

Broader estimates of the uncertainties in the observed tidal harmonic constants associated with different series lengths and analysis methods can be found by focusing on the suite of M_2 and K_1 tides observed at stations in the southern main basin where the tides are nearly uniform in amplitude and phase. These estimates (Table 6) also provide a check on the general effects of uncertainty in calibration and time base. For the M_2 amplitude the standard deviations are about 0.02 to 0.03 m whether estimated from the reductions in variance (Eq. 20) or computed from the scatter of observations in the region although the latter is enhanced by the southerly increase in M_2 amplitude (Table 6). The M_2 phase standard deviations is about 1° and shows no regional trend. The amplitude standard deviations (0.008 to 0.02 m) for the K_1 tide (Table 6) are

TABLE 6. Variations of M_2 and K_1 tidal harmonic constants at stations (Fig. 4) in the southern main basin where the standard deviations σ come from the full-length response analyses using three weights and the tidal potential as the reference series (e.g. Pugh, 1987). Harmonic constants without standard deviations come from harmonic analyses. The differences ΔH and ΔG are between individual amplitudes and phase lags and the regional averages. Information about the observations are given in Table 4.

Observed M_2 Tide in the Southern Main Basin

Station	Length (days)	Amplitude H (m)	St. Dev. σ (m)	Diff. ΔH (m)	Phase Lag G (deg)	St. Dev. σ (deg)	Diff. ΔG (deg)
0000	369	1.070	-----	−0.026	11.5	-----	−0.4
PS8000	29	1.086	0.044	−0.010	13.2	2.3	1.3
6025	29	1.090	[0.027]*	−0.006	10.9	[1.4]*	−1.0
PS8313	84	1.075	0.022	−0.021	11.9	1.2	0.0
PS8314	252	1.081	0.015	−0.015	11.5	0.8	−0.4
PS8317	237	1.090	0.015	−0.006	10.9	0.7	−1.0
PS8318	237	1.091	0.016	−0.005	12.9	0.8	1.0
6248	29	1.118	[0.027]*	0.022	12.5	[1.4]*	0.6
PS8315	233	1.114	0.016	0.018	11.2	0.8	−0.7
PS8316	252	1.107	0.016	0.011	11.5	0.8	−0.4
PS8409	291	1.098	0.014	0.002	11.6	0.7	−0.3
6545	29	1.133	[0.027]*	0.037	13.0	[1.4]*	1.1
Mean		1.096	0.020 [0.022]**	0.019***	11.9	0.8 [1.1]**	1.0**

Observed K_1 Tide in the Southern Main Basin

Station	Length (days)	Amplitude H (m)	St. Dev. σ (m)	Diff. ΔH (m)	Phase Lag G (deg)	St. Dev. σ (deg)	Diff. ΔG (deg)
0000	369	0.831	-----	0.005	277.3	-----	−0.5
PS8000	29	0.841	0.032	0.015	276.5	2.2	−1.3
6025	29	0.823	[0.030]*	−0.003	277.9	[2.1]*	0.1
PS8313	84	0.836	0.020	0.010	278.9	1.3	1.1
PS8314	252	0.820	0.012	−0.006	278.3	0.9	0.5
PS8317	237	0.815	0.013	−0.011	277.6	0.9	−0.2
PS8318	237	0.814	0.013	−0.012	278.8	0.9	1.0
6248	29	0.825	[0.030]*	−0.001	276.8	[2.1]*	−1.0
PS8315	233	0.824	0.012	−0.002	278.2	0.8	0.4
PS8316	252	0.824	0.012	−0.002	278.0	0.9	0.2
PS8409	291	0.832	0.011	0.006	277.3	0.8	−0.5
6545	29	0.834	[0.030]*	0.008	278.0	[2.1]*	0.2
Mean		0.826	0.016 [0.020]**	0.008***	277.8	1.1 [1.4]**	0.7**

* Standard deviations σ′ based on 29-day harmonic analyses at PS8314 (Table 5)
** Mean standard deviations including estimates from 29-day harmonic analyses
*** Standard deviations of the differences from the regional mean

somewhat less than those for M_2, while the K_1 phase standard deviation is comparable (~1°) with that for M_2. The largest standard deviations (0.03 for amplitude and 1.4° to 2° in phase lag) occur for harmonic constants derived from individual 29-day harmonic analysis. The smaller observed harmonic constants can be expected to have comparable uncertainties in amplitude but larger uncertainties in phase lag assuming the intensity of the noise is uniform within each tidal band. For inferred constituents such as P_1, estimates can be found for the standard deviations by assuming the same fractional amplitude and phase standard deviations as those for the observed constituents from which the inferred harmonic constants are derived.

When studying the response of a region to tidal forcing, it is often helpful to examine the variations of the tidal behavior within each of the major tidal bands. A convenient quantity that characterizes this behavior is the tidal admittance. The admittance amplitude at the frequency of a given tidal constituent is the ratio of the observed tidal amplitude to that of a reference tidal signal at the same frequency, and the admittance phase is the difference between the observed phase and that of the reference. The concept of a continuously varying admittance within each tidal band is fundamental to the response method of tidal analysis. When the reference is the tidal potential, a unit admittance amplitude and zero admittance phase indicates that the response is the same as the equilibrium tide. While the equilibrium tide in general differs substantially from those observed in the ocean, it provides a useful standard for comparison. In the discussion of tides in Puget Sound, it is convenient to focus on the tidal admittances at PS8314 because they are typical of those in Puget Sound away from its entrances and because the reliability of the observed PS8314 tidal harmonic constants have been treated above in some detail.

In the semidiurnal band, the admittance amplitudes are large compared with the equilibrium tide in the middle and lower ranges of frequency (Fig. 5). The relatively constant admittance amplitude between N_2 and M_2 frequencies is consistent with the near-equilibrium N_2/M_2 amplitude ratio (Table 7). The admittance amplitude decreases above the M_2 frequency to the sub-equilibrium S_2 amplitude typical of the relatively small S_2 in the North Pacific region. Because there is little tidal energy at the low frequency end of the semidiurnal band to guide the analysis, the rise in admittance amplitude below the N_2 frequency is probably created artificially by the response analysis method, which generates divergent admittances at the ends of the tidal bands when more than one weight is used in a given tidal band. There is the usual increase in semidiurnal admittance phase lag with a progressively decreasing slope of the phase lag curve toward the high frequency end of the semidiurnal band.

In the diurnal tidal band, the admittance amplitudes at PS8314 (Fig. 5) are larger than equilibrium values and increase strongly with increasing frequency as expected from the West Coast of North America where typical O_1/K_1 amplitude ratios (Table 7) are less than the equilibrium ratio. The increase in diurnal phase lag with frequency also reflects the diurnal relationships of the incoming tidal waves from the Pacific Ocean. The minimum admittance phase lag

TABLE 7. Tidal amplitude ratios and coefficients in linear phase formulas at PS8314 (47° 26.5'N, 122° 22.5'W) from a full-length 252-day response analysis (three weights, 0, ±48 hr with the tidal potential as the reference series), averages of nineteen 369-day harmonic analyses at Seattle (Zetler *et al.*, 1985) where ratios are obtained directly from the observations, equilibrium ratios from the tidal potential and phase coefficients based solely on frequency differences (Schureman, 1958). Also shown are tidal harmonic constants at PS8314; negative phase lags are used so that the phases are continuous through 0° as required by the phase formulas.

Semidiurnal Tides

	Amp. (m)	Phase Lag (°G)		Amplitude Ratio PS8314	Seattle	Equil.	Phase Coefficient a,b* PS8314	Seattle	Freq.
$2N_2$	0.0340	−58.7	$2N_2/N_2$	0.166	0.133	0.133	−2.257	−1.994	−2.000
μ_2	0.0391	−54.0	μ_2/M_2	0.036	0.030	0.024	−3.539	(−6.333)	−2.000
N_2	0.2049	−19.6	N_2/M_2	0.190	0.199	0.194	−1.000	−1.000	−1.000
ν_2	0.0387	−14.5	ν_2/N_2	0.189	0.169	0.194	−0.836	−0.358	−0.866
M_2	1.0807	11.5	-----	-----	-----	-----	0.000	0.000	0.000
L_2	0.0271	28.5	L_2/M_2	0.025	0.046	0.028	0.547	1.607	1.000
T_2	0.0170	36.7	T_2/S_2	0.063	0.059	0.059	−0.023	0.000	−0.040
S_2	0.2715	37.3	S_2/M_2	0.251	0.241	0.465	0.000	0.000	0.000
K_2	0.0632	38.5	K_2/S_2	0.233	0.280	0.272	0.047	−0.049	0.081

* For $2N_2$, N_2, ν_2, M_2 and L_2, $G = G(M_2) + a[G(M_2) - G(N_2)]$;
for μ_2, T_2, S_2 and K_2, $G = G(S_2) + b[G(S_2) - G(M_2)]$

Diurnal Tides

	Amp. (m)	Phase Lag (°G)		Amplitude Ratio PS8314	Seattle	Equil.	Phase Coefficient a** PS8314	Seattle	Freq.
Q_1	0.0675	253.2	Q_1/O_1	0.144	0.164	0.194	−1.073	−1.215	−1.496
O_1	0.4682	254.9	O_1/K_1	0.571	0.552	0.711	−1.000	−1.000	−1.000
M_1	0.0425	264.2	M_1/O_1	0.091	0.085	0.071	−0.603	(0.489)	−0.500
P_1	0.2687	275.9	P_1/K_1	0.328	0.304	0.331	−0.103	−0.123	−0.075
K_1	0.8198	278.3	K_1/M_2	0.759	0.777	0.584	0.000	0.000	0.000
J_1	0.0487	295.4	J_1/O_1	0.104	0.079	0.079	0.731	0.502	0.496
OO_1	0.0289	312.9	OO_1/O_1	0.062	0.043	0.043	1.479	1.000	1.000

** a is the coefficient in the equation $G = G(K_1) + a[G(K_1) - G(O_1)]$

near the low frequency end of the band may be artificial since Q_1 and other nearby minor constituents have little tidal energy to guide the response analysis.

The ratios (Table 7) of tidal amplitudes and the coefficients in the linear phase formulas are often used to infer the harmonic constants for minor tidal constituents in, for instance, the 29-day harmonic analysis. They reflect the behavior of the tidal admittances (Fig. 5) when compared with the equilibrium amplitude ratios and phase coefficients based solely on frequency differences. They are typical of Puget Sound in which, for example, the S_2/M_2 (0.24 to 0.25) and O_1/K_1 (0.54 to 0.58) amplitude ratios are relatively constant over the Sound and where the S_2-N_2 (54.8° to 59.2°) and K_1-O_1 (20.0° to 23.6°) phase differences increase only modestly from Port Townsend to Olympia. The consistency of the semidiurnal ratios and coefficients in Puget Sound is in contrast to amphidromic or nodal systems (areas of small or near-zero amplitude and rapidly changing phases) such as the Straits of Juan de Fuca-Georgia in which a semidiurnal nodal region lies just outside the entrance to Puget Sound.

The differences (Table 7) in phase coefficients between the response analysis and equilibrium values arise because the admittance phase curves (Fig. 5) are not straight lines as assumed in the linear frequency interpolation scheme. The differences are greatest where the inferred constituent (i.e., $2N_2$, μ_2 and Q_1) is well-removed in frequency from the major constituents. This discrepancy should have little effect on the results of the harmonic analyses for the major constituents (O_1, P_1, K_1, N_2, M_2 and S_2) since the interference of these outlying minor constituents on the major constituents is relatively small (Schureman, 1958). The largest inferred constituent, P_1, has essentially the equilibrium ratio relative to K_1 as expected since the proximity of the P_1 frequency (2 cycles per year less) to that of K_1 requires essentially the same response of the ocean to gravitational forcing, and there is no diurnal amphidrome or node in Puget Sound.

One interesting difference occurs for K_2 between the PS8314 and the frequency phase coefficients on the one hand and that for Seattle on the other. Both the PS8314 response analysis and frequency coefficients b are positive (K_2 phase lag greater than that for S_2), but b from the directly observed K_2 tide at Seattle is negative (K_2 phase lag less than that of S_2) implying a negative slope to the phase admittance curve (Fig. 5) at the high frequency end of the semidiurnal band. It is possible that this is the result of the radiational (meteorological) S_2 tide perturbing the gravitational phase curve. By fitting parabolas through observed tidal amplitudes and phase lags of the purely gravitational N_2, M_2 and K_2 constituents, Zetler (1971) finds that the radiational S_2 tidal amplitude for the U.S. West Coast is typically 16% of the gravitational S_2 amplitude with a radiational phase lag 133° less than that of the gravitational S_2 constituent; at Neah Bay at the entrance to the Strait of Juan de Fuca-Georgia, the amplitude ratio (0.20) is slightly larger and phase difference (81°) smaller than the West Coast average (133°). Zelter *et al.* (1985) applied the same parabolic method to the observed tides at Seattle. Their inferred radiational S_2 amplitude of 0.035 m at Seattle gives a radiational-to-gravitational amplitude ratio 0.12 that is

less than the West Coast average (0.16), while the phase difference 154° is larger than the West Coast average (133°) but well within the phase range (81°-180°) reported by Zetler (1971).

5. TIDES

Tidal distributions are the primary data by which the adequacy of the model can be judged. Observed tidal amplitudes and phases for the M_2, K_1, S_2, N_2, O_1, P_1, and M_4 frequencies, given the discussion of accuracy in the previous section, are provided in Figs. 6a,b-12a,b. Corresponding model results for the M_2 and K_1 tides are found in Figs. 6c,d and 7c,d. And differences in model results and observations for both amplitude and phase for all seven tidal constituents are to be found in Figs. 6e,f, 7e,f, 8c,d-12c,d. Model results are given for the model section closest to the actual measurement location. Phases are Greenwich phase lags in degrees.

Observed M_2 tidal distributions (Figs. 6a,b) show amplitudes increasing from 0.65 m at Port Townsend in Admiralty Inlet to values exceeding 1.46 m in the southern basin (excluding Oakland Bay), an increase of 220%. The phase change over the same distance amounts to 40°, Port Townsend having a phase lag of 350°. Gradients in amplitude and phase are largest in these constricted regions of flow: Admiralty Inlet, The Narrows, and Deception Pass. For example, the growth of the M_2 amplitude over Admiralty Inlet amounts to about 0.30 m, and the phase shift is 15-20°, while in The Narrows the amplitude grows by at least 0.10 m and the phase shifts by 10° or more. Even larger changes in amplitude and phase occur at Deception Pass. Note the amplitude change over the northern part of Hood Canal, a silled region of relatively shallow depth.

Large gradients also occur for smaller, narrow and/or shoal channels. For example, the data (Fig. 6b) shows an M_2 phase shift of approximately 28° through Hammersley Inlet leading into Oakland Bay at Shelton. A substantial phase shift and an amplitude increase also occur through Port Washington Narrows into Dyes Inlet. Changes in amplitude and phase in other regions occur more slowly. In a few locations (e.g. Edwards Point, Bush Point, Three Tree Point, Admiralty Head, and in Hood Canal and Colvos Passage), stations are located across channel from one another, permitting examination of the cross-channel variation of the tides. In almost all cases, real differences in tidal amplitude or phase are not resolvable in the cross-channel data.

The model results (Fig. 6c,d) show the same features as the data. This cannot be too surprising in view of the fact that the entrance amplitudes and phases (Table 1) and the friction parameters (for the M_2 constituent only) were adjusted to provide for good agreement. Still the use of a linearized model for the tides in the Sound is vindicated by the very good quantitative agreement between model and data.

The goodness of fit is better judged by diagrams showing the differences in M_2 model results and data (Figs. 6e,f). Over 47 stations the average difference in amplitude and phase

between M_2 model results and observations is 0.007 m and 0.7°, respectively (Table 8), well within the uncertainty limits on the data (Section 4). At the Seattle station, for which the tides are best determined, the differences are on the same order as the average differences. The model replicates the tidal amplitude maximum in Whidbey basin at the Oak Harbor Station. In the southern basin, a bias of 2-3 cm in the amplitude toward larger model results is observable (Fig. 6e). That the amplitude in the southern basin depends strongly on the presence of Whidbey basin, as suggested earlier (University of Washington, 1954), was found to be true in our modeling studies as well. When both Hood Canal and Whidbey basin branches were truncated from the network, the result was much reduced tides in the southern basin.

As is well understood from simpler models, the phase changes along a channel are quite sensitive to the value given the friction coefficient. Phase shifts are greatest in channels of largest friction. The large changes in tidal phase across the sill regions and in other area of the Sound dictated that the friction coefficients in some channels be adjusted upward away from their nominal value of 2.0×10^{-3} m/s as described earlier (Table 2).

One local region in which the correspondence between model and data is unsatisfactory is Deception Pass. The model could not be made to provide the amount of amplitude growth and phase change that is observed across Deception Pass from the western side on the Rosario

TABLE 8. Averages $\bar{x}$ and standard deviations σ for the differences in amplitude and phase between the model results and tidal observations. The number of stations for which the comparisons were made (Figs. 6e,f, 7e,f, 8c,d-12c,d) is represented by n.

Tidal Species	ΔAmp $\bar{x}$ (m)	ΔAmp σ (m)	ΔPhase $\bar{x}$ (deg)	ΔPhase σ (deg)	n
M_2	.007	.025	0.72	2.73	47
N_2	−.004	.026	−0.06	2.03	45
S_2	−.004	.021	1.53	2.41	45
K_1	.001	.013	−0.12	4.52	45
O_1	−.002	.010	1.01	3.96	45
P_1	.001	.013	−0.10	1.90	45
M_4	.005	.011	−0.50	63.22	33

Head-West Point transect (a model entrance) to the eastern side at Yokeko Point. Attempts to provide better resolved bathymetry and cross-sectional areas through the Pass provided no substantial improvement in model results. It thus seems likely that non-linear aspects of the dynamics, which are missing in the model, play a significant role in this limited region.

Because the model did give good results at Yokeko Point and in Whidbey basin with linear dynamics, the model was run with the entrance conditions shown in Table 1, understanding that model tidal distributions from the Rosario Head-West Point transect to Yokeko Point (3 segments) would not well represent the actual data. Only tides and tidal transports at Yokeko Point and landward are regarded as valid estimates of tidal conditions for the Deception Pass region.

At one other site, Dyes Inlet, the model performs poorly by underestimating the amplitude and overestimating the phase changes. This result is most likely caused by poor resolution of channel geometry through Port Washington Narrows, though other causes (e.g. nonlinear dynamics) cannot be ruled out.

Observed K_1 tidal distributions (Figs. 7a,b) show an amplitude change from 0.73 m near Port Townsend to 0.94 m in the southern basin, an increase of nearly 30%, much less than for the M_2 tide. The phase changes over the length of the network are comparably less too: a phase at Port Townsend of 270° and a southern basin phase near 288°. In the other major branches, amplitude and phase changes are small. For example, along Hood Canal the amplitude changes by 3.6%; there is even less amplitude change in the southern part of Whidbey basin to Oak Harbor. As occurs for the M_2 tide, however, the largest gradients in amplitude and phase occur in the regions of more restricted flow. Real cross-channel differences in K_1 tidal amplitude and phase (Fig. 7a,b) are not resolvable with these data, considering the confidence intervals on the K_1 tidal estimates (Section 4).

Model tidal distributions (Figs. 7c,d) well represent the amplitudes and phases of the K_1 tide as shown in the difference distributions (Fig. 7e,f). The average difference between model results and data over 45 stations is 0.001 m in amplitude and −0.1° in phase (Table 8). The match at the Seattle tide station is within this range. A systematic bias in phase of about 2° occurs in the southern basin region with the model phase being smaller than the observed; a systematic basis of about 3°, the model phase being larger, occurs in Hood Canal as well. Friction coefficients were not changed from the values used to fit the M_2 distributions, so the closeness of the K_1 fit despite these slight biases is very good.

Distributions of two other semidiurnal tidal constituents, the S_2 and N_2, show amplitude and phase patterns like those of the M_2 (Figs. 8a,b-9a,b), though the amplitudes are much less and the phases are shifted at the entrances (Table 1). The S_2 amplitude is only 23% and the N_2 amplitude only 20% of the M_2 tidal amplitude near Port Townsend (Table 1). Phases of the S_2 and N_2 at the same location are 5° and 314° rather than the 342° for the M_2. Model and data amplitudes and phases are in good agreement (Figs. 8c,d-9c,d). The average difference between

the model results and the data in amplitude for both the S_2 and N_2 is −0.004 m, while the average differences in phases are 1.5° and −0.1°, respectively (Table 8).

Distributional patterns for two other diurnal constituents, the O_1 and the P_1, follow the K_1 distributions, also with the amplitudes reduced and the phases shifted (Figs. 10a,b-11a,b). The amplitudes of the O_1 and P_1 tides are 56% and 33% of the K_1 amplitude at the Admiralty Inlet entrance to the system (Table 1). Corresponding phases are 247° and 267° rather than 269° for the K_1 tide. The differences between the model results and the data (Figs. 10c,d-11c,d) lead to estimates of average differences in amplitude of −0.002 m and 0.001 m and 1.0 and −0.1° in phase for the O_1 and P_1 results (Table 8).

The M_4 tide, having a frequency twice that of the M_2 tide, has a distribution (Fig. 12a,b) unlike the other constituents previously discussed. Though the amplitude change through Admiralty Inlet is unclear, the data does show an amplitude increase of 100% over the length of Hood Canal. Through The Narrows there appear to be M_4 amplitude increases of over 50% and a phase change of 70° or more. Differences in phase between the main basin and southern basin amount to approximately 100°.

The M_4 tide has been reported at 34 stations (Fig. 12a,b). A comparison of these data with the model output (Fig. 12c,d) show that the model accounts for much of the observed variation in M_4 amplitude and phase. The average difference in amplitude between model results and observations is 16% of the average M_4 amplitude value (Table 8). The median absolute difference between model results and observations for phases is 10.9°. The amplitude of M_4 near the Port Townsend entrance of the model is 0.025 m (Table 1). In order that the model amplitude match exactly the data at the Seattle station, as it does, the M_4 amplitude must decrease into the Sound while the phase is increasing by nearly 115° (Table 1, Fig. 12b). Along Hood Canal the M_4 amplitude nearly doubles, yet there is very little change in phase; the model simulates both amplitude and phase gradients in Hood Canal though a small bias to the predictions is evident in the difference distributions (Fig. 12c,d). The overall similarity between the model and observed M_4 tides in Puget Sound indicates that this tide is a regional wave originating outside the Sound. Though small M_4 tides can be generated locally by M_2 tides near points of land, for example, M_4 tides are not created within the Sound by the model because the model dynamics are linear. The landward increase in M_4 phase lag also indicates a source outside the Sound.

A time series of predicted and observed tides at Station PS8314 (Fig. 13) show the quality of the model results in the time domain. The predicted series is based on six fitted model amplitudes (M_4 not used) and phases at this station plus 14 additional, minor tidal constituents inferred from the model results. The six constituents, however, account for 99% of the variance of the predicted tidal signal. The comparison (Fig. 13) has been made after the observational mean has been adjusted to the model mean over the given time interval by an amount comparable to the sum of the nominal deployment depth and the atmospheric pressure (Table 9; the pressure

TABLE 9. Results of a comparison (Fig. 13) between predicted and observed tides at PS8314 in East Passage. The predictions are based on 20 tidal constituents either obtained directly or inferred from the model. The pressure observations have been converted to equivalent sea level height (m) with an adjustment to the background depth of the observations which produces the same mean level (zero mean difference) as the predictions.

Station:	PS8314 (47° 26.5'N, 122° 22.5'W)
Simulation Period:	0000 GMT 25 February 1983 to 0000 GMT 5 March 1983

Nominal Deployment Depth = 14 m		
Nominal Atmospheric Pressure = 10.0 m		
Depth Offset of Pressure Observations = 23.181 m*		
Standard Deviation of Differences = 0.093 m	(5.4%)**	
Magnitude of Maximum Difference = 0.236 m	(13.7%)**	

* Adjustment for zero mean difference
** Percentage relative to the mean diurnal amplitude 1.72 m (half the diurnal range 3.44 m)

gage measures the sum of the oceanic and atmospheric pressures). The resultant time series match closely both in phase and pattern, though the predictions tend to underestimate slightly the amplitudes of the observations at high and low water. The standard deviation of the difference between the predictions and observations in percent (5.4%) is similar to those of open ocean predictions in which theoretical results have been calibrated with observations at a suite of stations (e.g. Mofjeld, 1975; Schwiderski, 1980).

There are many possible reasons for the model's slight underestimation of the observations at high and low water. One is that the limited number of constituents (20) used in the predictions does not adequately represent the tidal content of the observed signal. A second reason is that those harmonic constants used in the prediction that are inferred from the model-derived constants are not sufficiently accurate because they are based on equilibrium rather than actual relationships between major and minor constituents (Table 7). A third reason is that the constants determined by model fit to the observations are inaccurate because the observational data contain noise. There is a tendency for noise in the observed time series to lead to an underestimation of the coherent tidal signal and hence the observed harmonic constants. It is common for tidal predictions based on harmonic analysis to underestimate high and low water; for this reason, the National Ocean Survey routinely enlarges measured tidal harmonic amplitudes to

obtain harmonic amplitudes for prediction (Zetler *et al.*, 1985). A fourth reason for the model's underestimation of observations at high and low water (Fig. 13) may be that the observed time series contains some non-tidal energy from, for example, meteorological forcing.

6. TIDAL TRANSPORTS

Tidal transport estimates are a second direct product of the model. Figs. 14 and 15 show transport amplitudes and phases for the M_2 and K_1 tides at locations coincident with those of the tidal stations. Transport amplitudes, though posted at station locations, represent the flux of water through a cross-channel transect which has an endpoint nearest the station location. Phases are Greenwich flood lags in degrees.

Amplitudes for the M_2 transport range from 3.29×10^5 m^3/s off Port Townsend in Admiralty Inlet to zero at the end of terminal channels. Transports decrease into the network as a result of the storage of water in the tidal prism seaward of a given point. Transport amplitudes are discontinuous in magnitude at junctions where transport must be distributed among connecting channels. A few peculiar values of transport in Figs. 14 and 15 (e.g. in the vicinity of Port Townsend or at the north end of Vashon Island) are the result of a station location nearest a segment on a minor rather than major channel (Fig. 3).

Figure 14a suggests that M_2 tidal transport into Hood Canal (4.53×10^4 m^3/s) and Whidbey basin (6.38×10^4 m^3/s) represent 14 and 19% of the total M_2 transport at Port Townsend. The M_2 transport through the Narrows (7.24×10^4 m^3/s), 22% of the Port Townsend transport, is 1.6 times that into Hood Canal but only slightly more than that into Whidbey basin. The difference in transport at the northern end of the main basin and The Narrows is indicative of the storage capacity of the main basin for the tides. The M_2 tidal transport is split 1/3 to Colvos Passage and 2/3 to East Passage. Note too that the apparent M_2 tidal transport through Deception Pass as represented by the Yokeko Point flux (2.98×10^3 m^3/s) is only about 5% of the transport that passes into Whidbey basin through Possession Sound.

The phase changes for the model M_2 transport (Fig. 14b) from Admiralty Inlet into southern basin are not nearly as great as for the M_2 tide itself. There is only a 16° phase shift in M_2 transport over that distance compared to the 40° for the M_2 tide. Nor are the gradients in transport phase highest in the sill regions of Admiralty Inlet and The Narrows though changes in phase are substantial in Hammersley Inlet and Port Washington Narrows. The M_2 transport phases in Hood Canal and Whidbey basin lead those of Admiralty Inlet and those in Colvos Passage lead those of East Passage by about 5°.

The amplitude of the K_1 transport (1.33×10^5 m^3/s) is 40% of the M_2 transport at Port Townsend (Fig. 15a). The fraction of the K_1 transport at Port Townsend partitioned to Hood Canal and to Whidbey basin is nearly the same as for the M_2 transport, but the percentage of K_1 flux into the southern basin is less by about 4% for the K_1 than for the M_2 tide. Only 40% of the

volume of the K_1 tide entering the northern main basin passes on to The Narrows. The K_1 transport through Deception Pass is only 2.3% of the K_1 transport coming into Whidbey basin through Possession Sound.

A phase change for the K_1 transport of approximately 11° occurs over the length of the network to the southern basin with slightly larger changes occurring over the short lengths of Hammersley Inlet and Port Washington Narrows (Fig. 15b). As with M_2, the K_1 transport phases in Hood Canal and Whidbey basin lead those in Admiralty Inlet. The phase difference between Colvos Passage and East Passage is accentuated for the K_1 transport, with those in Colvos Passage leading those in East Passage by approximately 11°. The K_1 phase difference in northern Whidbey basin between Oak Harbor and Yokeko Point stations (Fig. 15b) indicates the difference in transport directions.

The accuracy of these tidal transport estimates can be judged by a comparison of these results with transport estimated from data acquired on cross-channel arrays of current meters. Four such transects have been occupied (Fig. 16, Table 10). These are located off Dash Point near Tacoma (Bretschneider *et al.*, 1985), off Three Tree Point in East Passage (Bretschneider *et al.*, 1985), off Meadow Point near Seattle and off Bush Point in Admiralty Inlet (Cannon *et al.*, 1979). The bathymetry across channel and the locations of current meters within each cross-section are found in Figs. 17-24.

Details of the instrumentation and moorings for each cross-section are to be found in the given references (Table 10). Table 10 shows that the records available for analysis ranged from 40 to 102 days in length. The observed current time series were resolved along the axes parallel to the local channel direction and analyzed for harmonic constants using the 29-day harmonic

TABLE 10. Information about the observed current transects and the grid used for the calculation of tidal transports.

Section	Year	Typical Duration (days)	Grid Size Depth (m)	Grid Size Horiz. (m)	References
Bush Pt.	1977	57	10.0	200	Cannon *et al.* (1979)
Meadow Pt.	1985	102	12.5	500	unpublished
Three Tree Pt.	1983	40	12.5	250	Bretschneider *et al.* (1985)
Dash Pt.	1983	42	12.5	125	Bretschneider *et al.* (1985)

method. For the longer time series, averages were taken of results from successive analyses. Small corrections due to short 29-day analysis lengths were ignored in deriving the tidal-current harmonic constants.

At Dash Point 12 current meters on three moorings spanned the channel of 3300 m width. Along-channel M_2 current amplitudes (Fig. 17a) ranged from 12.6 to 18.0 cm/s. A slight intensification of current amplitude occurs toward the southeast side (Dash Point) of the section. Results of the Jamart (1983) model show nearly uniform vertically-averaged currents across the channel at this same location. The effect of a tidal bottom boundary layer is weakly suggested on the Point Piner (NW) side of the cross section. A very thin boundary layer would be reasonable in an area such as this with relatively low velocities and the bottom sediment composed of fine-grained sediments (Roberts, 1974). M_2 current phases (Fig. 17b) show an extraordinary shift of 50° over depth at this location.

K_1 tidal current amplitudes at Dash Point (Fig. 18a) show large vertical changes with the largest currents unexpectedly occurring at depth. Near surface values are 2.6-5.3 cm/s while at depth a maximum current amplitude of 15.8 cm/s occurs. Coincidentally, there is a phase lag increase of over 127° in K_1 currents from the surface to the bottom (Fig. 18b). No explanation for this unusual pattern of K_1 current amplitudes and phases is now available.

At Three Tree Point, 23 current meters were deployed on six moorings across the 4500-m-wide channel. Here M_2 current amplitudes (Fig. 19a) ranged from 7.7 to 28.6 cm/s with very large current amplitude gradients occurring in the cross-channel direction. The amplitudes on the second easternmost mooring near the bottom shows a nearly three-fold increase over the amplitudes measured near the bottom on the neighboring mooring only 650 m farther to the west. This intensification of the M_2 current amplitude at the eastern side of the transect is the result of the narrowing of the channel by the Three Tree Point promontory (Fig. 16). Sediment distribution maps (Roberts, 1974) show a small area of coarse sediment located off Three Tree Point, presumably the result of the winnowing of fine sediments by these currents. This intensification of currents on the east side of the cross-section is identified by Jamart's (1983) vertically-integrated model of tides in East Passage.

The vertical variation of M_2 current amplitudes also show some unusual behavior (Fig. 19a). On the second easternmost mooring, the amplitudes increase toward the bottom, showing no sign of a boundary layer that the moorings to the west weakly suggest. That there should be no evidence of a boundary layer overlying an area of high currents and coarse sediments is a surprise. Note also that current amplitudes measured near the surface at the middle of the array (~12-13 cm/s) are considerably higher than the near-surface amplitudes (~8 cm/s) on neighboring mooring to the east and west position. This difference may reflect in part the along-channel position of the mooring with three near-surface current meters with respect to the position of the remaining moorings. The M_2 current phases at Three Tree Point show primarily

vertical variation (Fig. 19b). The phase decrease with depth of 61° is greater than that measured over depth at Dash Point (50°).

At the Three Tree Point section the maximum K_1 current amplitude (8.1 cm/s, Fig. 20a) is only about half that at Dash Point and, in contrast, the current amplitudes decrease with depth in the water column. The horizontal gradients of the K_1 current amplitude are less than for the M_2, though for both amplitude and phase (Fig. 20) the influence of Three Tree Point on the flow is evident. Phase increases over the water column are less than at Dash Point, the largest change being 51° rather than 126°.

Farther to the north at Meadow Point (Figs. 21-22) where the Sound has a width of 7500 m 24 current meters have provided data that show M_2 current amplitudes ranging from 5.5 to 21.6 cm/s, the extremes being on the east and west of the channel near the surface. A significant vertical variation of M_2 current amplitudes (Fig. 21a) also occurs, some moorings suggesting a bottom boundary layer. The M_2 phase (Fig. 21b) shows far less variation than at the cross-sections to the south. The Meadow Point cross-section occurs at a location where just to the north at the surface the channel broadens in the westerly direction into Port Madison and where the channel at depth turns toward the east. These along-axis geometric/bathymetric changes of the channel undoubtedly cause some of the lateral and vertical variation of M_2 currents observed at this section.

The maximum for the K_1 current amplitude at Meadow Point (Fig. 22a) occurs near the bottom as it does at Dash Point. Phase differences for the K_1 currents over the section are greater than 60° (Fig. 22b), in contrast to the M_2 current phase variation of only 10°.

In Admiralty Inlet off Bush Point where the channel has a width of approximately 4600 m the cross-channel array consisted of nine meters on three moorings (Figs. 23-24). Here the measured M_2 current amplitudes (Fig. 23a) range from 60.6 to 100.1 cm/s. Though there are fewer current meters to resolve the cross-sectional variations, the data suggests only slight cross-channel variation of M_2 current amplitudes. The sizeable decrease in M_2 current amplitudes toward the bottom, on the other hand, suggests a thick boundary layer as discussed by Mofjeld and Lavelle (1984) who analyzed data from the central mooring. M_2 current phase variation (Fig. 23b) is about 14° over the vertical and is consistent with the idea that the entire water column is a boundary layer for the M_2 tidal currents (Mofjeld and Lavelle, 1984).

The K_1 current amplitudes at Bush Point (Fig. 24a) are large in comparison to those measured at the other three cross-sections (Fig. 18a, 20a, 22a). Here they range in magnitude from 25.3 to 44.7 cm/s, while K_1 current phase shifts (Fig. 24b) of up to 29° occur. Lateral variations are as significant as vertical variations for both K_1 current amplitude and phase. The decrease in K_1 current amplitudes with depth is consistent with the idea of a boundary layer of thickness comparable to the depth of the water.

Given these measured current amplitudes and phases, transports at M_2 and K_1 frequencies through each of the four cross-sections were computed in the following way. The M_2 and K_1 current amplitudes and Greenwich phase lags coming from the analysis of data from each meter were transformed into in-phase and out-of-phase components. These components were then interpolated onto uniform grids of horizontal and vertical size as given in Table 10, using a combination of Laplacian and spline interpolation schemes. Each resultant grid of values was integrated numerically over each cross section. The integrals of the in-phase and out-of-phase transports were then recombined into estimates of observed tidal transport amplitudes and phases (Table 11). Model transports through transects (Fig. 3) most closely located to the current meter transects (Fig. 16) are also given in Table 11.

TABLE 11. Comparison of M_2 and K_1 transports from the model with estimates from cross-channel sections of observed tidal currents.

M_2 Transport

Section	Amplitude			Flood Phase Lag			
	Model (10^3 m^3/s)	Observed (10^3 m^3/s)	Diff. (%)	Model (°G)	Observed (°G)	Diff. (°)	Direction (°T)
Bush Pt.	314.6	311.2	1.1	285.1	287.6	−2.5	181
Meadow Pt.	144.6	132.5	8.4	290.1	303.8	−13.6	191
Three Tree Pt.	76.8	76.9	−0.6	294.0	291.8	2.2	160
Dash Pt.	63.1	61.9	1.8	296.6	299.7	−3.1	233

K_1 Transport

Section	Amplitude			Flood Phase Lag			
	Model (10^3 m^3/s)	Observed (10^3 m^3/s)	Diff. (%)	Model (°G)	Observed (°G)	Diff. (°)	Direction (°T)
Bush Pt.	125.3	119.6	4.6	188.7	190.5	−1.8	181
Meadow Pt.	53.1	47.4	10.7	190.8	200.6	−9.8	191
Three Tree Pt.	27.4	27.4	−0.1	194.3	182.7	11.6	160
Dash Pt.	21.9	24.4	−11.7	196.0	179.6	16.4	233

Table 11 shows that observed M_2 transport amplitudes range from 311×10^3 m^3/s off Bush Point to 61.9×10^3 m^3/s off Dash Point, values resembling the model estimates to within an average percentage difference over the four cross-sections of 2.7%. The good correspondence of model and measured M_2 transport amplitudes is the result of transport depending only on the tidal prism landward of a section. As long as the model reasonably approximates tidal heights and phases as it does, then tidal transport should also be well described. Observed and modeled M_2 transport phase lags are also in good agreement except for the Meadow Point station. The irregular progression of observed M_2 transport phase lags from Bush to Dash Points at Meadow Point (Table 11) is enigmatic. A careful investigation of possible sources of error in the data and analyses for the Meadow Point station that might result in such phase progression revealed no assignable reasons for it.

The correspondence between model and measured transports for the K_1 tide is less satisfactory. Though the average difference in K_1 amplitudes between model and measured results is about 1%, the differences range from −11.7 to +10.7% over the four transects. Furthermore, there appears to be fundamental difference in the down-axis pattern of transport phases between model and observations for the K_1 component. From the model, the phase progression is toward later phase from Bush to Dash Points. The cross-sectionally averaged K_1 phases from the current data show the opposite trend. The measured Meadow Point phase is anomalous in the down-channel trend of phases (Table 11) at the K_1 frequency, as it was for the M_2.

7. TIDAL CURRENTS

Cross-sectionally averaged tidal currents can be calculated by dividing model transports by cross-sectional areas. The results can usefully show the along-channel variations of tidal current amplitudes that result from changes in channel cross-section, but the results provide no information on lateral and vertical variations of currents that the data (Section 6) have shown to exist.

In Figs. 25-27 the amplitudes and phases for the M_2, K_1, and M_4 tides (dashed lines) and their cross-sectionally averaged currents (solid lines) are plotted against distance down the center of Puget Sound. Distance is measured from the McCurdy Pt. – Pt. Partridge transect (Admiralty Inlet entrance of the model) down the center of each channel through Admiralty Inlet, the main basin including East Passage, The Narrows, Nisqually reach, Dana Passage, along Squaxin Island, through Hammersley Inlet, and into Oakland Bay. The total distance is just over 200 km.

Fig. 25a shows the high variability of M_2 current amplitudes with distance into the estuary. Cross-sectional variations create amplitude changes of almost a factor of 2 over short (< 10 km) distances in the Admiralty Inlet region. More exaggerated changes of amplitude occur in the Hammersley Inlet region. M_2 currents exceed 1 m/s over a distance of more than 7 km in The Narrows. The smallest M_2 current amplitude outside of the southern basin occurs at the junction of Whidbey basin with the main basin. Phase changes are gradual for the M_2 currents except at

the entrance to Hammersley Inlet (Fig. 25b). M_2 tidal amplitudes and phases (dashed lines, Fig. 25) have their largest gradients in the regions of constricted flow as previously discussed.

The K_1 current amplitudes (Fig. 26a) have a down-channel pattern much like the M_2, though the amplitudes are also reduced in size. The maximum current amplitude is 0.63 m/s in Hammersley Inlet. Tidal current phases (Fig. 26b), on the other hand, are much more discontinuous than those for M_2. The K_1 current phase jumps by several degrees toward later phase at the northern end of East Passage but sheds most of that phase gain at the entrance to The Narrows. A noticeable decrease in the phase occurs in the region of complex channel connections just outside of Hammersley Inlet, a region of rapid K_1 phase change (Fig. 26b). The K_1 tidal amplitude and phase gradients (dashed lines, Fig. 26) are smaller than for M_2, but the patterns of change are similar.

M_4 tidal current amplitudes (Fig. 27a), though having the same qualitative nature as the M_2, have much smaller amplitudes in Admiralty Inlet relative to the rest of the distribution than does the M_2. M_4 current amplitudes are generally less than 0.05 m/s except in The Narrows and in Hammersley Inlet. The M_4 current phases (Fig. 27b) range from -60 to $+100°$, a range much larger than for the M_2 current phase (50°). Large changes in phase occur at the junctions of Hood Canal and Whidbey basin with the main basin.

The M_4 tidal amplitude distribution (dashed line, Fig. 27a) demonstrates a minimum within Admiralty Inlet. The amplitude increases by a factor of three through The Narrows and southern basin. Absolute values for amplitude are always less than 0.07 m. The tidal phase (dashed line, Fig. 27b), ranging from about 80 to nearly 300° excluding Hammersley Inlet, shows the largest gradients in the constricted flow regions. The minimum in amplitude in Admiralty Inlet and the phase change over the length of the network of about 220° may indicate that Puget Sound is not far from resonance for the M_4 tide.

The total tides and tidal currents in Puget Sound are sums of contributions from the individual tidal constituents. These composites form characteristic patterns in time series that are determined by the relative amplitudes and phase lags of the harmonic constants. The examples in Figs. 28 and 29 show typical patterns in 1988 for the tides and tidal currents in Admiralty Inlet near the main entrance to Puget Sound (Port Townsend) and in the central main basin off Seattle (Alki Point). The time series were generated by a tidal prediction program that uses 20 harmonic constants obtained either directly or by inference from the model distributions as previously explained (Schureman, 1958); the tidal current is cross-sectionally averaged. As shown by Schureman (1958), the year 1988 corresponds to a time in the 18.6-year cycle of the lunar orbit when the nodal modulation of the semidiurnal lunar (e.g., N_2 and M_2) tidal forcing is at its minimum (3.6% less than the mean) while the diurnal lunar (e.g., O_1 and the lunar component of K_1) forcing is at its maximum (18.1% greater than the mean for O_1 and 11.1% greater for K_1).

The relative influence of the diurnal tides and tidal currents during 1988 is therefore somewhat enhanced over their average contribution to the total tidal motions.

The January 1988 period follows shortly after the winter solstice when new and full moon occur at nearly the same time as that for maximum declination of the sun and moon (solstitial tides), while April follows the vernal equinox when the moon and sun are very near the equator (zero declination) at new and full moon (equinoctal tides). These differences in the relative phases of the diurnal and semidiurnal forcing produce different tidal patterns. The January tides at Port Townsend (Fig. 28a) and off Seattle (Fig. 28b) have strong fortnightly (every two weeks) modulations caused primarily by the fortnightly variations in the diurnal forcing and to a lesser extent by the more monthly variations in the semidiurnal forcing (see Mofjeld and Larsen, 1984, for a detailed description of the tide and tide current characteristics in the Puget Sound region and their relationship to the tidal forcing).

The tide at Port Townsend (Fig. 28a) is near the semidiurnal nodal region in the eastern Strait of Juan de Fuca (Parker, 1977; Mofjeld and Larsen, 1984) and is therefore dominated by the diurnal tide (Table 12), especially the solstitial tides (Fig. 28a) and to a lesser extent during the equinoctal period (Fig. 29a) when the neap tides are semidiurnal. The tide off Seattle (Fig. 28b) is mixed-semidiurnal (Table 12) due to the comparable magnitudes of the composite diurnal and semidiurnal amplitudes. In general the Alki Point (Seattle) tide is larger in magnitude than the Port Townsend tide primarily due to the southward growth of the amplitudes of the semidiurnal tidal constituents.

The diurnal pattern of tides in Puget Sound during large ranges (i.e., periods of constructive interference between M_2, K_1 and O_1) characteristically have two nearly equal high waters where the higher high water usually precedes lower high water (more pronounced at Seattle where the sequence of tides is 199°) and two very different low waters in which lower low water follows immediately after lower high water. The January tidal ranges are larger than those in April because of coinciding spring (large semidiurnal) and tropic (large diurnal) tides during the solstitial period that are one week out of phase during the equinoctal period.

The tidal currents (Figs. 28 and 29) in Puget Sound are much more semidiurnal than the tides because the semidiurnal currents have nearly twice the amplitude of the diurnal currents (Table 12). This is consistent with the nearly equal diurnal and semidiurnal tidal amplitudes because the semidiurnal currents, which have half the period, must flow twice as strong to generate a tidal prism (and hence a tide) comparable with that of the lower frequency diurnal tides. The tidal currents in Admiralty Inlet (Figs. 28a and 29a) are strong because almost all the tidal prism for the large tides occurring in Puget Sound must flow through the inlet which is relatively shallow compared with the landward regions. The much smaller current amplitudes (Figs. 28b and 29b) off Seattle are due to the relatively large depth and width and to the smaller tidal prism to the south. Consistent with the tides, the solstitial January currents (Figs. 28a and

TABLE 12. Tidal characteristics from model results at transects off Port Townsend in Admiralty Inlet and off Seattle in the main basin. Mean ranges and current amplitudes are based on 19-year predictions over the epoch 1969 to 1988.

Transect Properties	Port Townsend	Seattle
Width (km)	6.01	7.48
Maximum Depth (m)	93.2	319.3
Mean Depth (m)	52.6	125.4
Cross-Sectional Area (m^2)	3.16×10^5	9.39×10^5

Tides	Port Townsend	Seattle
Type of Tide*	1.44	0.97
Sequence of Tide**	190°	199°
Mean Tidal Range (m)	1.59	2.32
Diurnal Range (m)	2.65	3.44

Tidal Currents	Port Townsend	Seattle
Type of Current*	0.49	0.43
Sequence of Current**	290°	291°
Mean Maximum Current Speeds		
Flood (m/s)	1.36	0.175
Ebb (m/s)	1.43	0.184

* Ratio of amplitudes $\frac{K_1 + O_1}{M_2 + S_2}$

** Phase lag difference (flood phases for currents) $M_2^\circ - K_1^\circ - O_1^\circ$

28b) are stronger than the equinoctal April currents as are the inequalities between flood and ebb currents. The sequences of tidal current (Table 12) at Port Townsend and Seattle indicate that the tidal currents have essentially equal flood and ebb inequalities with somewhat larger ebb inequalities.

In The Narrows the model currents (not shown) have essentially the same patterns (sequence of current equal to 292°) as those in Admiralty Inlet and off Seattle (Figs. 28-29) with maximum speeds somewhat larger than those in Admiralty Inlet. This similarity in the patterns is not seen in near-bottom observations reported by Mofjeld and Larsen (1984) in which the sequence of current (343°) indicates nearly equal flood currents but strongly unequal ebbs. The differences between the cross-sectionally averaged model currents and the near-bottom observations suggests that there is a great deal of vertical structure in the current profiles in The Narrows as is seen in East Passage.

8. TIDAL PRISMS AND DISSIPATION

Tidal prisms are directly related to tidal transport (e.g. Eq. 16). Tidal prisms for the M_2, K_1 and composite tides into principal regions of Puget Sound have been computed from the model results and plotted schematically in Fig. 30-32. The channel configuration in the vicinity of the north end of Colvos Passage is complex. There tides entering or leaving Colvos Passage can pass around both sides of Blake Island or come through Rich Passage. The complexity of this junction is abbreviated in Figs. 30-32.

For the M_2 tide (Fig. 30), the total tidal prism entering via Admiralty Inlet is 4.74 km^3, close to the estimate of Parker (1977) from current meter data. Since the total volume of water in the Sound is estimated to be 168.7 km^3 (McLellan, 1954), the full M_2 tidal prism is nearly 2.8% of the total volume of the Sound. The M_2 tide through Deception Pass (Fig. 30) provides little tidal prism (0.04 km^3) because, though the currents are swift, the cross-sectional area of the Pass is small. The tidal prism through Deception Pass amounts to less than 1% of that entering Admiralty Inlet.

Values of the M_2 prism decrease into the network and split at the junctions (Fig. 30). The difference in inflow and outflow for any junction or channel represents the amount of water stored. The northern part of the main basin, for example, is seen to have significant storage capacity (~1.1 km^3).

Of the total M_2 prism, 14.6% finds its way to Hood Canal, 19.6% to Whidbey basin, and 22.2% to the Narrows and the southern basin. Thus the capacity of Whidbey basin for M_2 storage is comparable to that of the southern basin. The bulk (34.0%) of the M_2 tide is stored in the main basin, while only 9.7% is stored in Admiralty Inlet. The partitioning of the composite tidal prism into principal regions of Puget Sound by University of Washington (1954), based on

the work of McLellan (1954), puts slightly more fractional prism into Admiralty Inlet (12.4%) and Whidbey basin (22.6%) and slightly less into main (30.1%) and southern (20.9%) basins.

The total K_1 prism is 3.83 km^3, nearly as large as that of M_2. The volume is distributed as follows: 15.0% in Admiralty Inlet, 31.6% in main basin, 20.1% in Whidbey basin, 15.0% in Hood Canal, and 18.2% in The Narrows and southern basin. The prism through Deception Pass (0.02 km^3) is very small, as it is for M_2. Partitioning among the five major subareas of Puget Sound for the constituents other than M_2 and K_1 follow closely the areal partitioning of the M_2 and K_1 prisms.

The average volume transport rate through a section for a single tidal constituent is equal to twice the tidal prism divided by the tidal period. Consequently, the average volume transport rate through Admiralty Inlet at Port Townsend for the M_2 and K_1 tides are 2.12×10^5 m^3/s and 8.61×10^4 m^3/s, respectively. In comparison, the annual average discharge rate of all rivers entering Puget Sound amounts to 1.17×10^3 m^3/s (Coomes *et al.*, 1984). Thus the M_2 and K_1 average volume flux through Admiralty Inlet are 181 and 74 times that of the annual average fresh water discharge to the Sound.

Tidal prisms through the same sections for a model composite tide (Table 13) have also been estimated (Fig. 32). The tidal transport amplitudes and phases coming from the model,

TABLE 13. Tidal prisms in Puget Sound. Tidal-height prisms were computed by University of Washington (1954) based on areal integrals of the height differences between mean high water and mean lower low water. The volume-flux prisms are computed from volume exchanges at junctions (Fig. 32) based on model composite (20 constituents) tidal transports.

Basin	Total Volume[1] (km^3)	Tidal-height Prism[2,3] (km^3)	(%)	Volume-flux Prism[3] (km^3)	(%)	Difference Volume-flux Prism Tidal Height Prism[4] (%)
Admiralty Inlet	21.7	1.00	4.6	0.98	4.5	−2.0
main basin	77.0	2.44	3.2	2.28	3.0	−6.6
southern basin/The Narrows	15.9	1.69	10.6	1.59	10.0	−5.9
Hood Canal	25.0	1.14	4.6	1.15	4.6	0.9
Whidbey basin	29.1	1.83	6.3	1.66	5.7	−9.3
Puget Sound (Total)	168.7	8.08	4.8	7.69	4.6	−4.8

[1] Volume below mean high water
[2] From University of Washington (1954), see Mofjeld and Larsen (1984)
[3] Percentages are for the tidal prisms relative to the total volume
[4] Percentages are relative to the tidal-height prism

expanded to 20 constituents using the equilibrium tide relationships between major and minor tidal components, were used to create a volume flux time series through each cross-section of interest. At a given cross-section differences were taken between 19-year averages (same period, or tidal epoch, used for the tidal datums) of the maximum landward volumes transported and the daily extreme seaward volume transported as predicted by the model. These differences at various transects are the model-estimated total tidal prisms. For comparison, the tidal prism estimates of the University of Washington (1954) are based on areal integrals over 57 sections of Puget Sound of the observed difference between mean high water and mean lower low water.

The model composite tidal prism throughout Admiralty Inlet (Figure 32) is 7.69 km^3, somewhat less than that estimated by the University of Washington (1954): 8.08 km^3. The percentage partitioning of the composite tide among Admiralty Inlet, Hood Canal, Whidbey basin, the main basin, and the combined southern basin and The Narrows from both methods of estimation are within 2%, however, with the largest difference occurring for Whidbey basin. The tidal prism of the composite tide is 4.6 and 4.8% of the total volume of the Sound for the two methods of estimation (Table 13). Percentage of the tidal prism relative to the total volume for individual basins of Puget Sound (Table 13) show a range of 3.0% (main basin) to 10.6% (southern basin). Though the main basin captures the largest fraction of the tidal prism, its volume exceeds that of the other basins by a factor of approximately 3-5.

The difference between the model and University of Washington (1954) estimates (7.69 versus 8.08 km^3) of the total tidal prism for the Sound amounts to about 5%. One reason for this discrepancy is that the observed tidal prisms are based on a larger surface water area at mean high water rather than the area at mean lower low water which is used in the model. The difference between estimates for the individual basins (Table 13) shows that the largest difference occurs for Whidbey basin (9.3% underestimate of absolute volume) which has extensive tide flats that are bare at low water. Another reason finds root in the different spatial distributions of the observed and model tides. For example, the model total tidal prism in Hood Canal is slightly greater (0.9%, Table 13) than the estimate of University of Washington (1954) because the model systematically overestimates the amplitude of the major tidal constituents in Hood Canal. A third reason is that the model composite tidal prism does not include annual Sa and semidiurnal Ssa constituents.

The average rate of energy flux into and through the network of channels landward of any point of evaluation is computed with Eq. 18. For any given reach the tidal dissipation is the difference between the incoming and outgoing energy fluxes. Energy fluxes through Puget Sound for the M_2 and K_1 tides are represented schematically in Figs. 33 and 34. Fig. 33 shows that the M_2 tide dissipates 528 MW of energy over the entire Sound, with 374 MW being dissipated in the high velocity, high friction region of Admiralty Inlet (Table 14). An additional 61 MW of M_2 power is dissipated in The Narrows. Together the two sill regions account for

TABLE 14. Tidal dissipation rates in principal regions of Puget Sound.

Location	Surface Area* (m^2)	Tidal Dissipation (MW)			Tidal Dissipation/unit area (W/m^2)		
		composite	M_2	K_1	composite	M_2	K_1
Admiralty Inlet	3.76×10^8	513	374	61	1.36	0.99	0.16
main basin	7.18×10^8	40	28	4	0.06	0.04	0.01
southern basin	3.68×10^8	55	37	4	0.15	0.10	0.01
Hood Canal	3.47×10^8	16	9	1	0.15	0.03	0.00
Whidbey basin	5.04×10^8	47	33	3	0.09	0.06	0.01
The Narrows	1.49×10^7	78	61	6	5.23	4.09	0.40
TOTAL	2.33×10^9	733	528	78	0.31	0.23	0.03

* Area of mean lower low water from McLellan (1954).

82% of the total M_2 energy dissipated. Comparatively little dissipation occurs in Hood Canal (Table 14), according to the model, primarily because of the nearly out of phase relationship between the tide and tidal current there.

The energy fluxes (Fig. 34) and dissipation rates of the K_1 tides (Table 14) are much smaller than for the M_2. The rate is only 78 MW over the entire sound, with 86% of that occurring in Admiralty Inlet and The Narrows. For both M_2 and K_1 tides, the rate of energy input into both ends of Whidbey basin is nearly equal.

The energy fluxes for the composite tide (Fig. 35) take into account the contribution of 20 tidal constituents and their phase relationships. They were computed by averaging the product of predicted, demeaned tides and tidal transports at major junctions over a 19-year epoch. Total tidal dissipation in the Sound is calculated to be 733 MW (Fig. 35). Approximately 513 MW of the dissipation, or 70% of the total, occurs in Admiralty Inlet, while another 78 MW is dissipated in The Narrows. The tidal energy dissipated in Whidbey basin is 47 MW, 2/3 of which arrives through Possession Sound. Southern basin dissipates more tidal energy (55 MW) than does main basin (40 MW) or Hood Canal (16.5 MW). The total 733 MW tidal dissipation rate may be compared to the 6.4×10^4 MW tidal dissipation rate in the Irish Sea (Proudman, 1953), the 8.8×10^4 MW tidal dissipation rate in the North Sea (Davies *et al.*, 1985), or the worldwide tidal dissipation rate of ~4-7 $\times 10^6$ MW (Lambeck, 1978; Sündermann and Brosche, 1978).

Model dissipation rates per unit area are obtained by dividing the calculated dissipation rates in each basin by the basin area at mean lower low water for which McLellan (1954) provides values (Table 14). This results in an estimate of dissipation of 5.23 W/m^2 in The Narrows

(Table 14), nearly four times the rate for Admiralty Inlet (1.36 W/m^2). The smallest dissipation per unit area for the composite tide occurs in the main basin (0.06 W/m^2). M_2 and K_1 dissipation rates per unit area for the principal basins of Puget Sound are given in Table 14.

9. CONCLUSIONS

The distributions of tidal heights and phases around Puget Sound can be modeled with a linked channel model having linear dynamics. In order for good correspondence between model and data, friction coefficients must range from 2.0×10^{-3} to 6.0×10^{-3} m/s, the highest being in channels like Admiralty Inlet and The Narrows where tidal flows are strongest. These are also the regions in which tidal amplitude and phase gradients are the largest. These friction values are unusually high, but they are consistent with high values found in modeling studies of the Straits of Juan de Fuca-Georgia system.

The model, having been calibrated with the observed tidal distributions by adjusting entrance amplitudes and, for M_2, the friction coefficients, does reasonably well in estimating tidal transports. This conclusion is based on a comparison of model estimates and those coming from currents measured on cross-sections across the Sound. One discrepancy in the transport comparisons is that of the phase of the K_1 tide, which the data shows to be progressing to smaller phases down the Sound from the north, while the model suggests the opposite progression.

A region of small geographic extent where the model fails is through Deception Pass. The model cannot reproduce the very large changes in amplitude and phase through the Pass, despite attempts to better the description of channel geometry by adding several more model segments and by using bathymetry of higher resolution. It must be thus suspected that non-linear dynamics places an important role there. Tidal distributions to the east of Deception Pass at Yokeko Point and into northern Whidbey basin appear to be reasonably described, so the model is viewed as providing good estimates in the Deception Pass region only at Yokeko Point and landward. The match of model and data through Port Washington Narrows into Dyes Inlet is also less than perfect, probably the result of insufficient bathymetric/geometric resolution of the model there.

The total tidal prism estimate and its distribution among the major basins of the Sound have model values close to those for earlier estimates. Tidal dissipation rates for the entire Sound, based on model results, are in the range of 733 MW for the composite tide and 528 MW for the M_2 tide. The bulk of the dissipation (>70%) occurs in Admiralty Inlet, though the dissipation rate per unit area is highest in The Narrows (5.23 W/m^2).

10. ACKNOWLEDGMENTS

We would like to thank Dave Kachel and Barry Neuhaus for contributions made to code and database development. This work was supported by NOAA/Environmental Research Laboratories.

11. REFERENCES

Bauer, H.A. 1928. Tides of the Puget Sound and adjacent inland waters. M.S. Thesis, University of Washington, Seattle, WA, 114 pp.

Bretschneider, D.E., G.A. Cannon, J.R. Holbrook, and D.J. Pashinski, 1985. Variability of subtidal current structure in a fjord estuary: Puget Sound, Washington, *J. Geophys. Res., 90*(C6), 11, 949-11,958.

Cannon, G.A., N.P. Laird and T.L. Keefer, 1979. Puget Sound circulation: final report for FY77-78. NOAA Tech. Memo. ERL MESA-40, 55 pp.

Chu, W., J.-Y. Liou, and K.D. Flenniken, 1988. Numerical modeling of tide and circulation in central Puget Sound: Comparison of a three-dimensional and a depth-averaged model. University of Washington, Dept. of Civil Engineering, Tech. Rpt. 109 (Water Resources Series), 51 pp.

Coomes, C.A., C.C. Ebbesmeyer, J.M. Cox, J.M. Helseth, L.R. Hinchey, G.A. Cannon, and C.A. Barnes, 1984. Synthesis of current measurements in Puget Sound, Washington – Volume 2: Indices of mass and energy inputs into Puget Sound: Runoff, air temperature, wind, and sea level, *NOAA Tech. Memo. NOS-OMS-4*, Rockville, MD, 45 pp.

Crean, P.B, 1978. A numerical model of barotropic mixed tides between Vancouver Island and the mainland and its relation to studies of the estuarine circulation, in: *Hydrodynamics of Estuaries and Fjords*, ed by J.C.J. Nihoul, Elsevier, Amsterdam, 283-313.

Davies, A.M., J. Sauvel, and J. Evans, 1985. Computing near coastal tidal dynamics from observations and a numerical model, *Cont. Shelf Res., 4*, 341-366.

Dronkers, J.J., 1964. *Tidal Computations in Rivers and Coastal Waters.* North-Holland, Amsterdam, 518 p.

Ebbesmeyer, C.C., C.A. Coomes, J.M. Cox, E.T. Baker, C.S. Smyth, and C.A. Barnes, 1986. Dynamics of Commencement Bay and approaches, *NOAA Tech. Memo, NOS-OMA-24*, Rockville, MD, 79 pp.

Gill, A.E., 1982. *Atmosphere-Ocean Dynamics*, Academic Press, New York, 662 pp.

Jamart, B.M., 1983. Report on the preliminary modeling of tides in East Passage, Report to METRO, Seattle, WA, 35 pp.

Jamart, B.M. and D.F. Winter, 1978. A new approach to the computation of tidal motions in estuaries, in: *Hydrodynamics of Estuaries and Fjords*, ed. by J.C.J. Nihoul, Elsevier, Amsterdam, 261-281.

Lambeck, K., 1978. Tidal dissipation in the oceans, In: *Tidal Friction and the Earth's Rotation*, ed. by P. Brosche and J. Sündermann, Springer-Verlag, New York, 95-97.

Liou, J.-Y., K. Flenniken, and W. Chu, 1988. Tidal circulation models for central Puget Sound. In: *Proceedings of the First Annual Meeting on Puget Research*, Vol. 1, Puget Sound Water Quality Authority, Seattle, WA, 93-98.

McGary, N. and J.H. Lincoln, 1977. *Tidal Prints*, University of Washington Press, Seattle, 51 pp.

McLellan, P.M., 1954. An area and volume study of Puget Sound, Washington, University of Washington, Department of Oceanography, *Tech. Rpt. 21*, 39 pp.

Mofjeld, H., 1975. Empirical model for tides in the Western North Atlantic Ocean. NOAA Technical Report ERL 340-AOML 19, 24 pp.

Mofjeld, H.O. and L.H. Larsen, 1984. Tides and tidal currents in the inland waters of Western Washington, *NOAA Tech Memo ERL PMEL-56*, Seattle, 52 pp.

Mofjeld, H.O. and J.W. Lavelle, 1984. Setting the length scale in a second-order closure model of the unstratified bottom boundary layer., *J. Phys. Ocean., 14*(4), 833-839.

Mofjeld, H.O. and M. Wimbush, 1977. Bottom pressure observations in Gulf of Mexico and Caribbean Sea. *Deep-Sea Res., 24*, 987-1004.

NOAA, 1984. Tidal current tables, 1985, Pacific Coast of North America and Asia, U.S. Department of Commerce, Rockville, MD, 270 pp.

Parker, B.B., 1977. Tidal hydrodynamics in the Strait of Juan de Fuca–Strait of Georgia. *NOAA Technical Rep., NOS-69*, 56 pp.

Pease, C.H., 1980. An empirical model for tidal currents in Puget Sound, Strait of Juan de Fuca, and southern Strait of Georgia, EPA 600/7-80-185, U.S. EPA, Washington, D.C., 33 pp.

Proudman, J., 1953. *Dynamic Oceanography*, Dover, NY., 409 pp.

Pugh, D.T., 1987. *Tides, Surges and Mean Sea-Level.* Wiley, New York, 472 pp.

Redfield, 1950. The analysis of tidal phenomena in narrow embayments. *Papers in Physical Oceanography and Met., 11*(4), MIT-WHOI, 36 pp.

Roberts, P.J.W., 1980. Current measurements and mathematical modeling in southern Puget Sound, in: *Estuarine and Wetland Processes*, P. Hamilton and K. MacDonald, eds., Plenum Press, New York, 269-284.

Roberts, R.W., 1974. Marine sedimentological data of the inland waters of Washington State, University of Washington, Dept. of Oceanography, *Special Rpt., 56*, 74 pp.

Schmalz, Jr., R.A., 1986. A numerical investigation of astronomic tidal circulation in Puget Sound., *Mis. Pap. CERC-86-9*, Corps of Engineers, Vicksburg, MS, 58 pp.

Schureman, P., 1958 (reprinted 1976). *Manual of Harmonic Analysis and Prediction of Tides.* Special Publ. No. 98, U.S. Gov. Printing Office, 317 pp.

Schwiderski, E.W., 1980. On charting global ocean tides. *Rev. Geophys. Space Phys., 18*, 243-268.

Sündermann, J. and P. Brosche, 1978. Numerical computation of tidal friction for present and ancient oceans, In: *Tidal Friction and the Earth's Rotation*, ed. by P. Brosche and J. Sündermann, Springer-Verlag, New York, 125-144.

University of Washington, Department of Oceanography, 1954. Puget Sound and approaches, a literature survey, Vol 3(10), University of Washington, Seattle, WA, 1-116.

Winant, C.D. and R.C. Beardsley, 1979. A comparison of some shallow wind-driven currents, *J. Phys. Oceanogr., 9*, 218-220.

Zetler, B.D., 1971. Radiational ocean tides along the coasts of the United States. *J. Phys. Oceanogr., 1*, 34-38.

Zetler, B.D., E.E. Long and L.F. Ku, 1985. Tide predictions using satellite constituents. *Int. Hydrog. Rev., LXII*, 135-142.

FIGURES

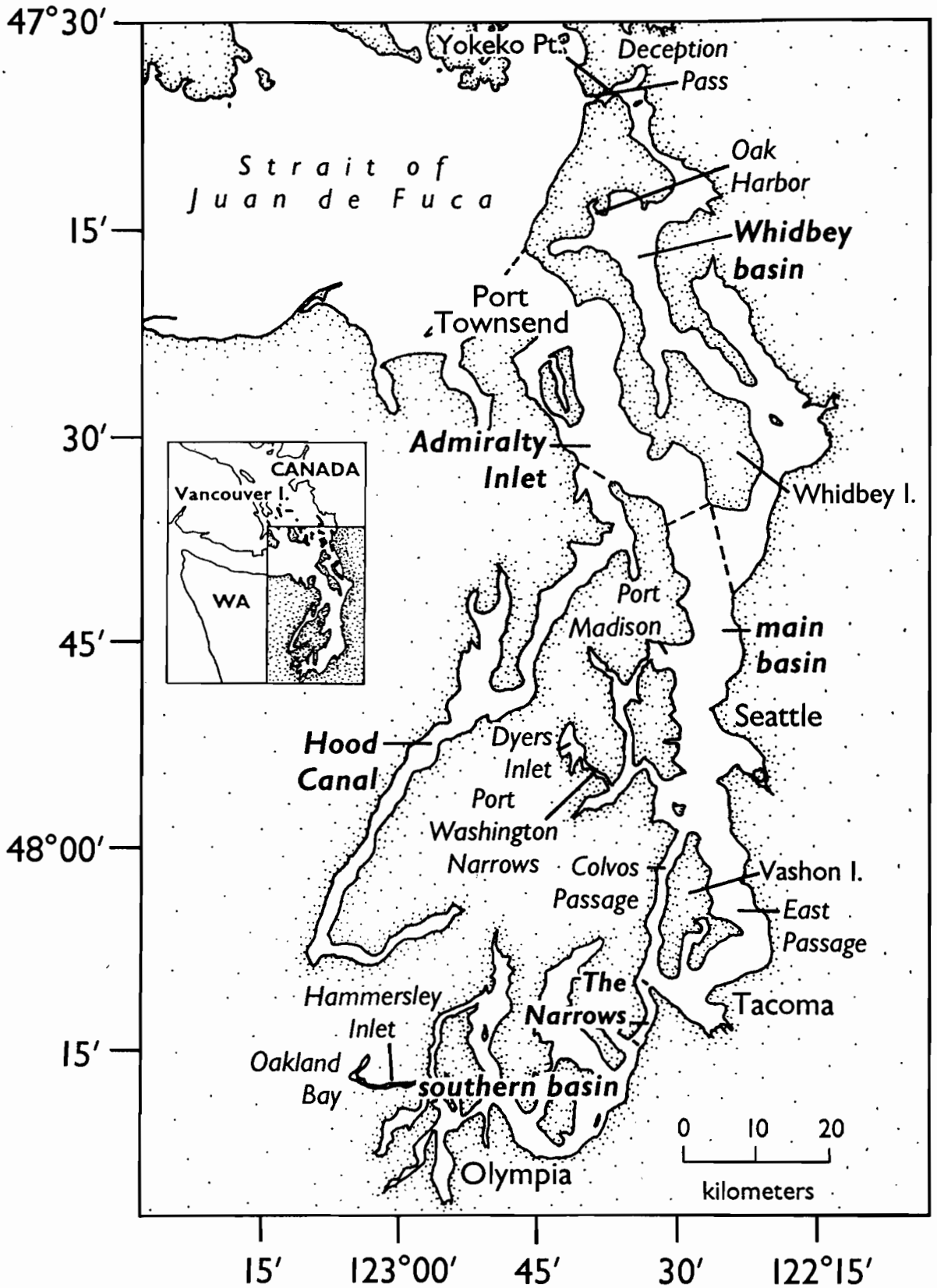

Figure 1: Map of Puget Sound with principal geographic locations noted. The shoreline is based on the mean lower low water datum from NOAA charts. Dashed lines separate the principal basins, which are identified in bold type.

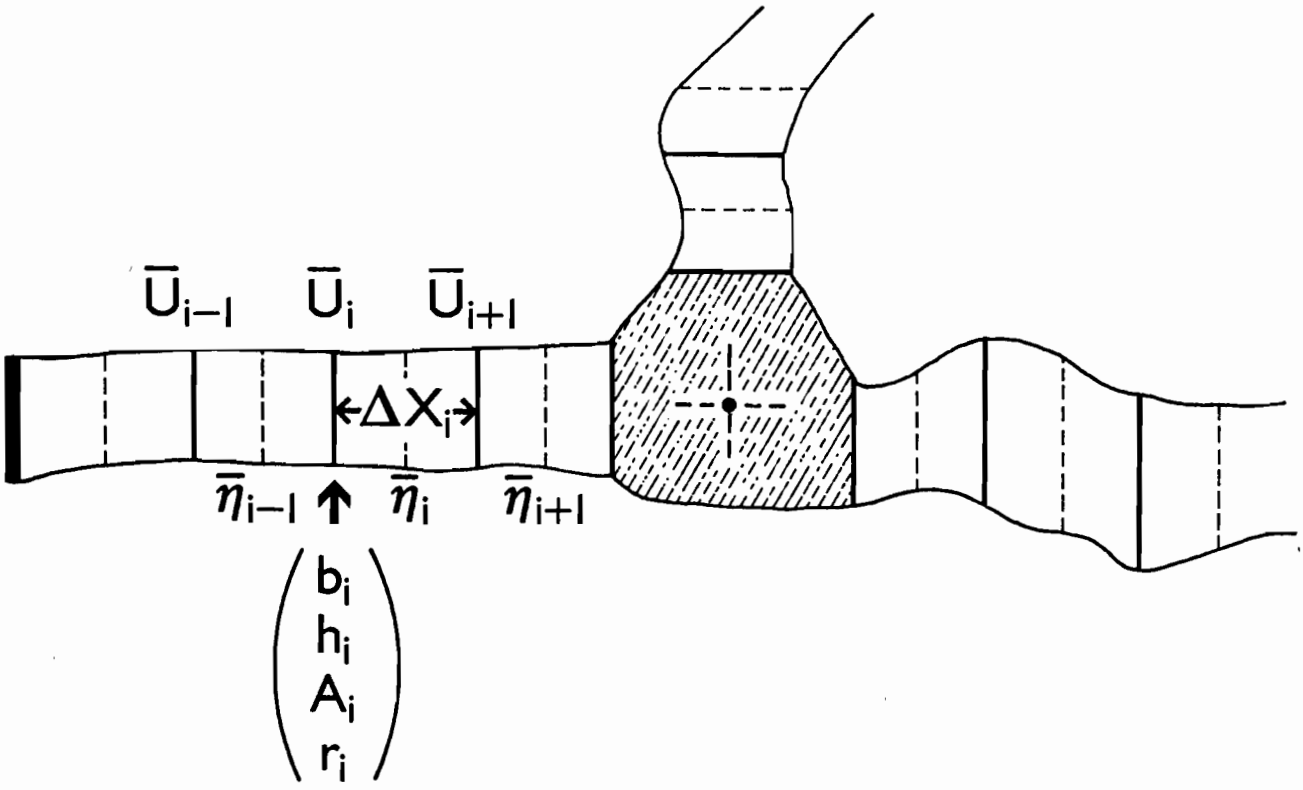

Figure 2: Notational schema for linked channels. Junction area is stippled. Heavy solid and dashed lines represent sites where transport ($\bar{U}$) and tidal height ($\bar{\eta}$) are evaluated, respectively. Channel characteristics, i.e., breadth (b), depth (h), area (A), and friction velocity (r), are given at the same site as transport. The double solid line represents the end of a channel where transport must be zero. A tidal height common to all channels is evaluated at the junction center.

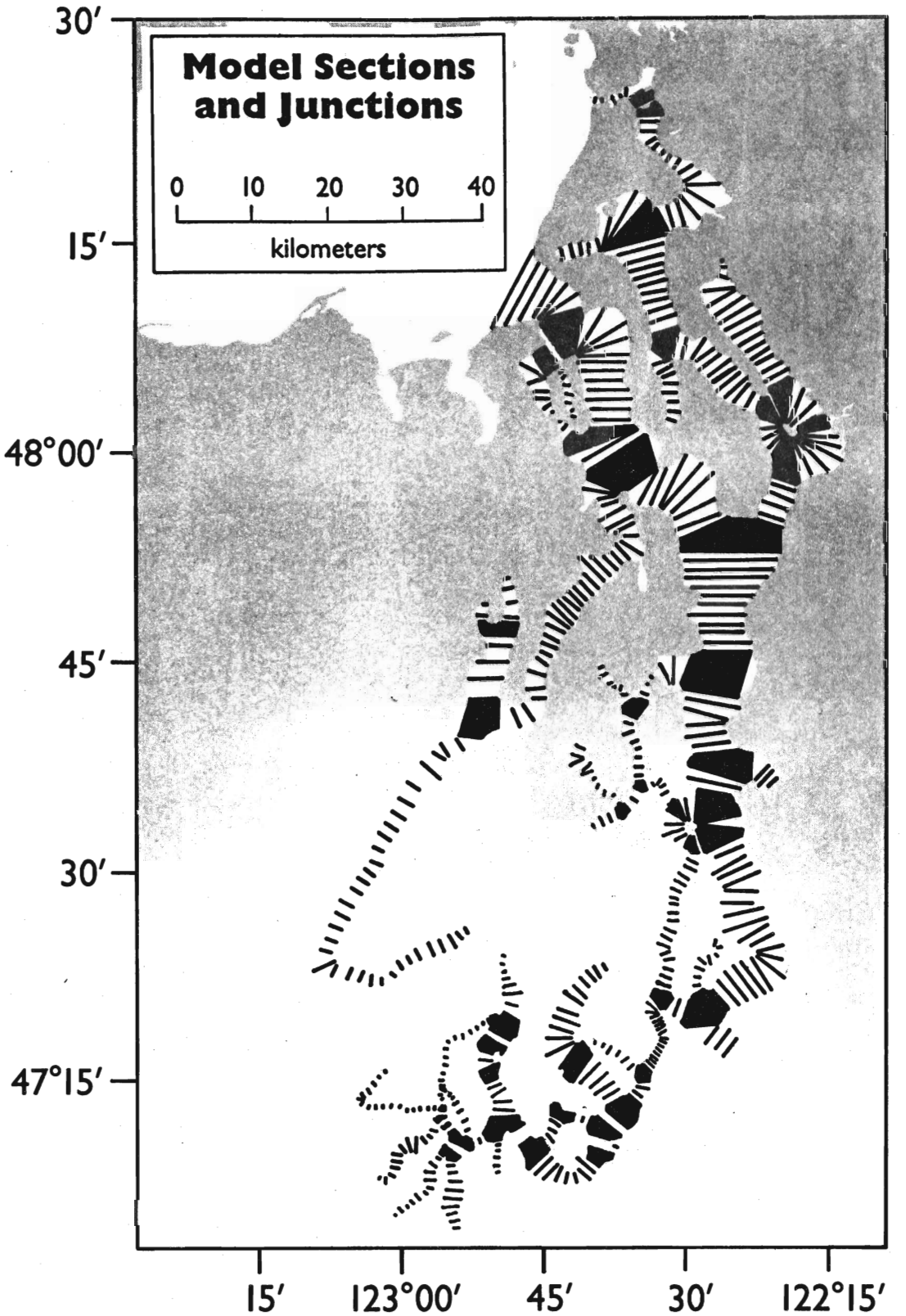

Figure 3: Transects and junctions (solid areas) defining the network used in calculating Puget Sound tides and tidal transports.

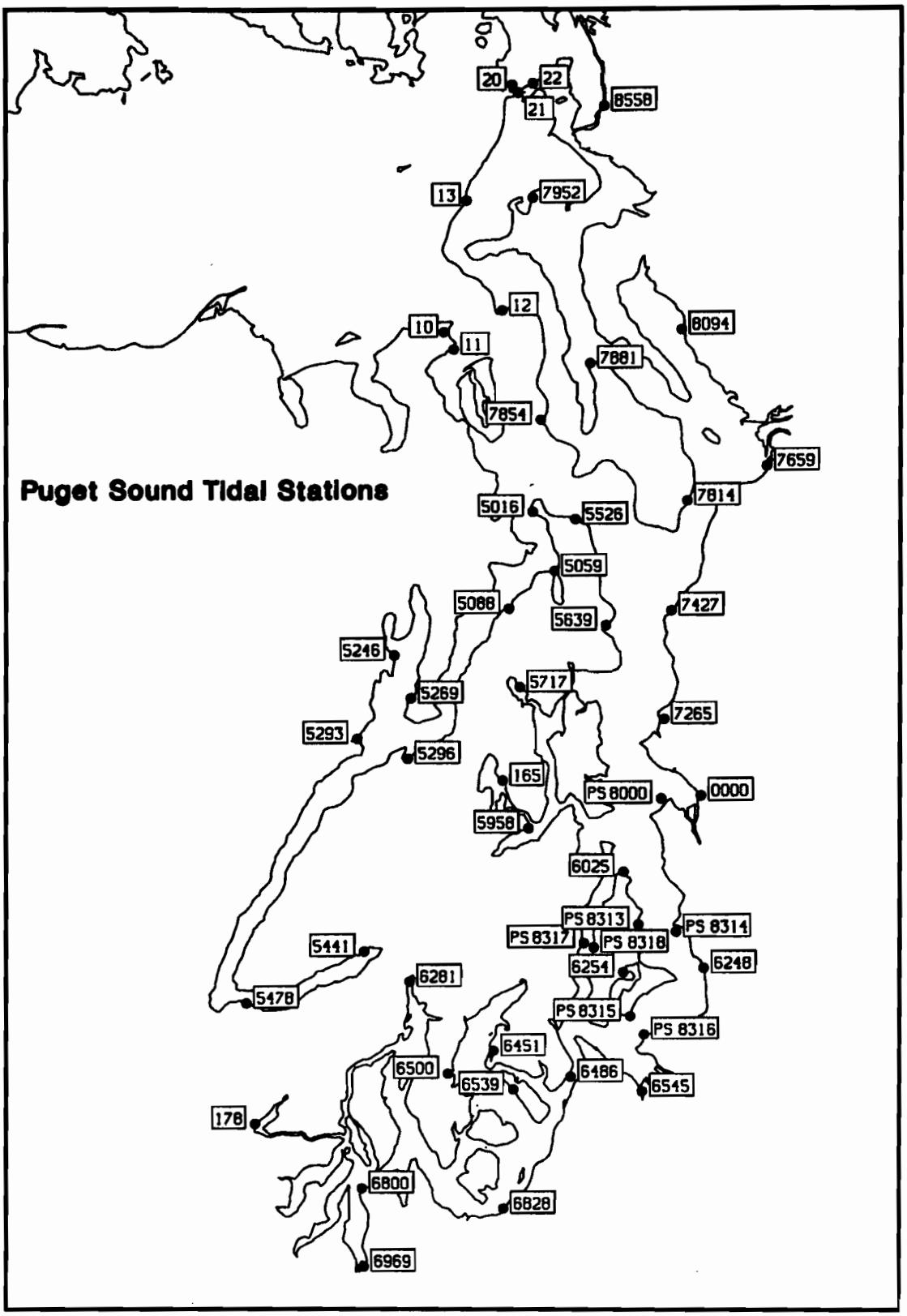

Figure 4: Tide and pressure gage stations in Puget Sound. Latitudes and longitudes are given in Table 3. Station identifiers are coded to represent data sources (Table 4).

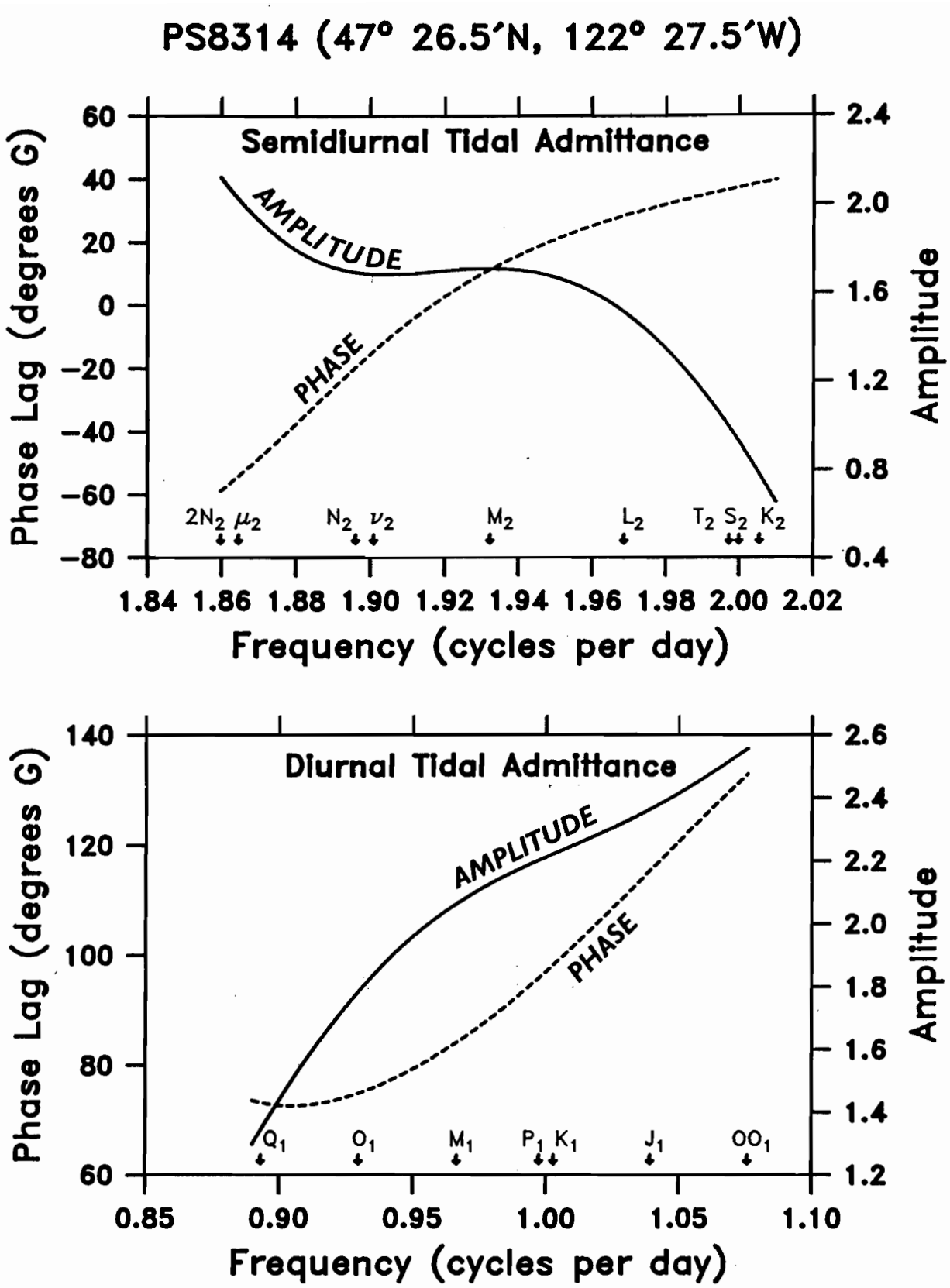

Figure 5: Semidiurnal and diurnal tidal admittance at PS8314 in southern main basin. Dashed line represents phase lags, and solid line represents amplitudes. Reference series is the tidal potential and analysis uses three complex weights per tidal band.

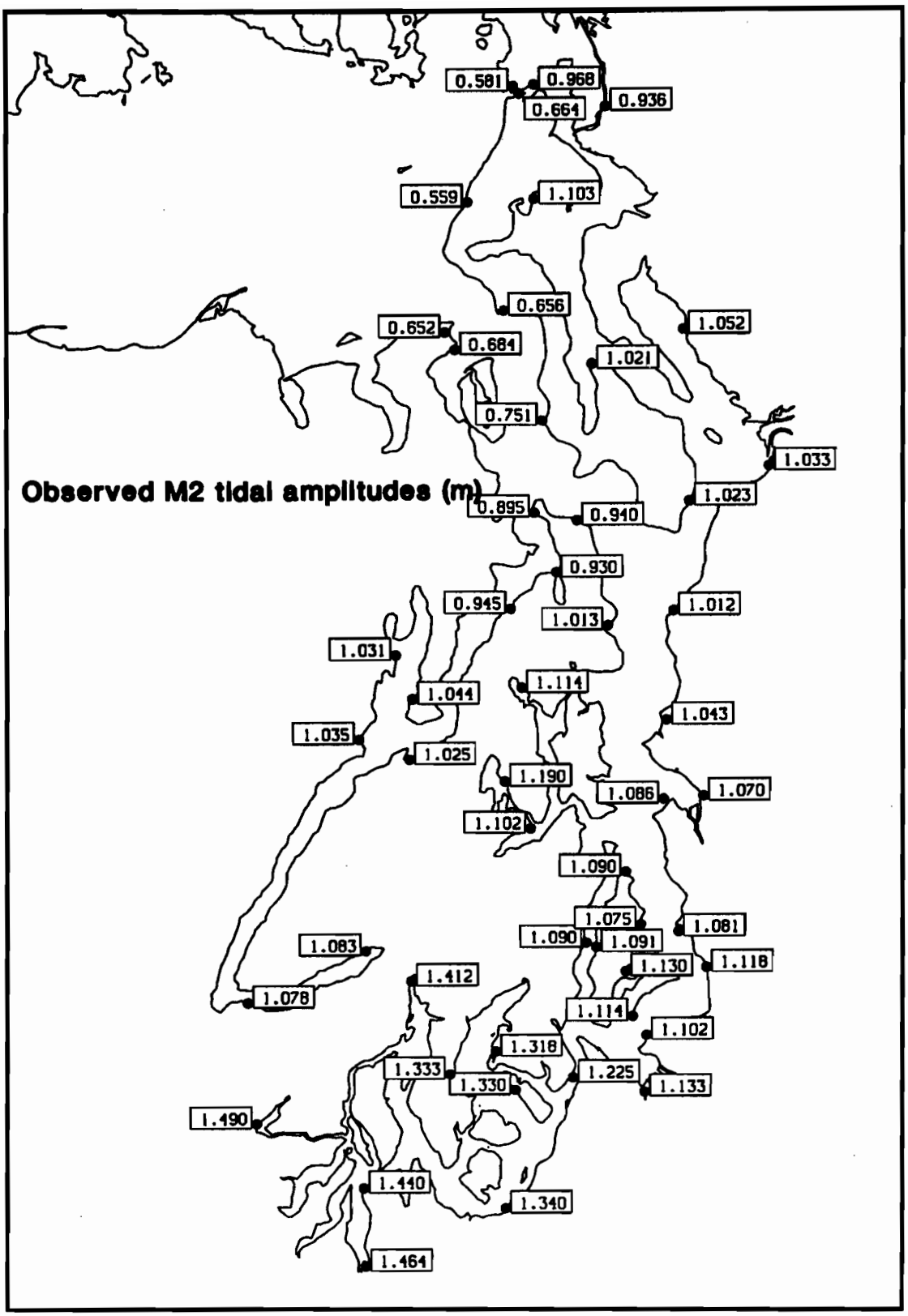

Figure 6a: Observed M_2 tidal amplitudes in meters.

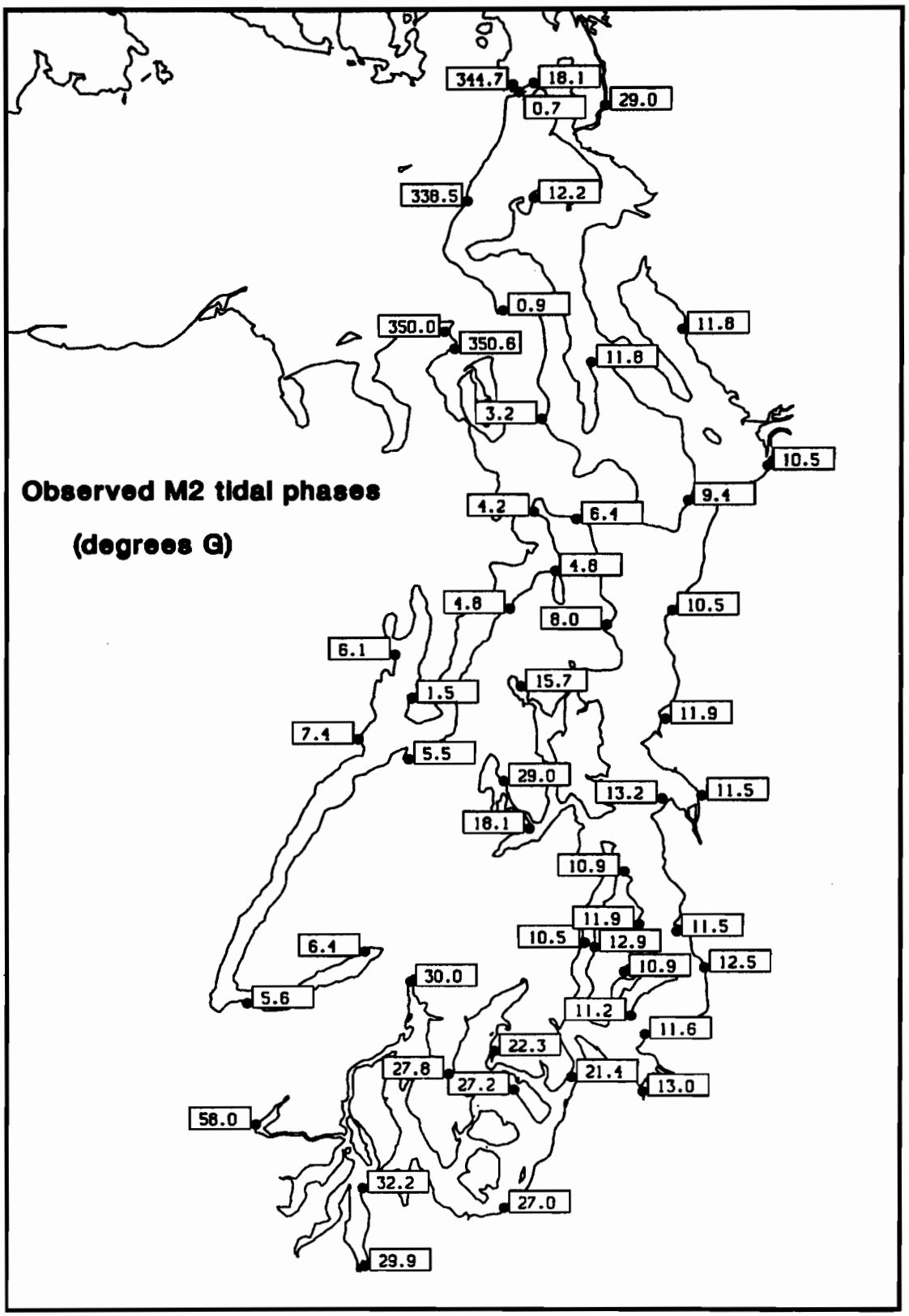

Figure 6b: Observed M_2 tidal phases in degrees. Phases are Greenwich phase lags.

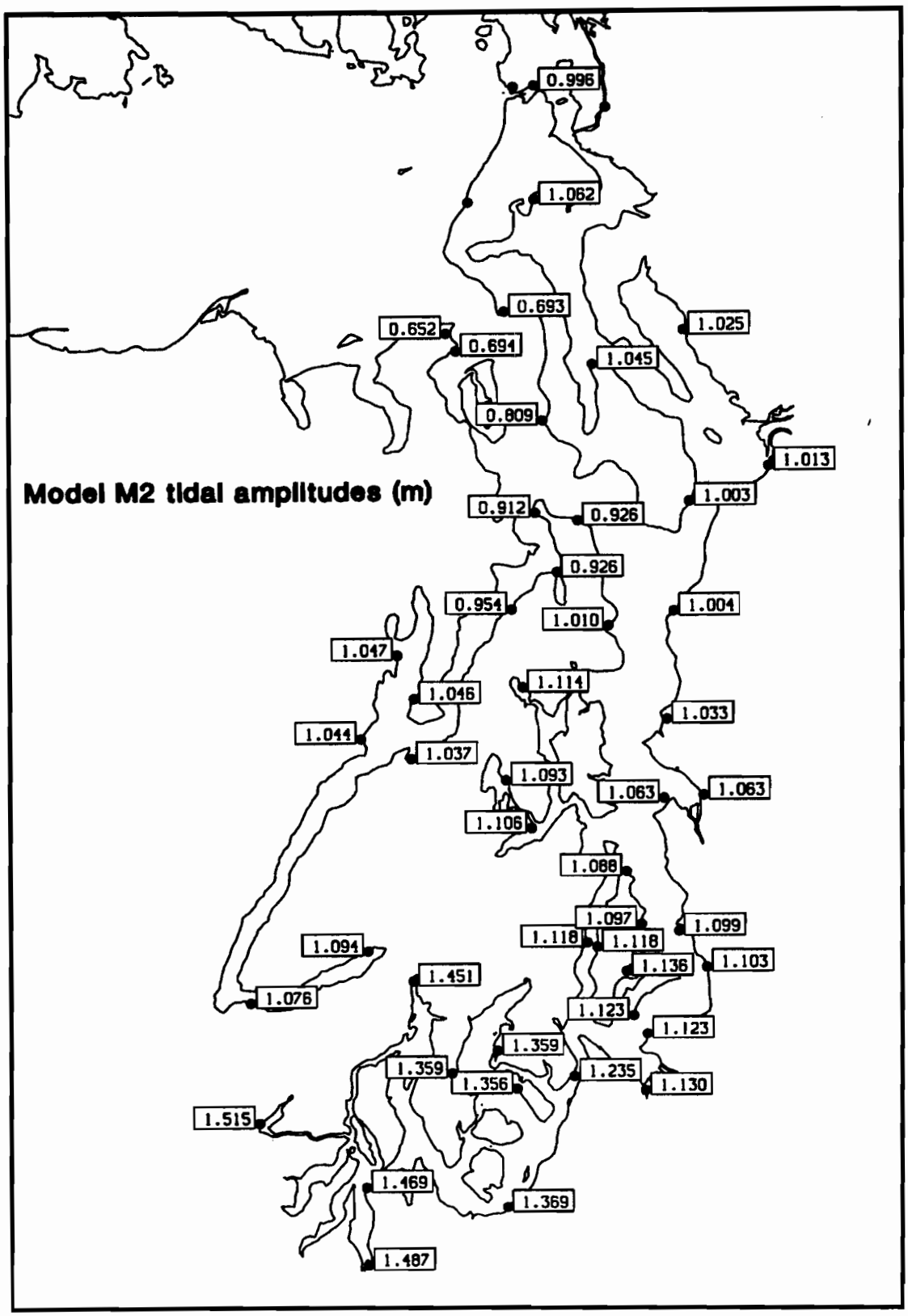

Figure 6c: Modeled M_2 tidal amplitudes in meters.

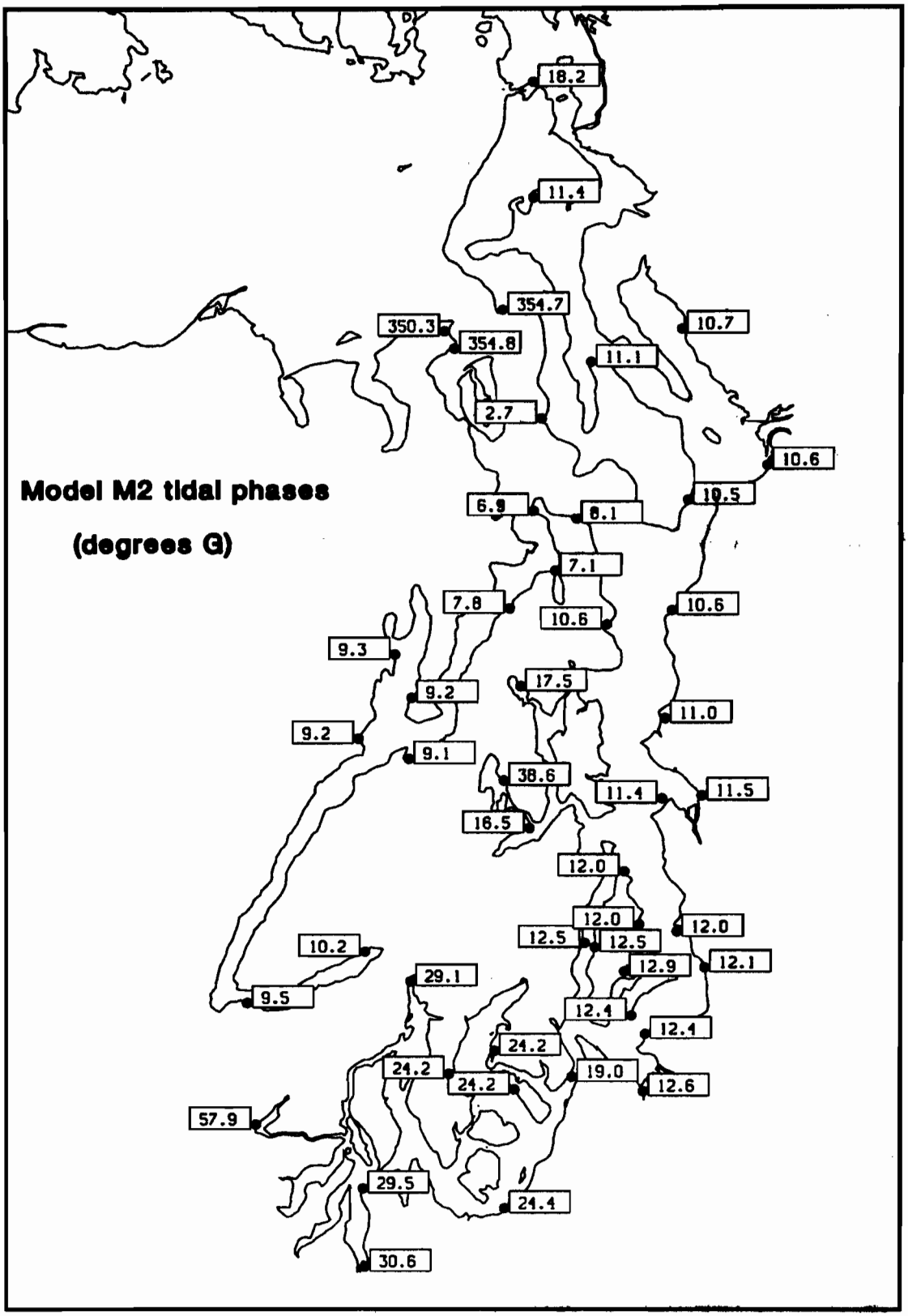

Figure 6d: Modeled M_2 tidal phases in degrees. Phases are Greenwich phase lags.

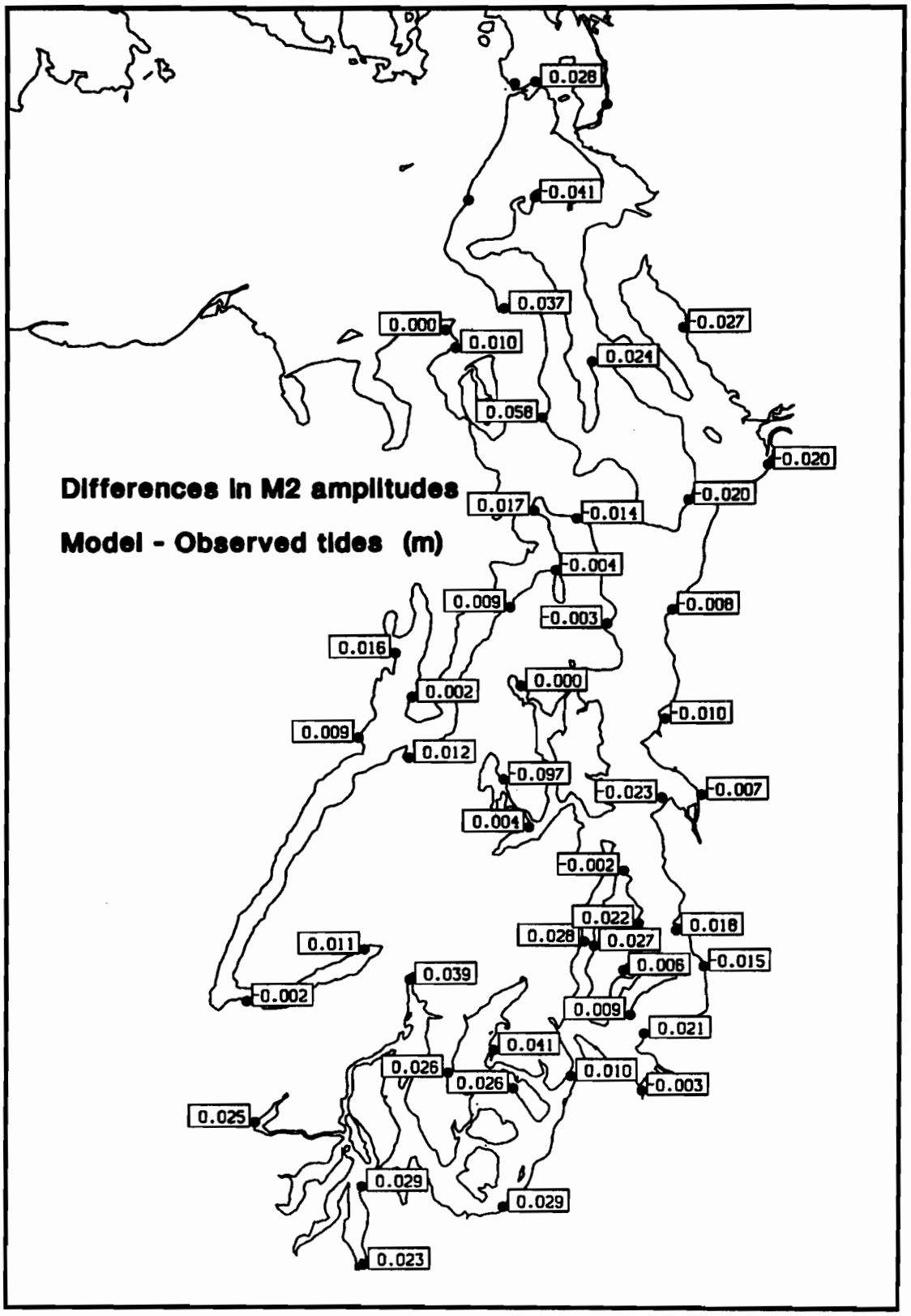

Figure 6e: Differences between modeled and observed M_2 tidal amplitudes in meters.

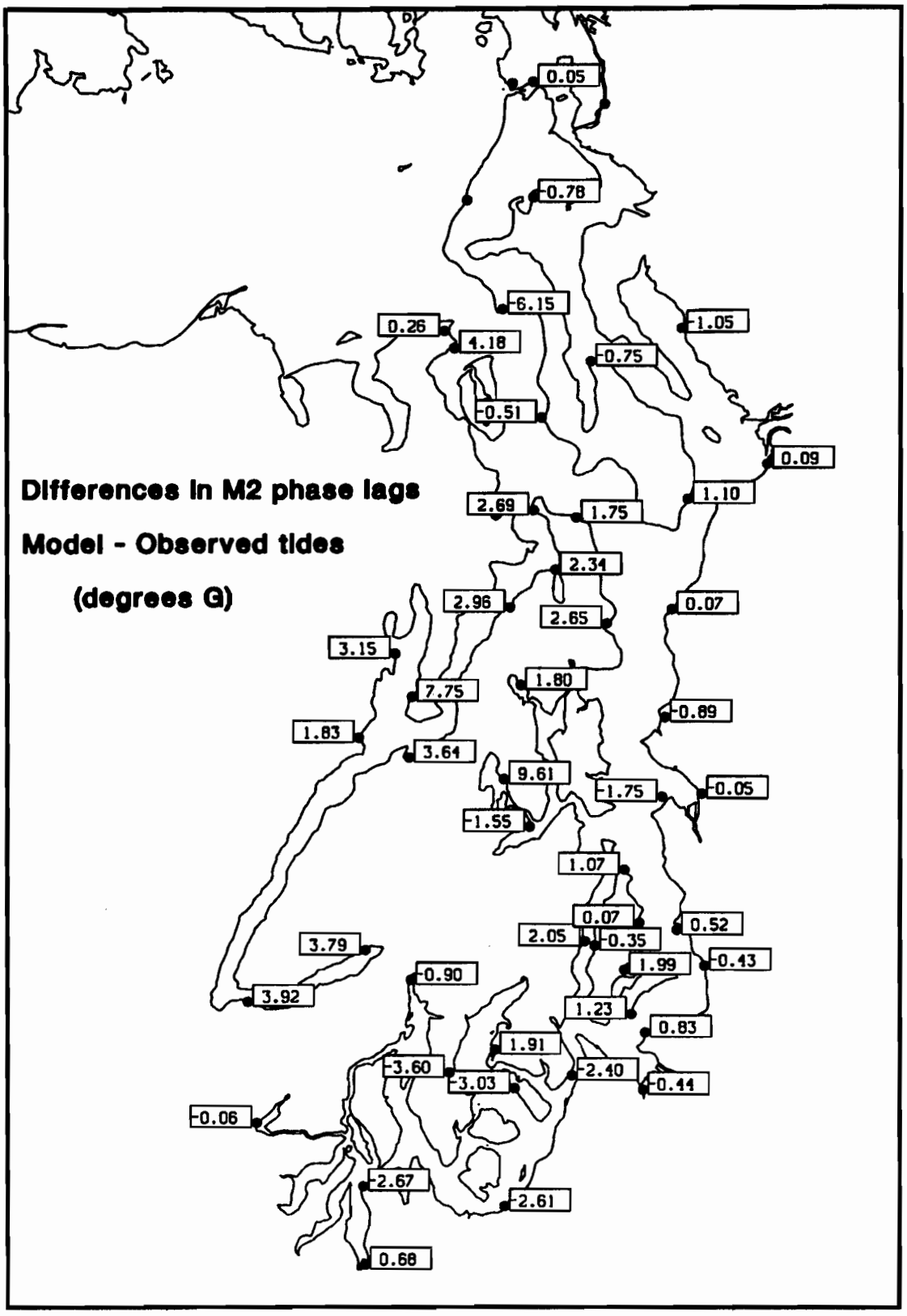

Figure 6f: Differences between modeled and observed M_2 tidal phases in degrees.

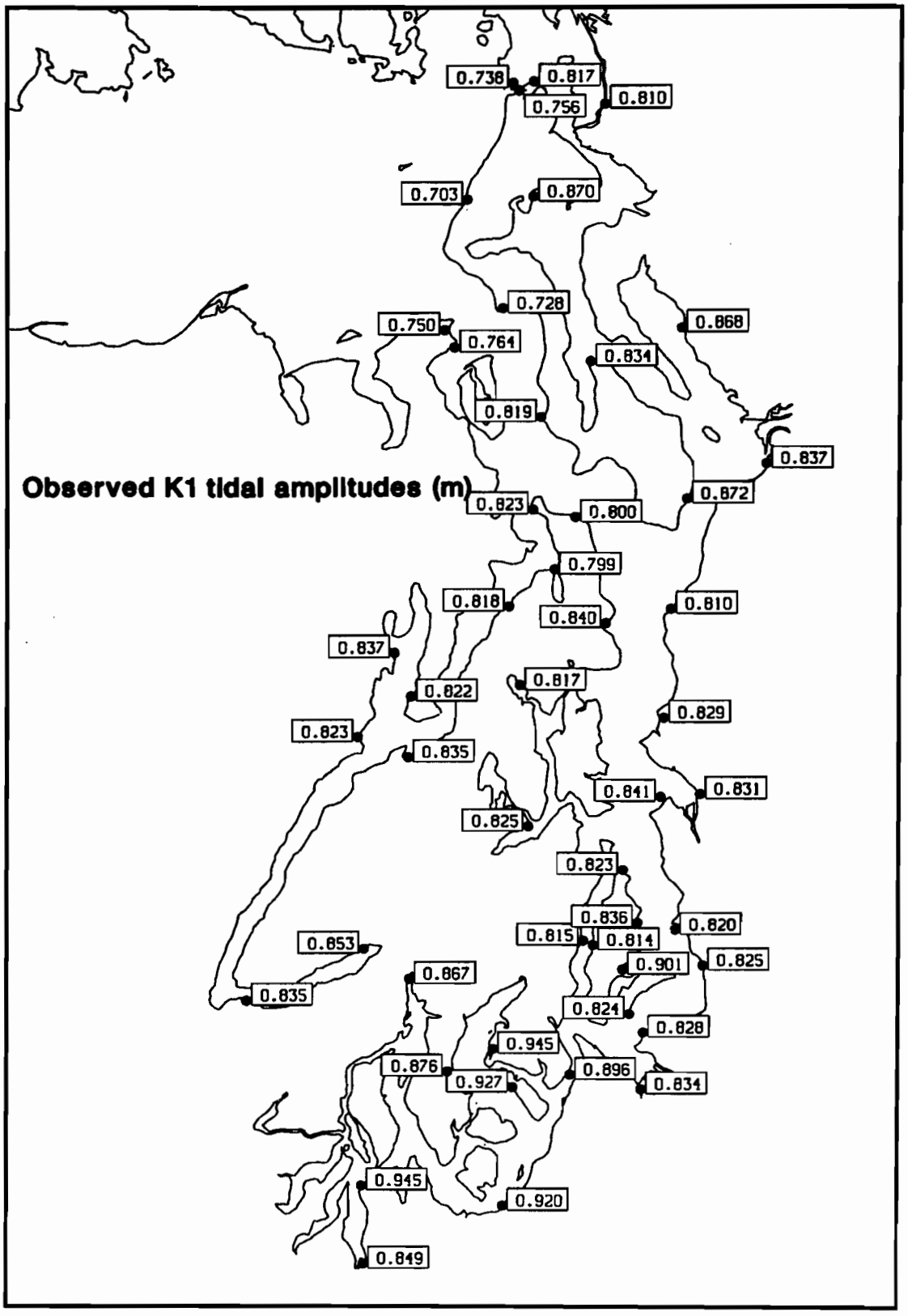

Figure 7a: Observed K_1 tidal amplitudes in meters.

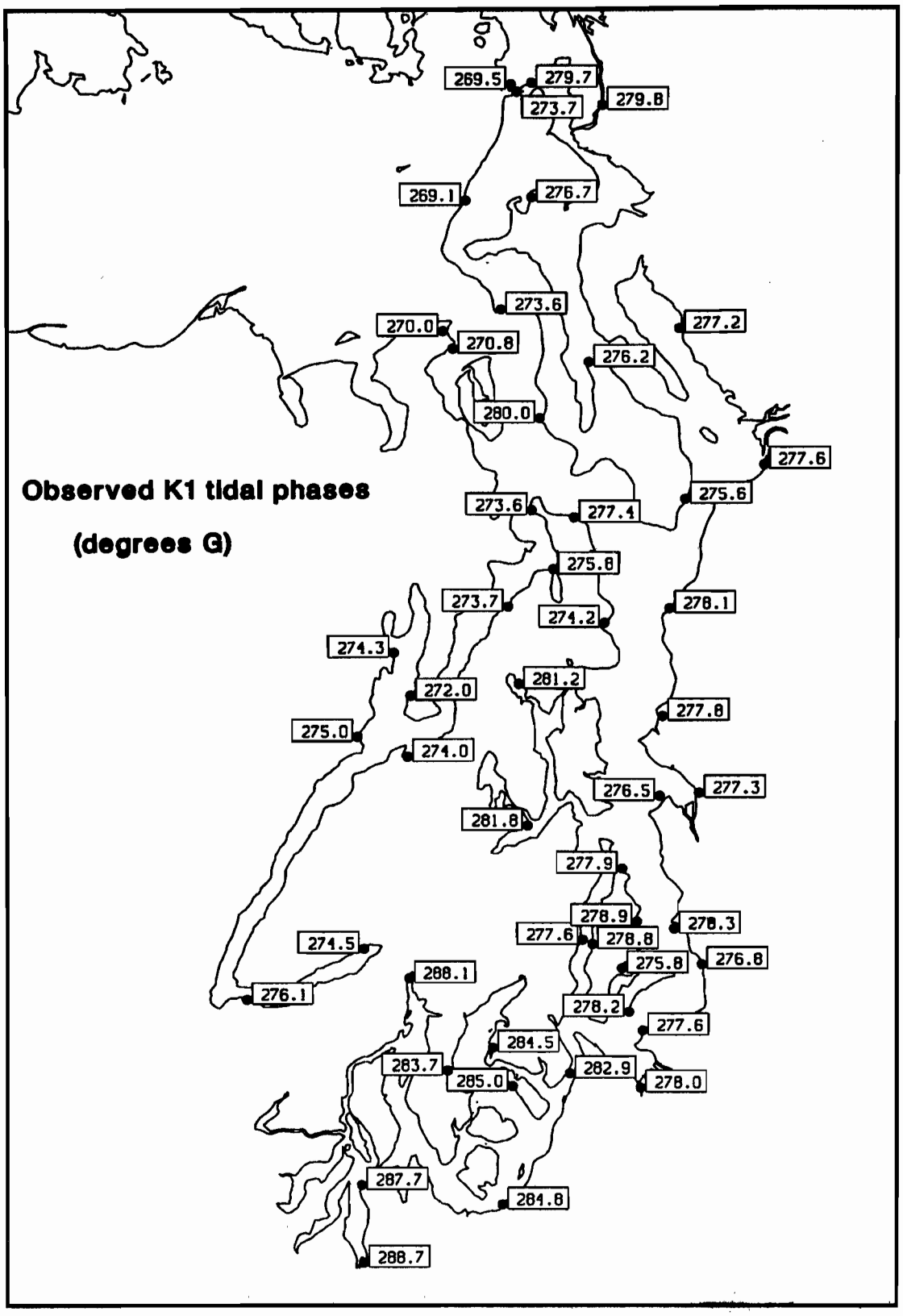

Figure 7b: Observed K_1 tidal phases in degrees. Phases are Greenwich phase lags.

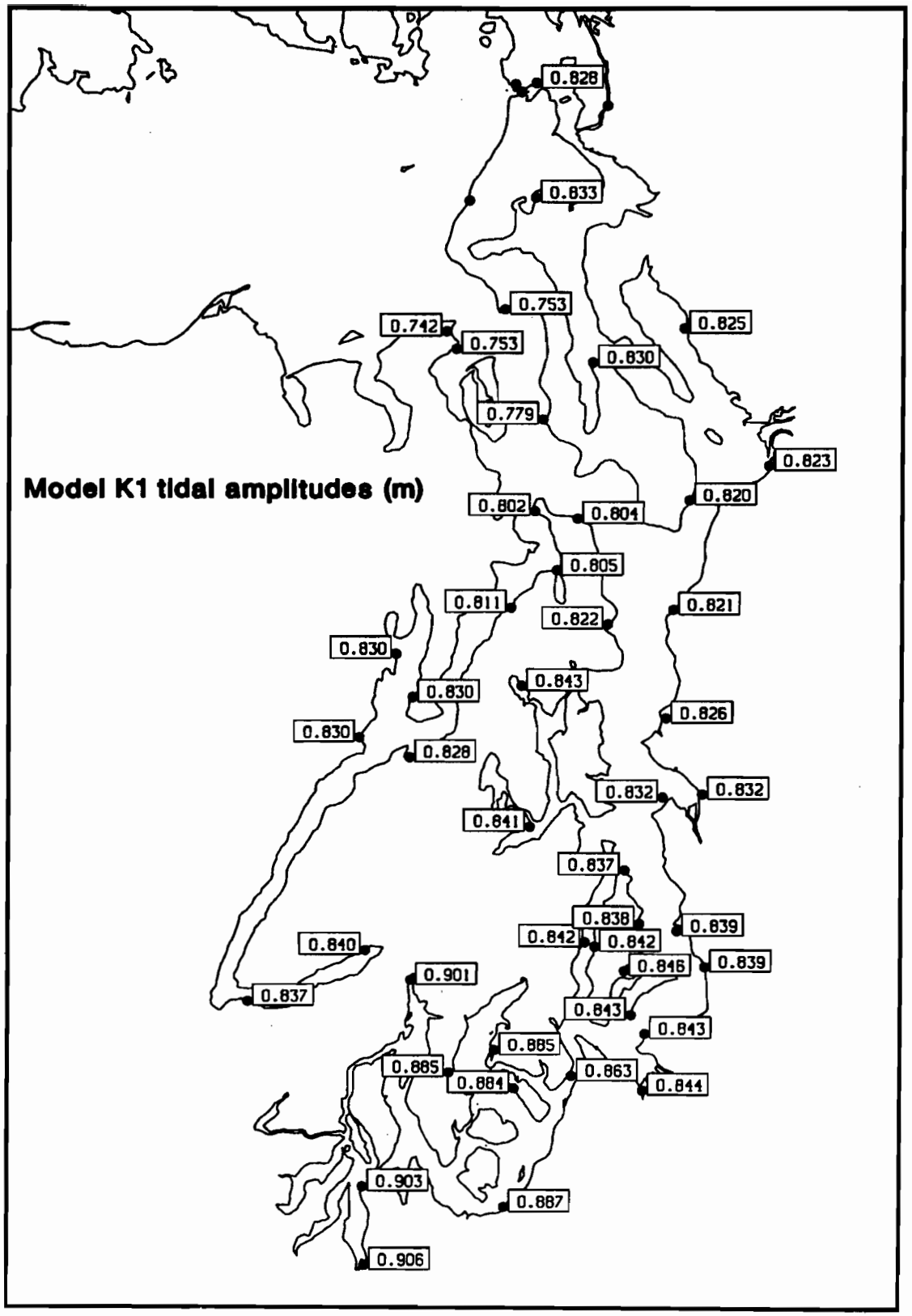

Figure 7c: Modeled K_1 tidal amplitudes in meters.

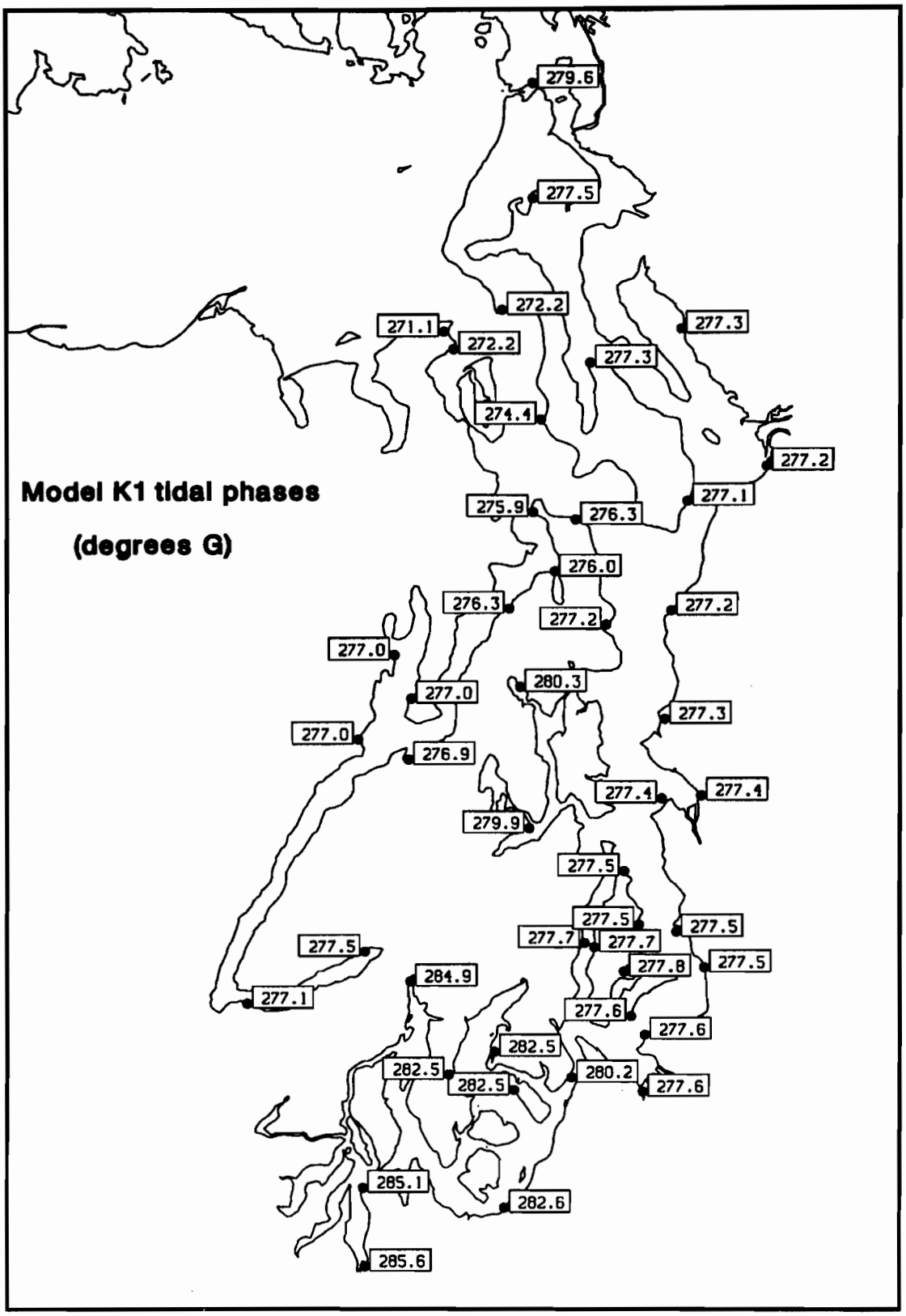

Figure 7d: Modeled K_1 tidal phases in degrees. Phases are Greenwich phase lags.

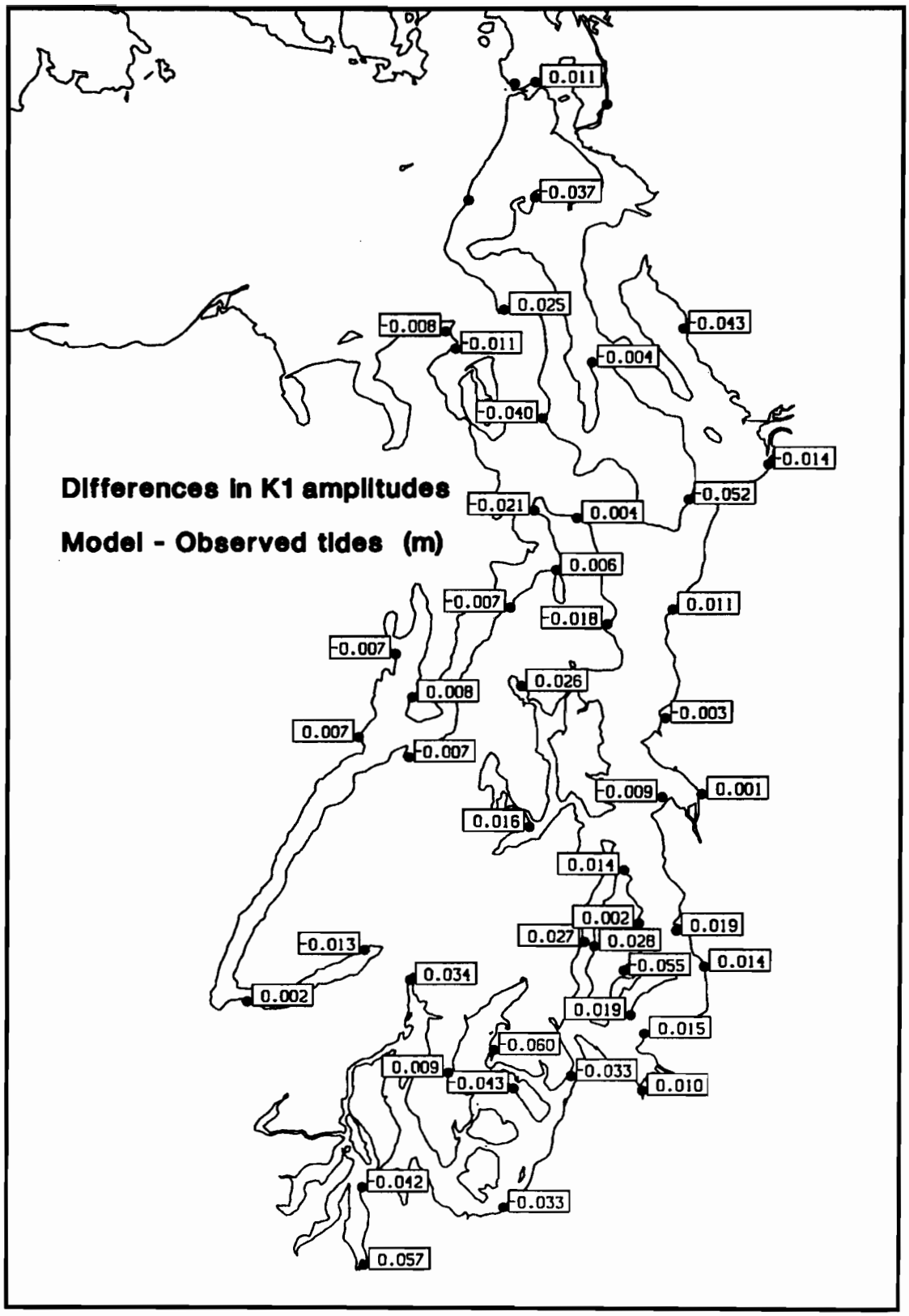

Figure 7e: Differences between modeled and observed K_1 tidal amplitudes in meters.

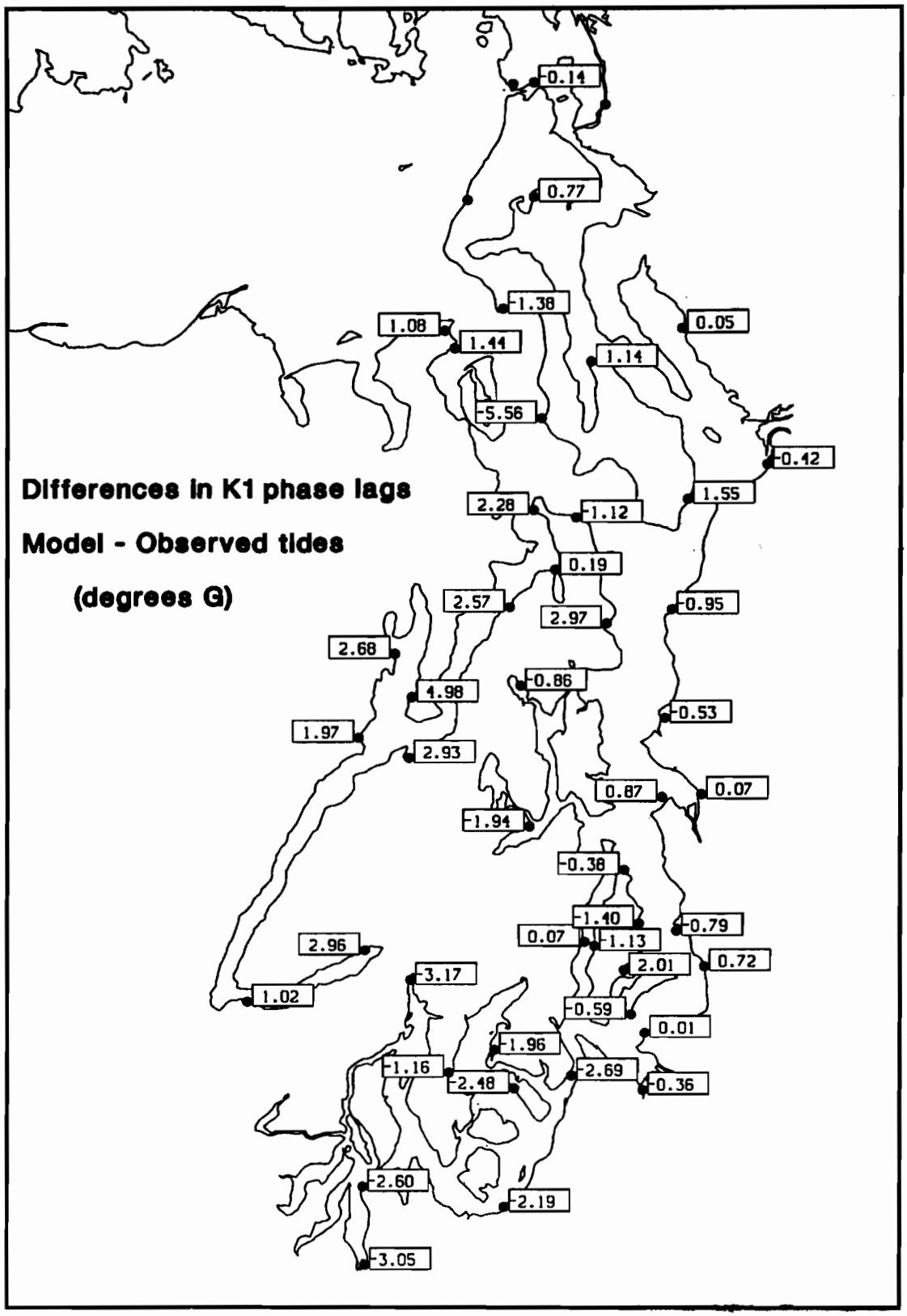

Figure 7f: Differences between modeled and observed K_1 tidal phases in degrees.

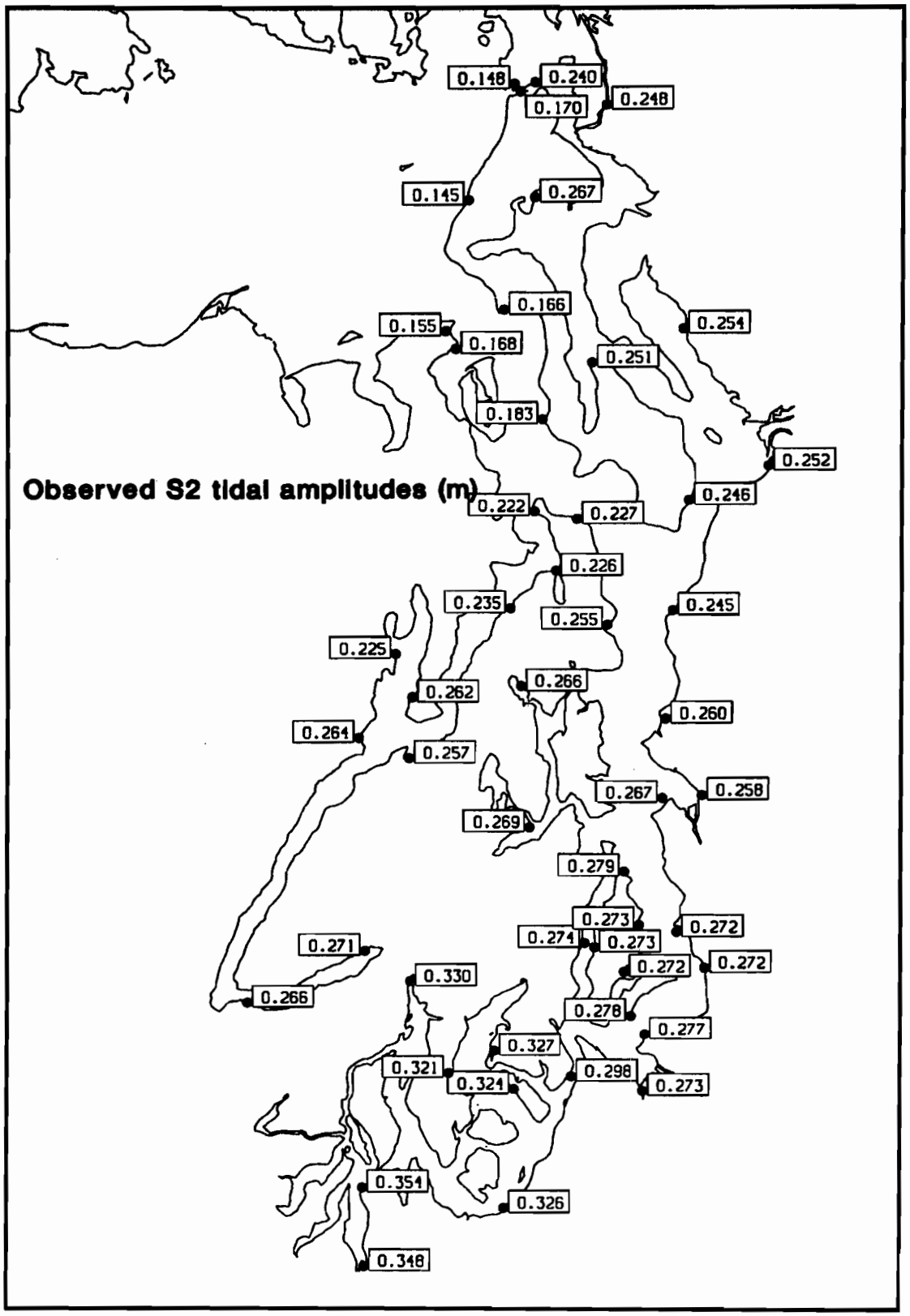

Figure 8a: Observed S_2 tidal amplitudes in meters.

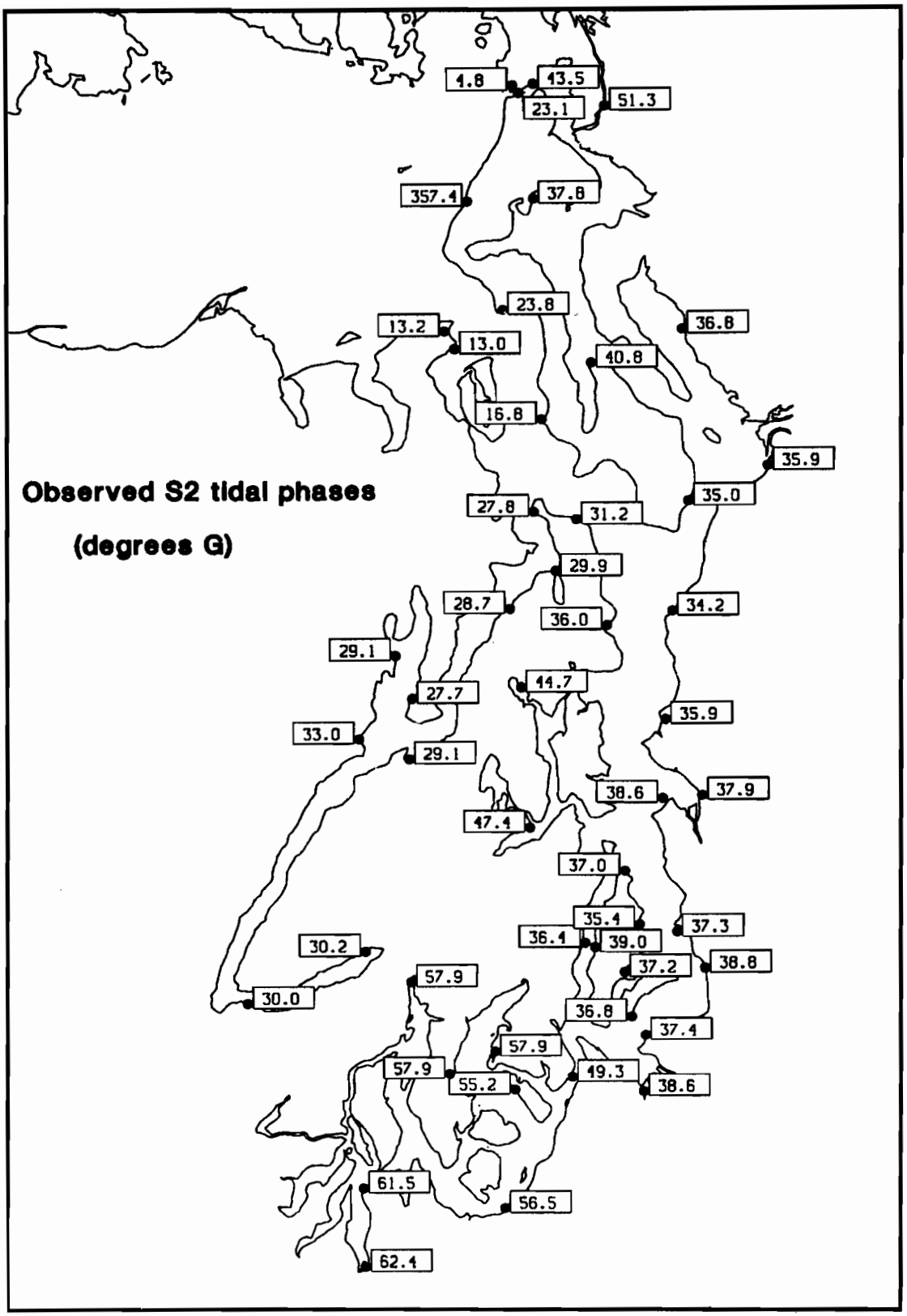

Figure 8b: Observed S_2 tidal phases in degrees. Phases are Greenwich phase lags.

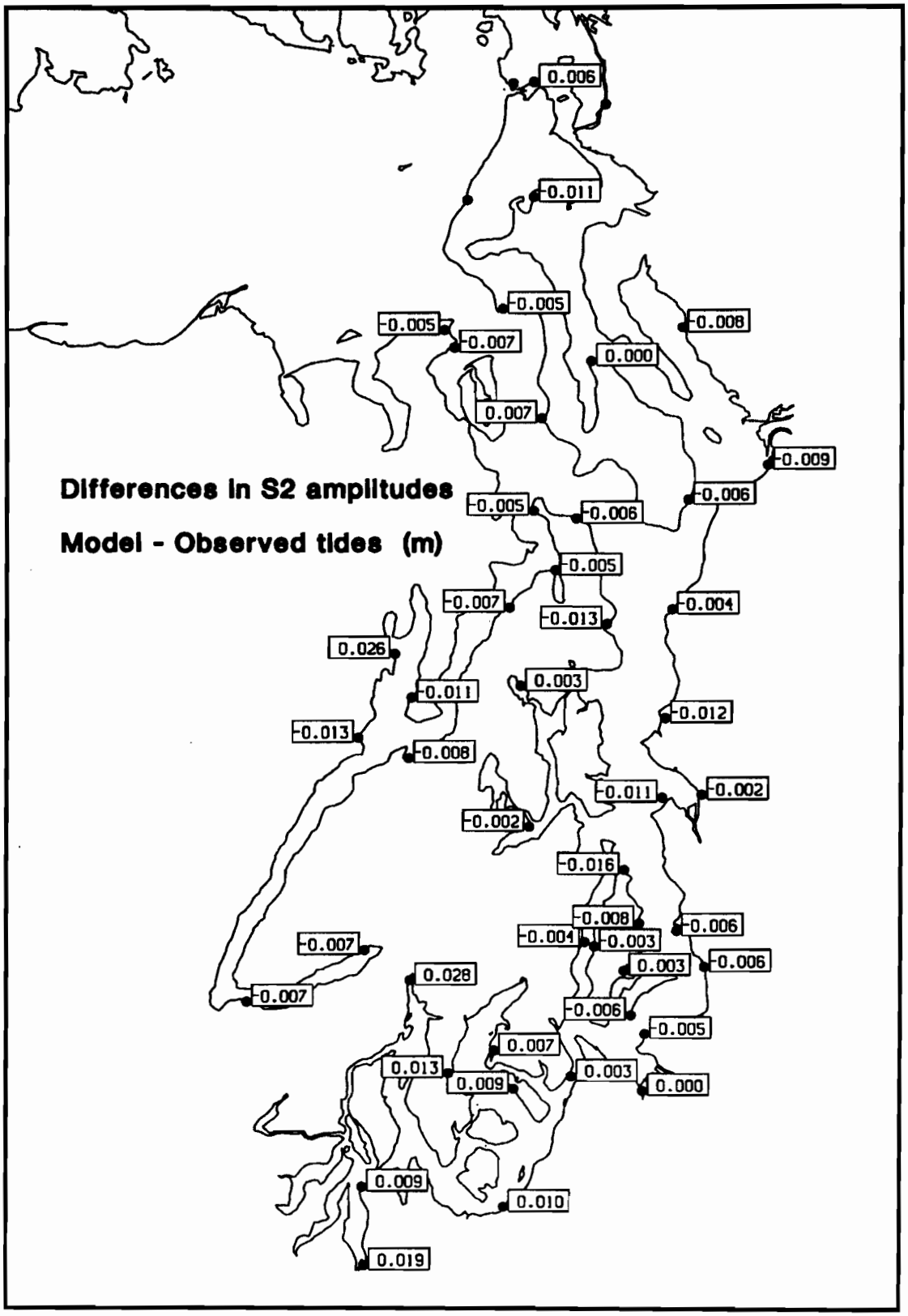

Figure 8c: Differences between modeled and observed S_2 tidal amplitudes in meters.

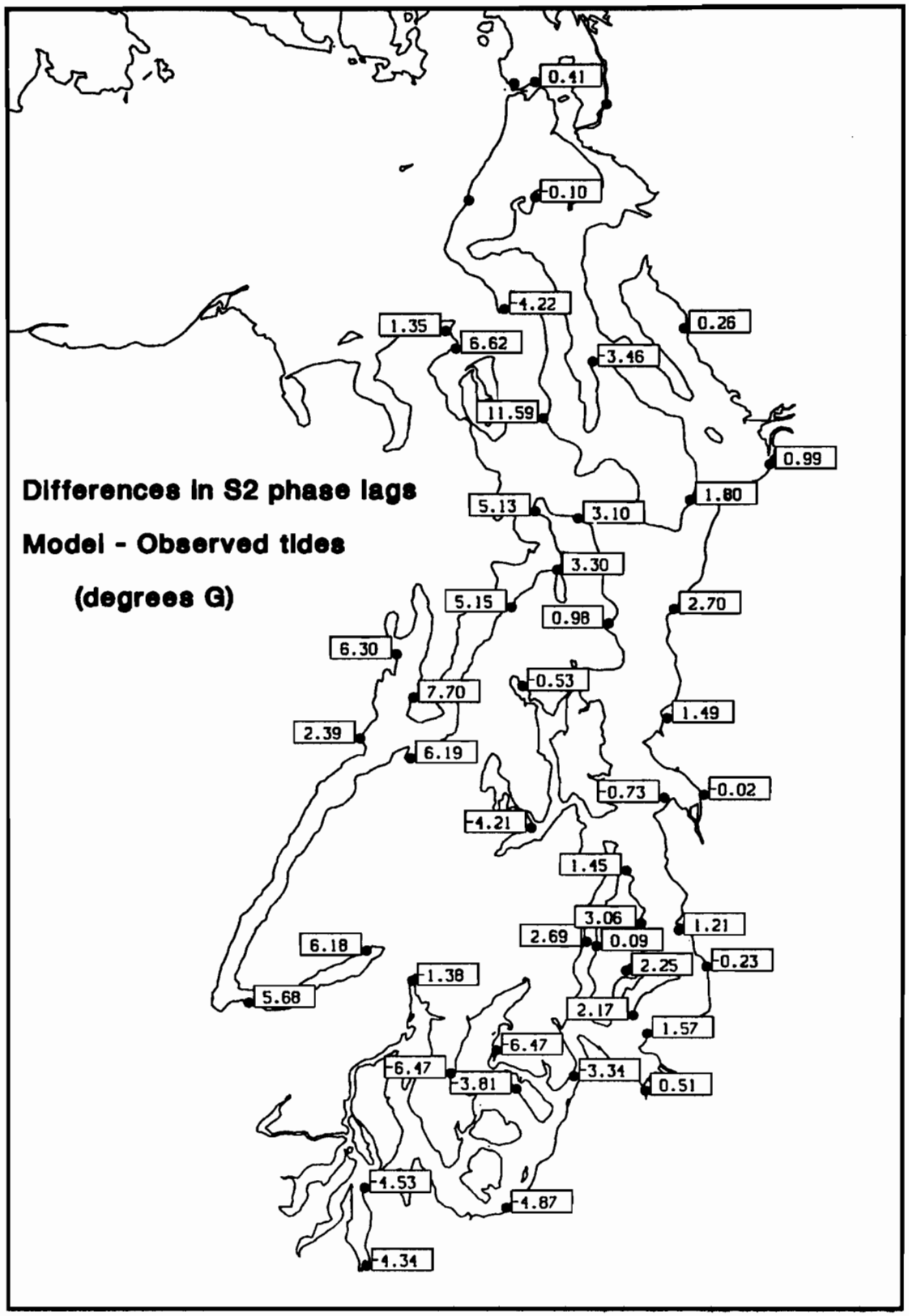

Figure 8d: Differences between modeled and observed S_2 tidal phases in degrees.

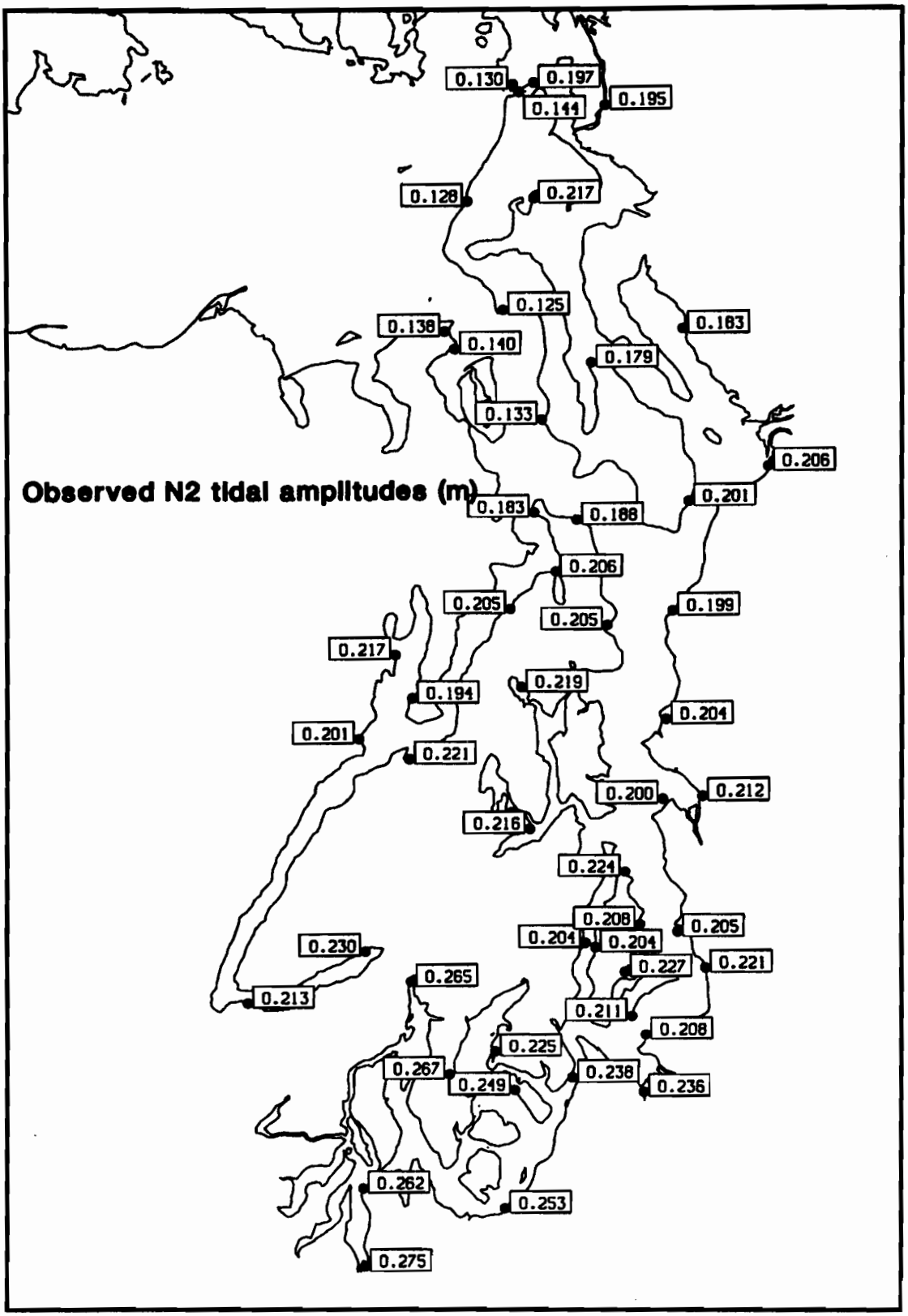

Figure 9a: Observed N_2 tidal amplitudes in meters.

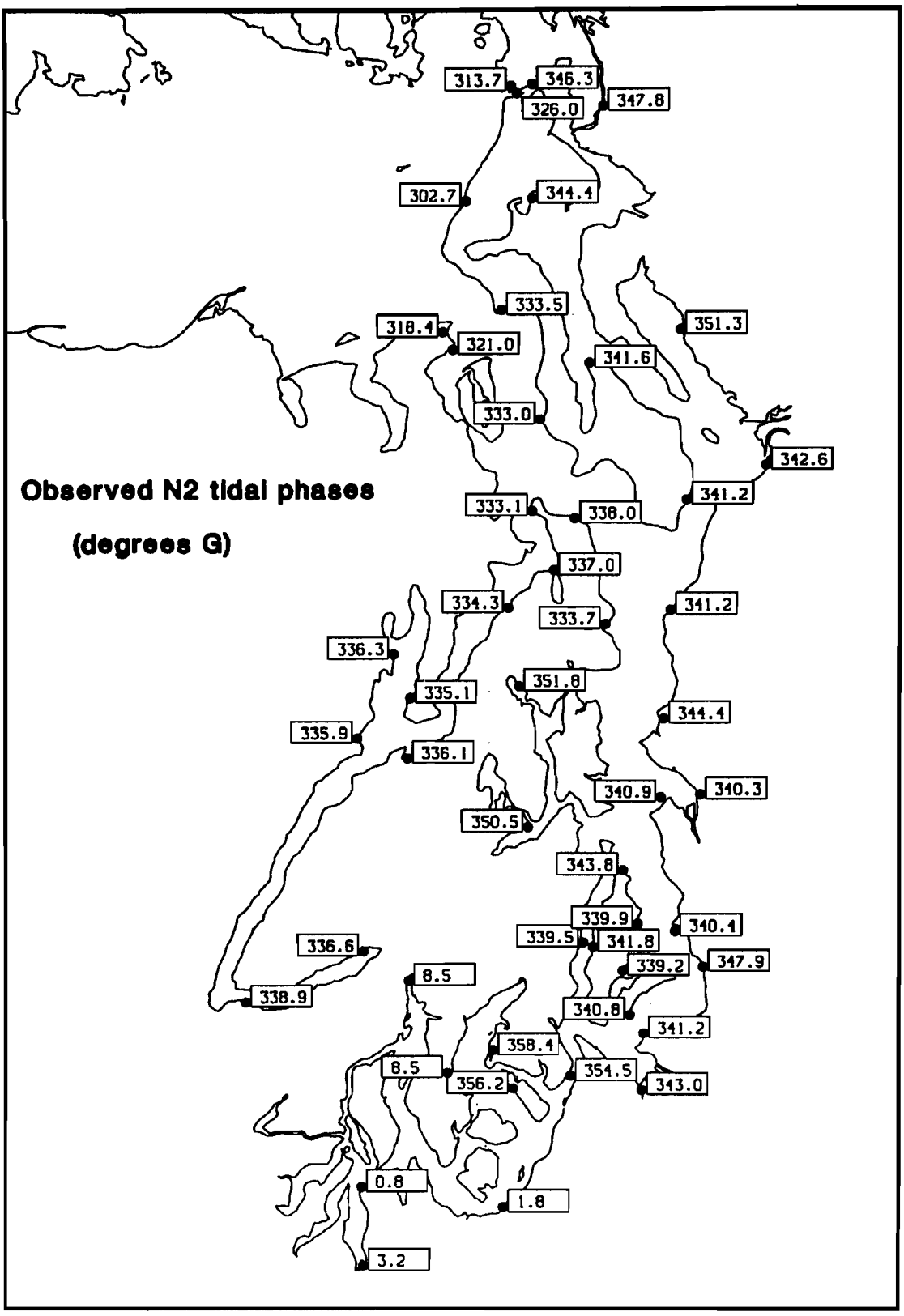

Figure 9b: Observed N_2 tidal phases in degrees. Phases are Greenwich phase lags.

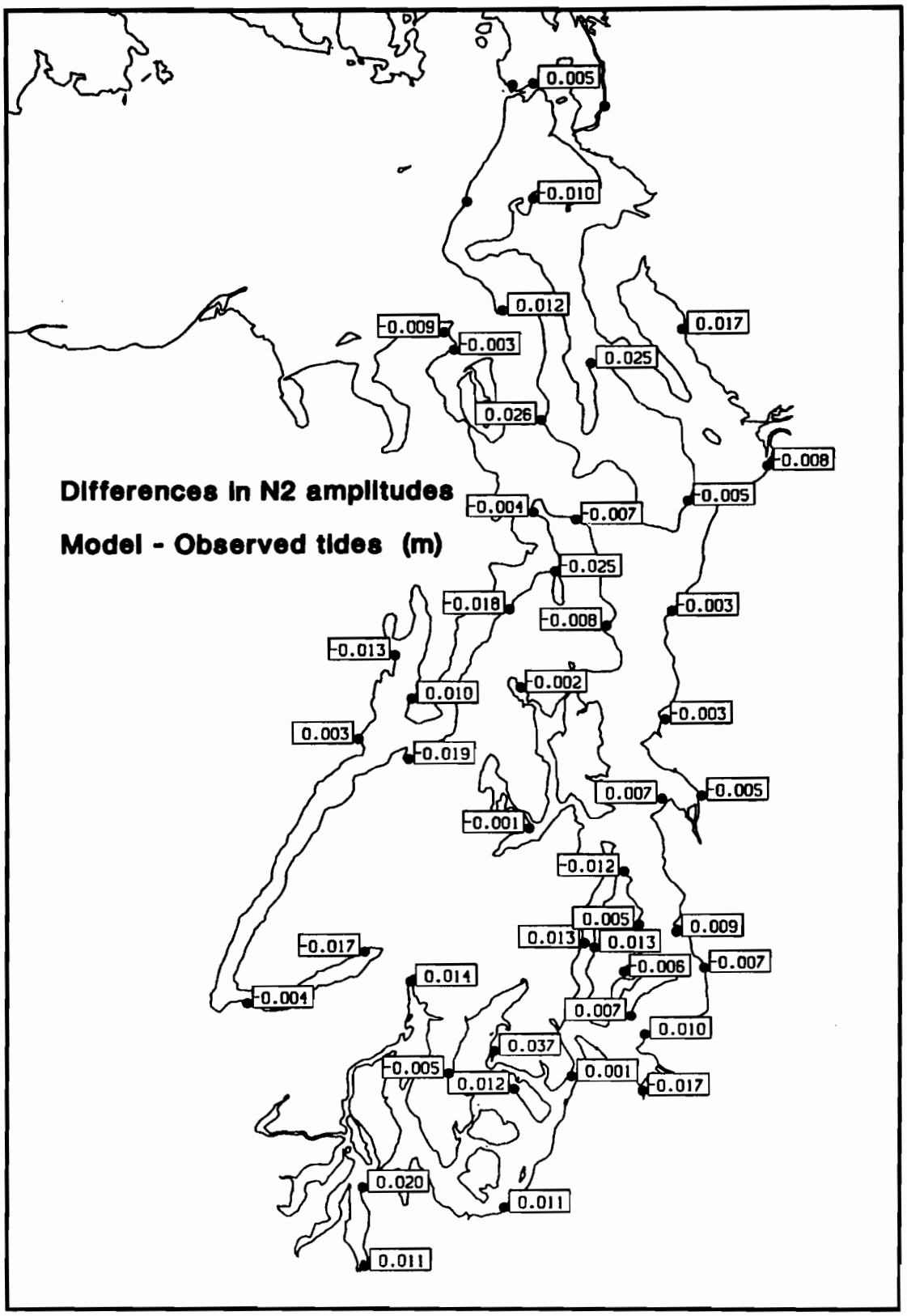

Figure 9c: Differences between modeled and observed N_2 tidal amplitudes in meters.

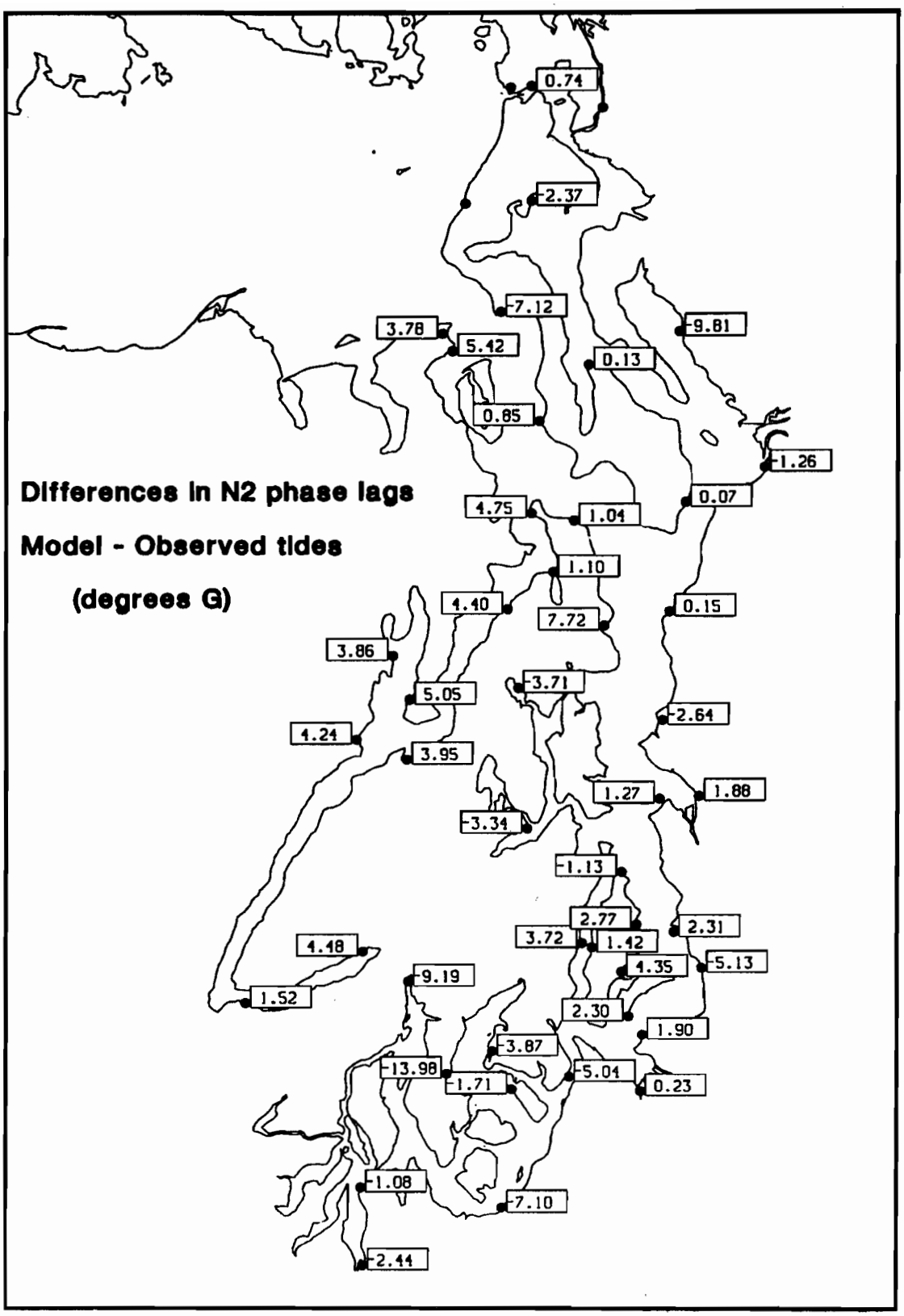

Figure 9d: Differences between modeled and observed N_2 tidal phases in degrees.

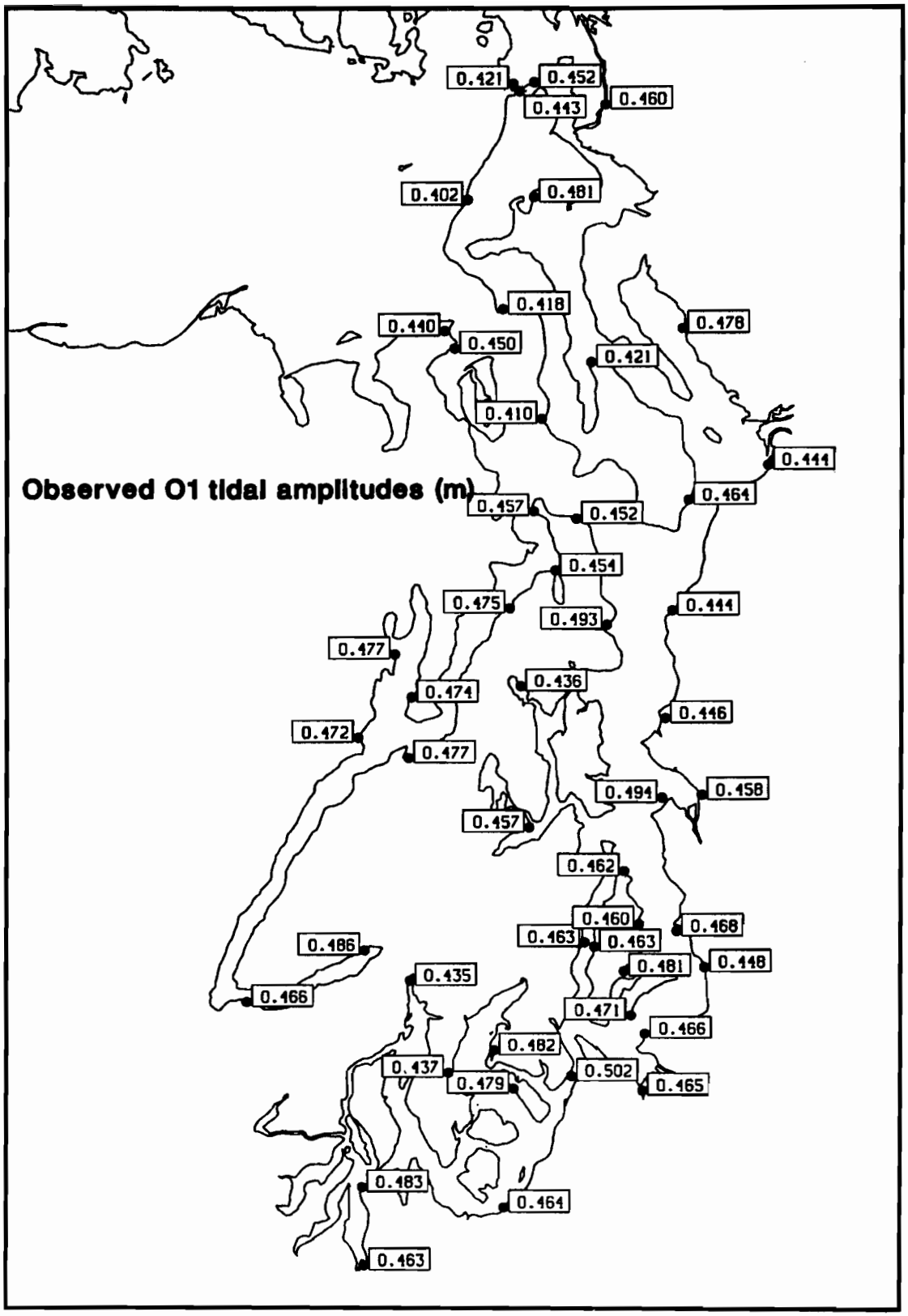

Figure 10a: Observed O_1 tidal amplitudes in meters.

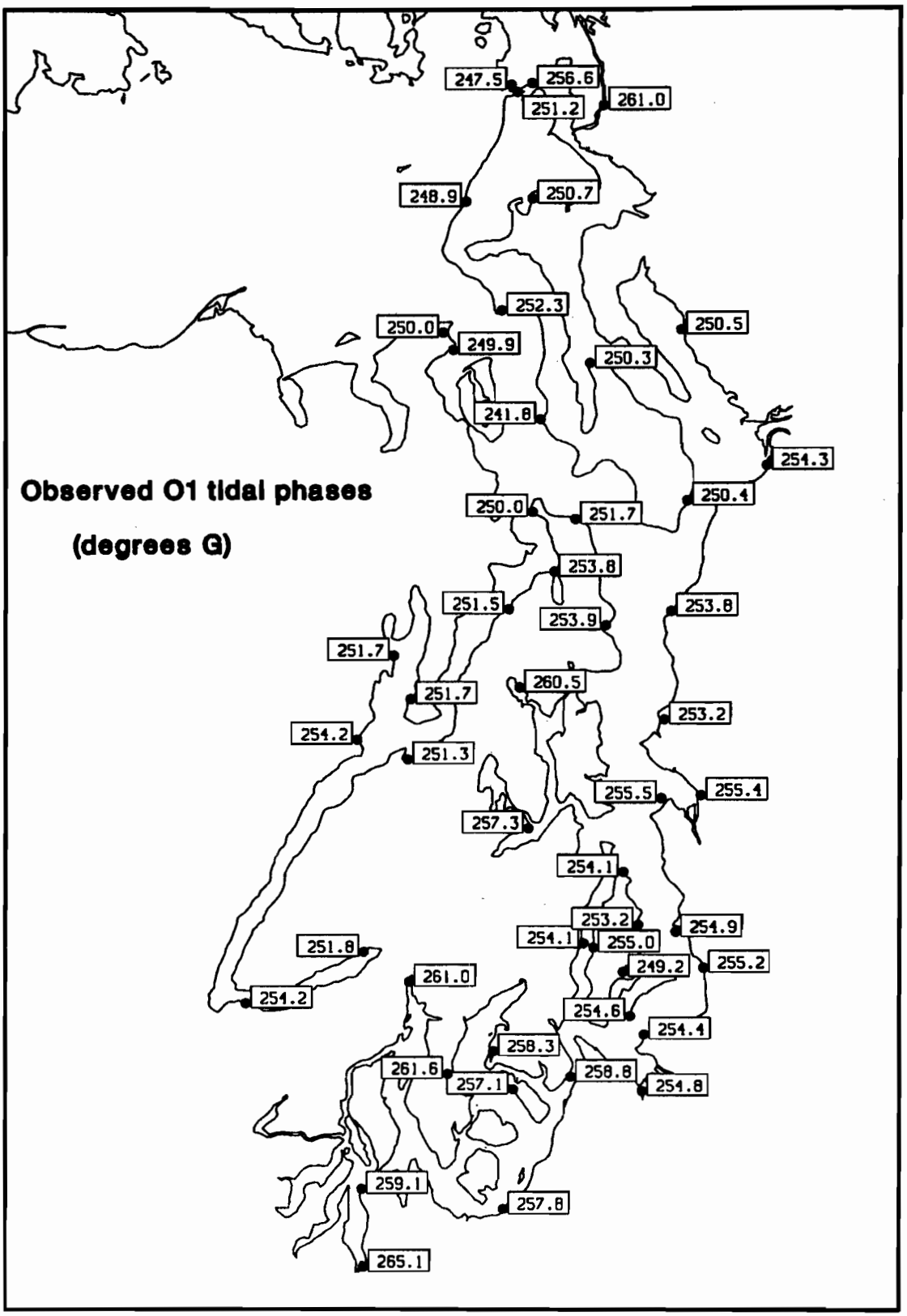

Figure 10b: Observed O_1 tidal phases in degrees. Phases are Greenwich phase lags.

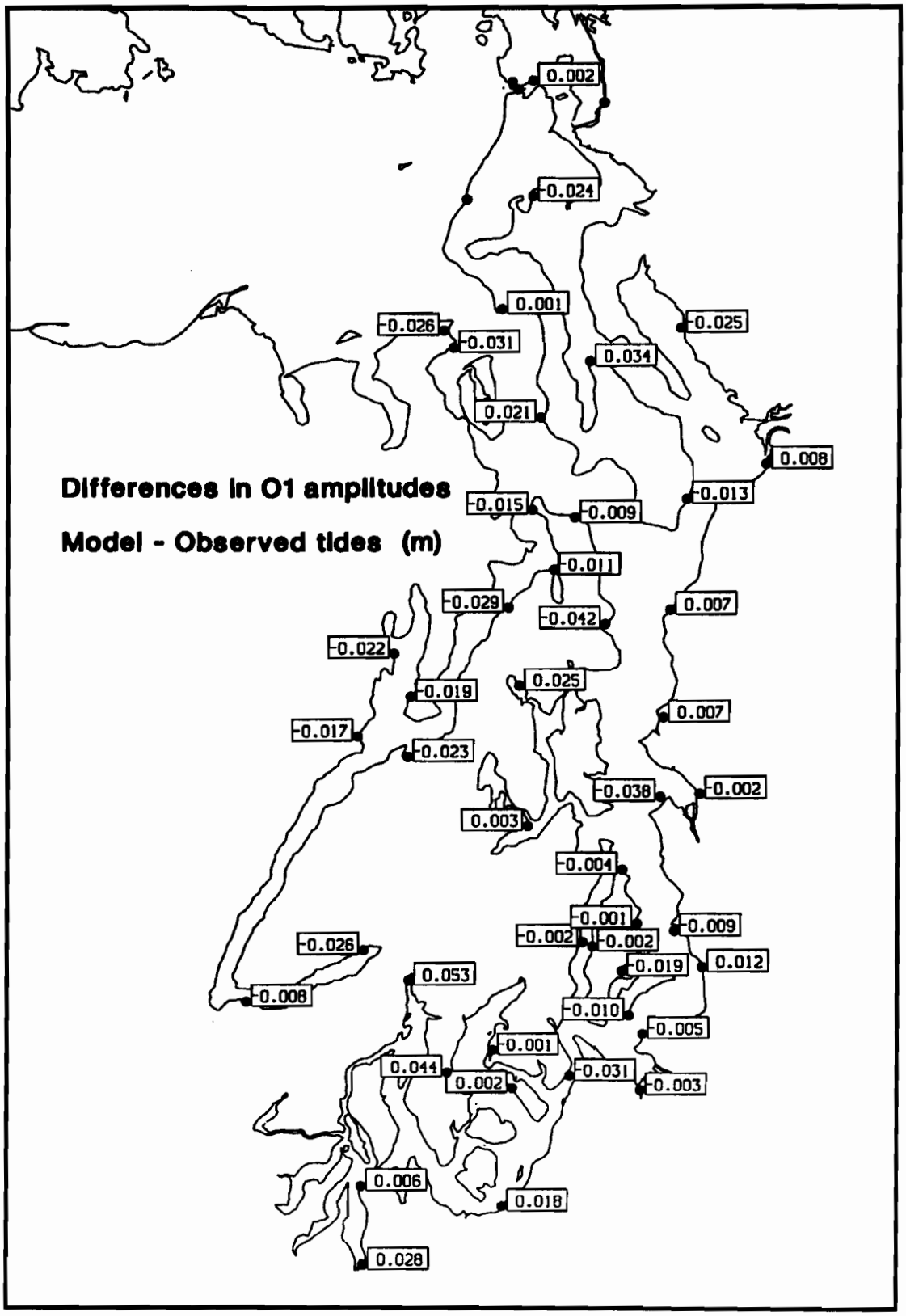

Figure 10c: Differences between modeled and observed O_1 tidal amplitudes in meters.

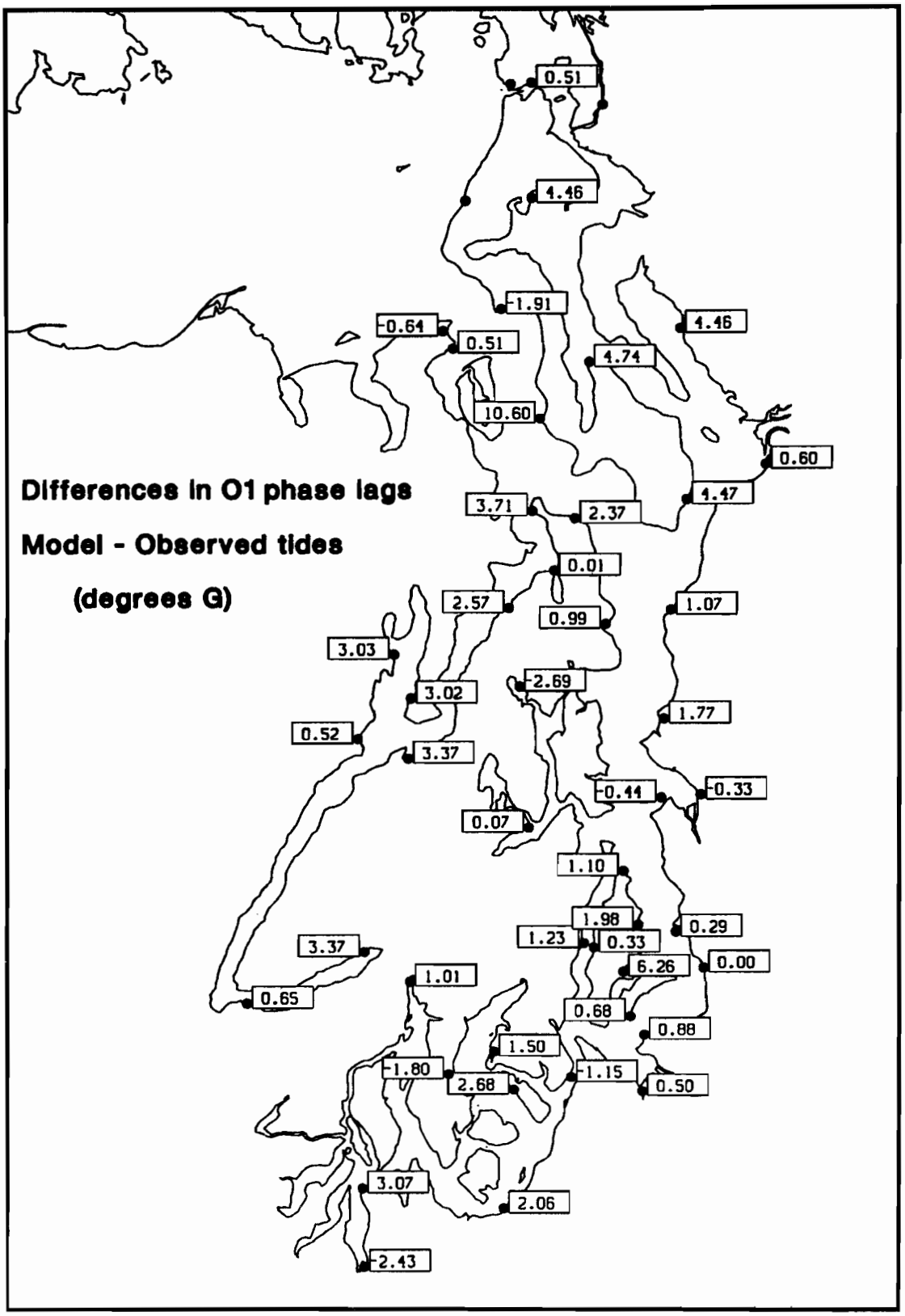

Figure 10d: Differences between modeled and observed O_1 tidal phases in degrees.

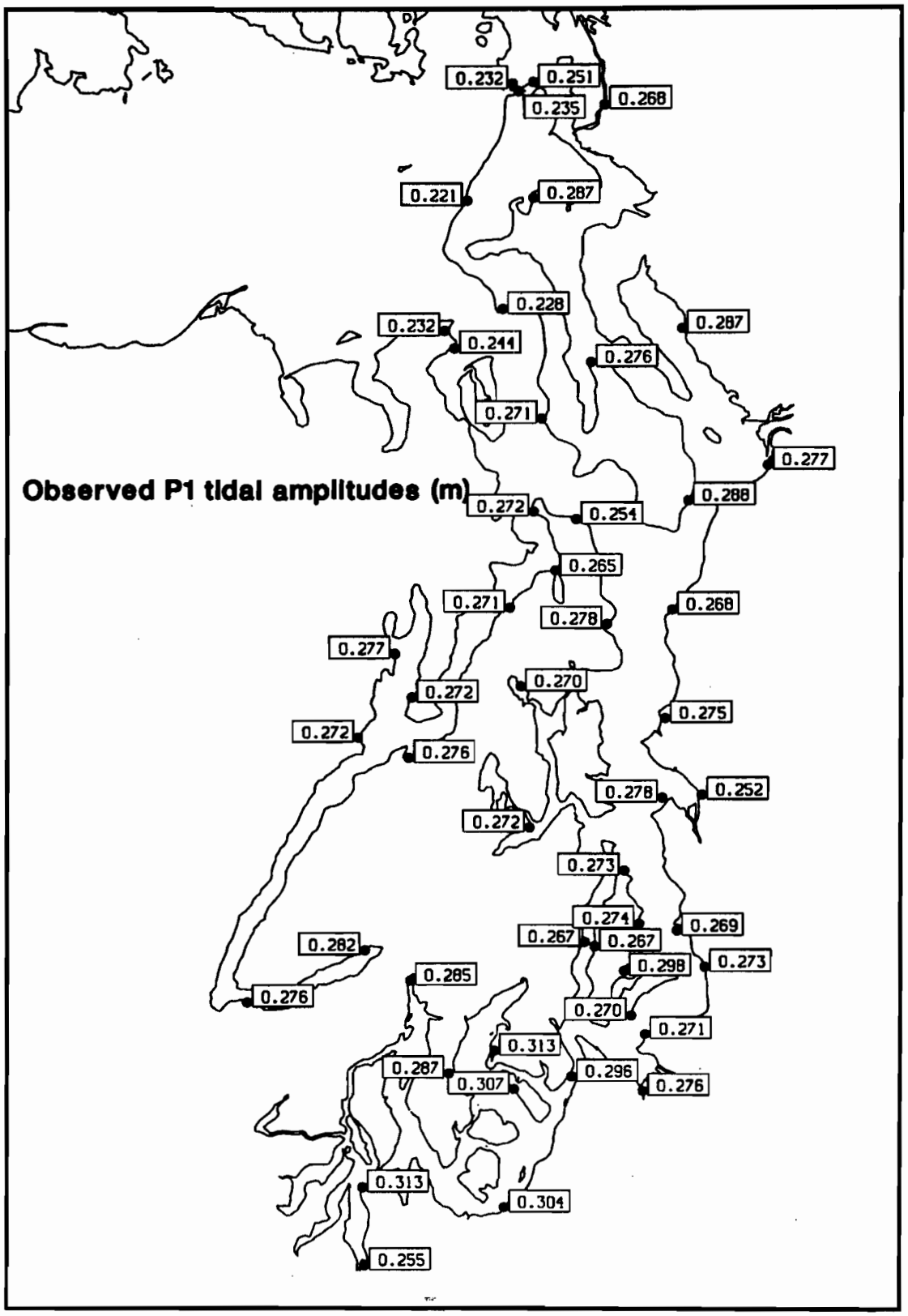

Figure 11a: Observed P_1 tidal amplitudes in meters.

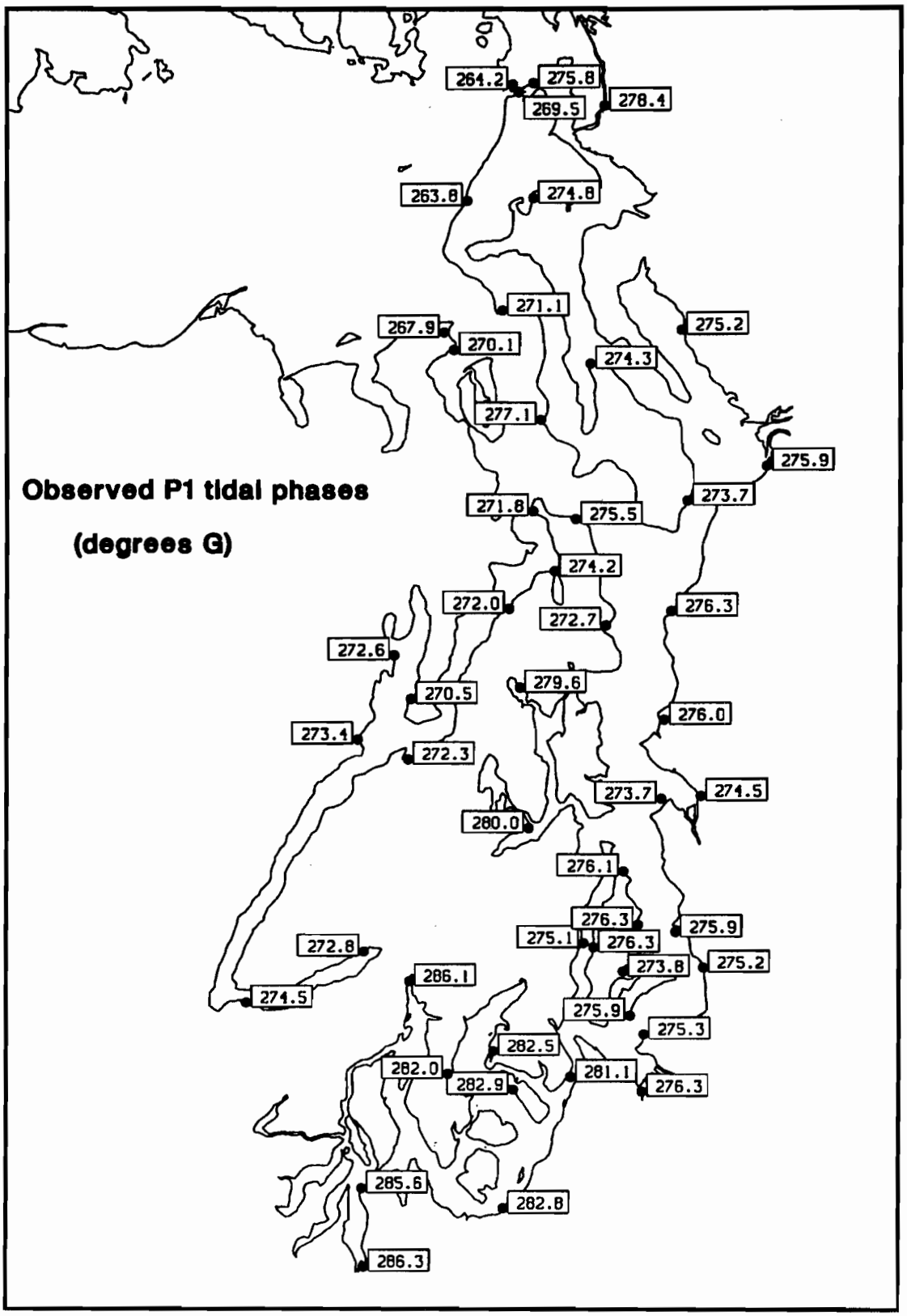

Figure 11b: Observed P_1 tidal phases in degrees. Phases are Greenwich phase lags.

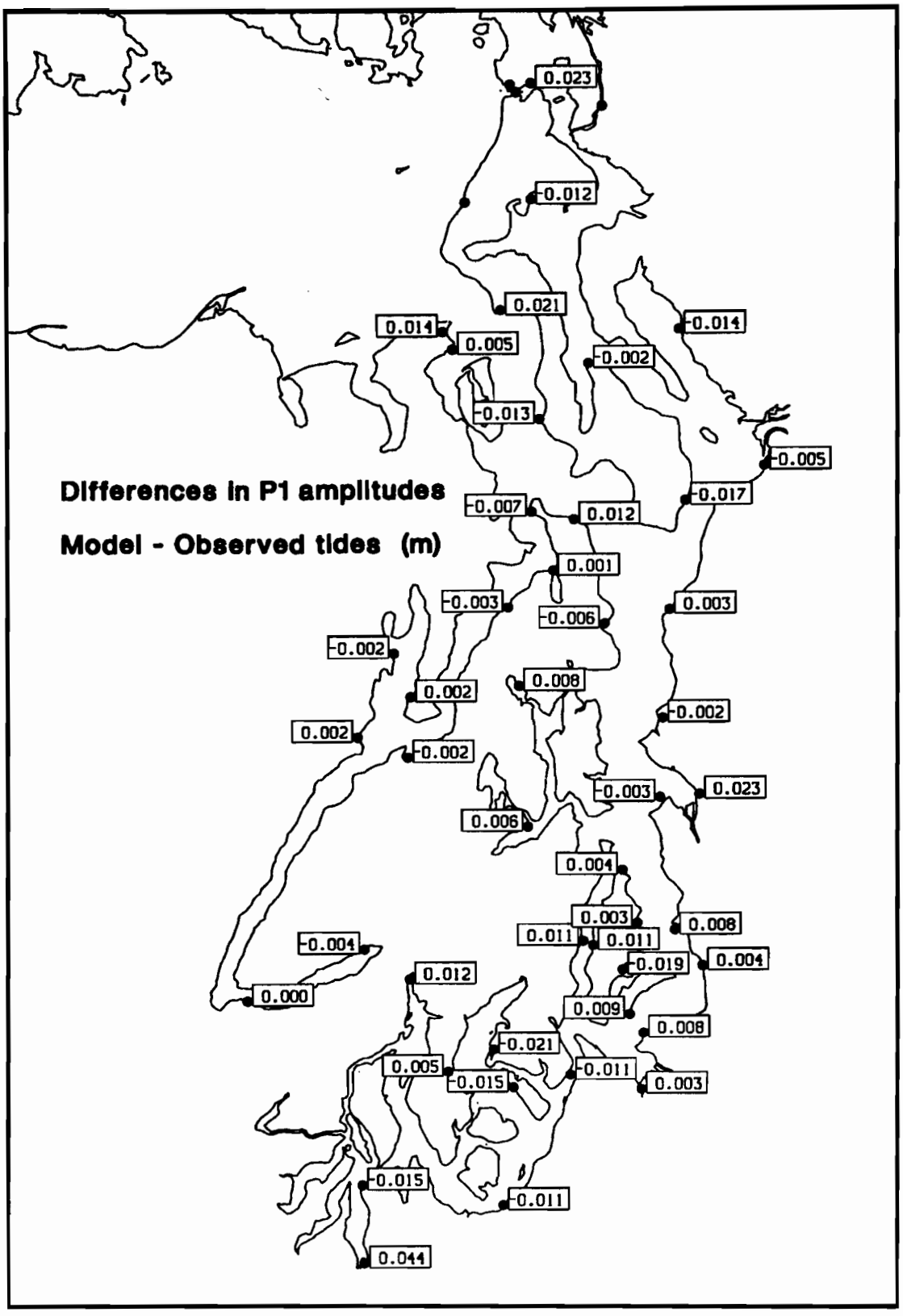

Figure 11c: Differences between modeled and observed P_1 tidal amplitudes in meters.

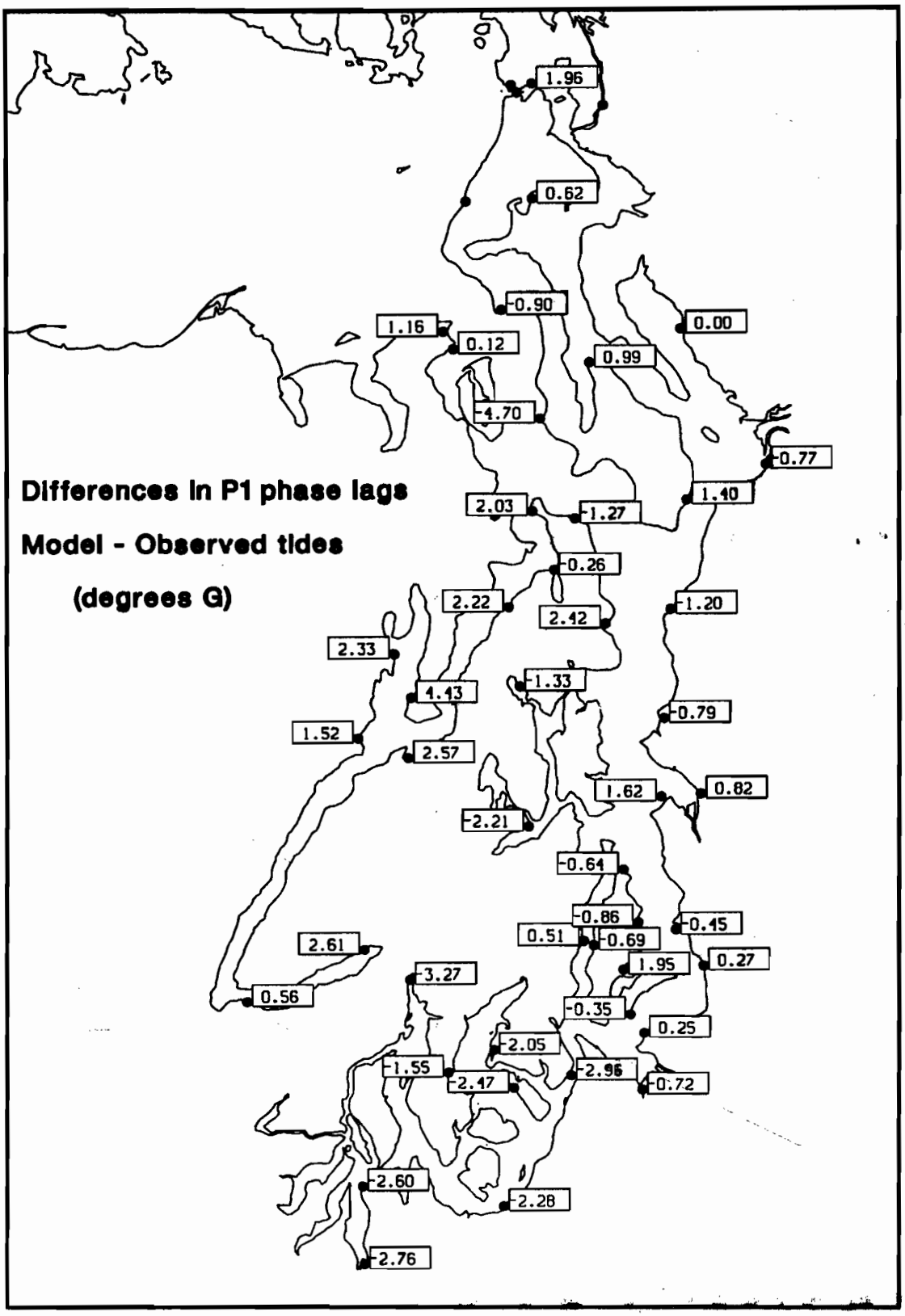

Figure 11d: Differences between modeled and observed P_1 tidal phases in degrees.

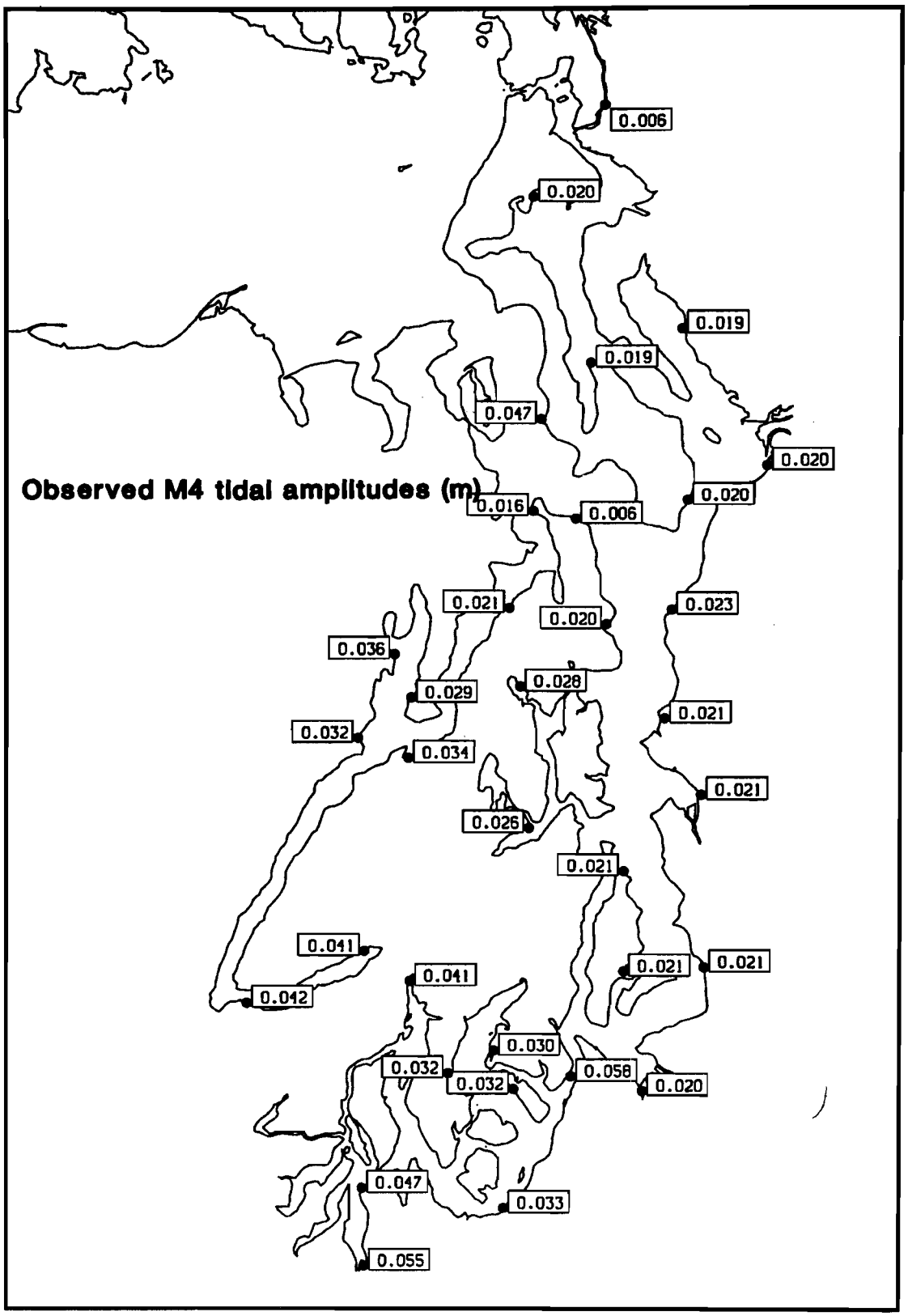

Figure 12a: Observed M_4 tidal amplitudes in meters.

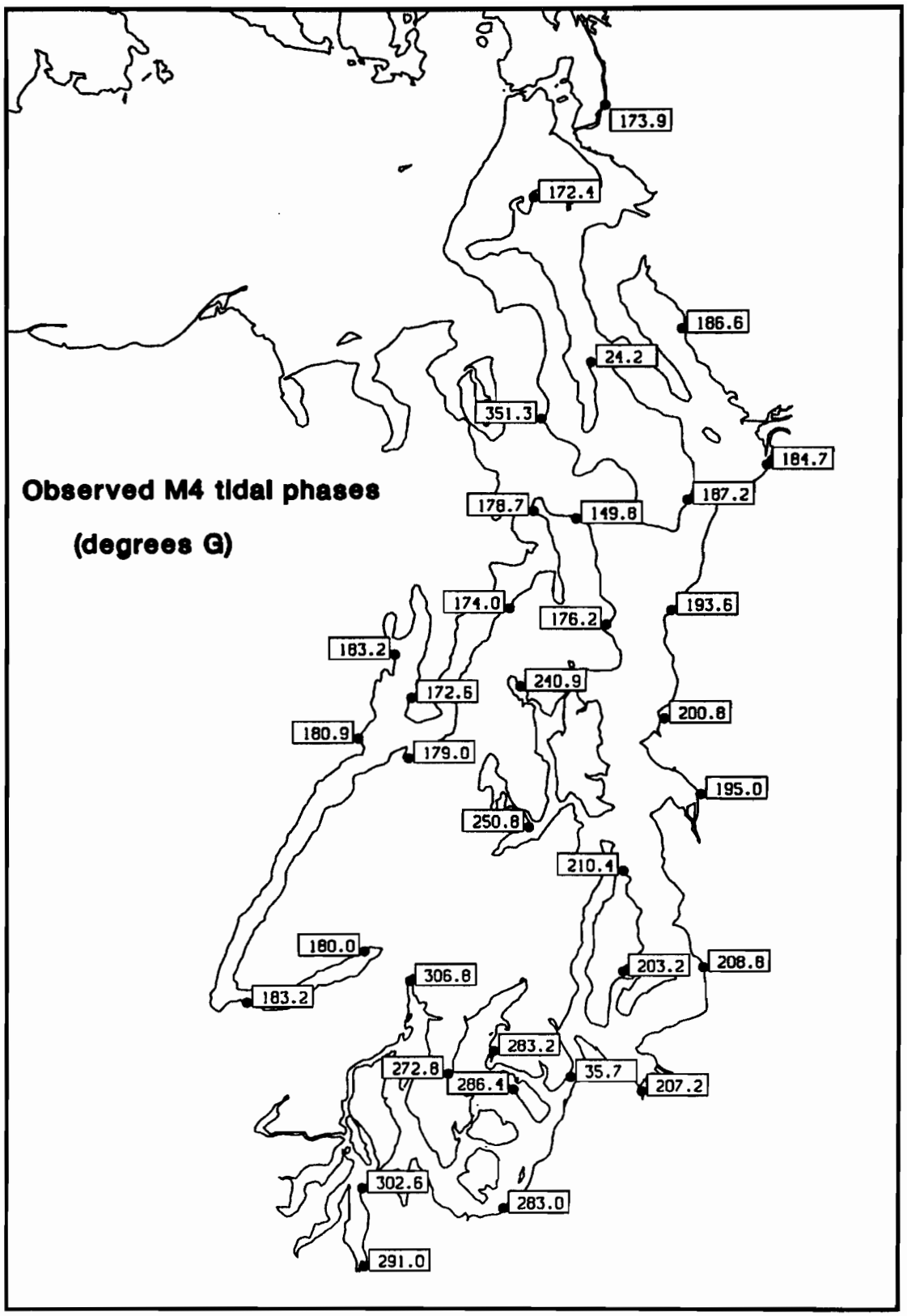

Figure 12b: Observed M_4 tidal phases in degrees. Phases are Greenwich phase lags.

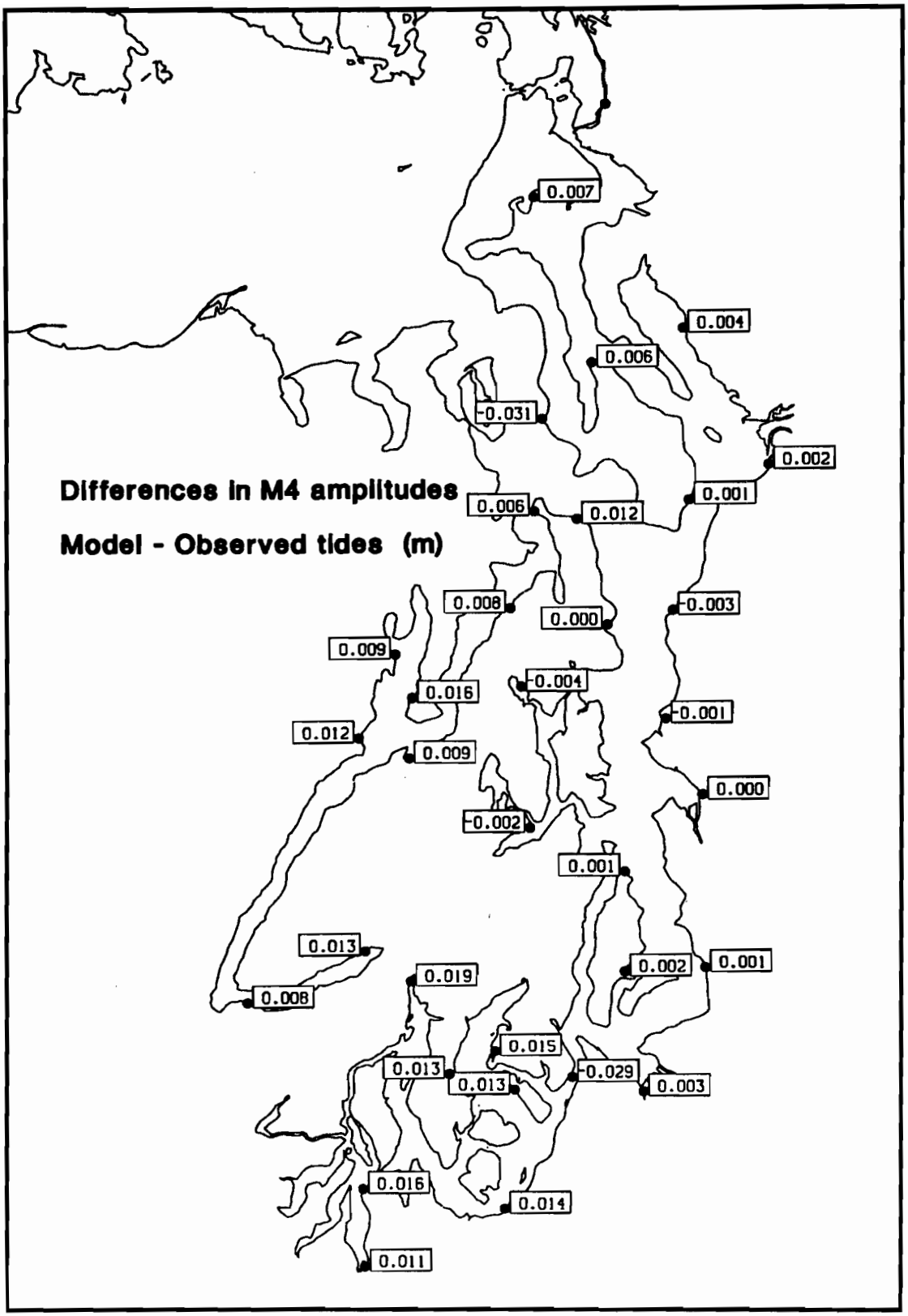

Figure 12c: Differences between modeled and observed M_4 tidal amplitudes in meters.

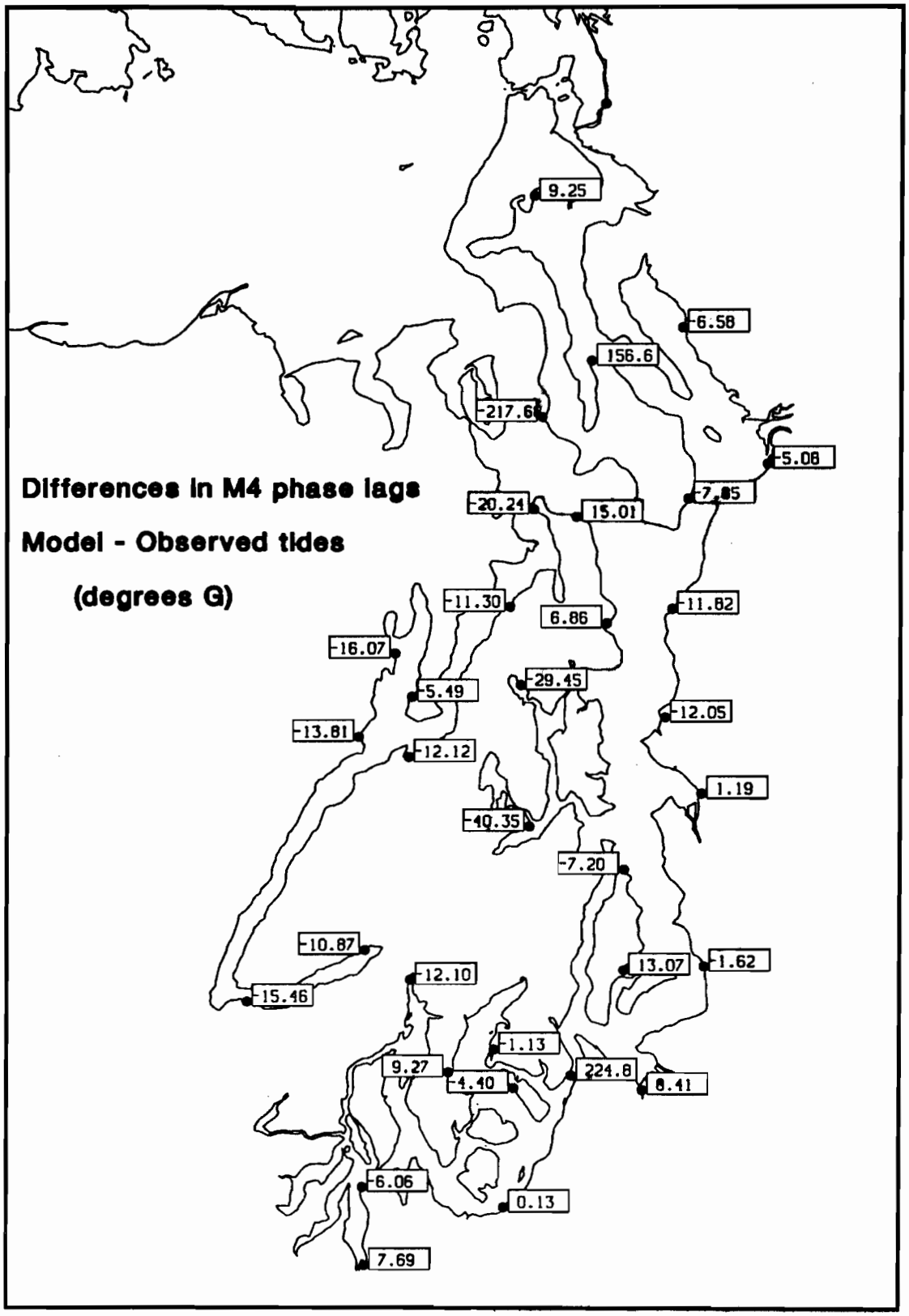

Figure 12d: Differences between modeled and observed M_4 tidal phases in degrees.

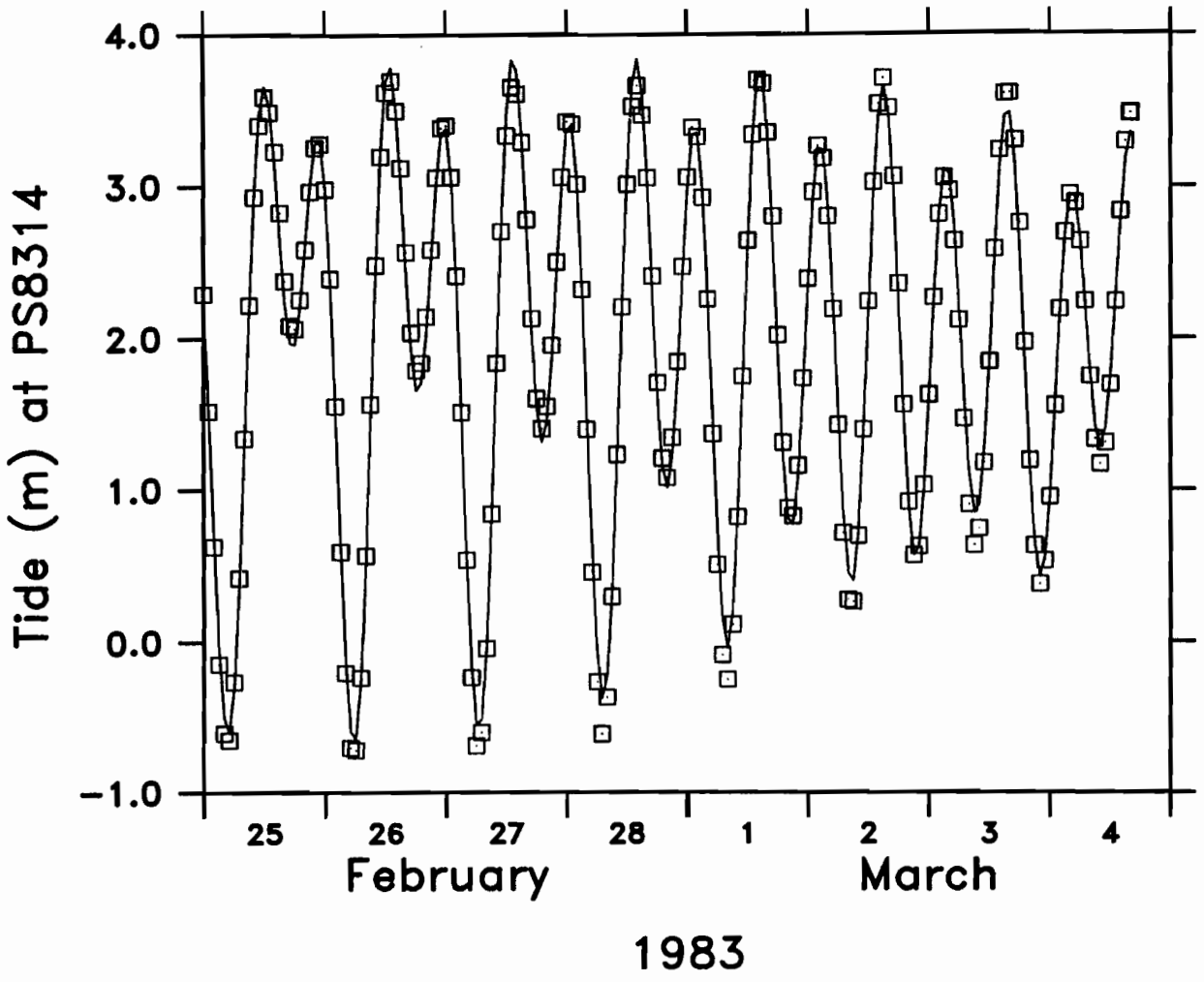

Figure 13: Observed (boxes) and predicted tidal heights (solid line) at PS8314 in southern main basin between February 25 - March 4, 1983. Observations are from a pressure gage. Predicted tidal heights are based on model results expanded to 20 tidal constituents using equilibrium tide relationships. Observational mean has been adjusted to predicted mean.

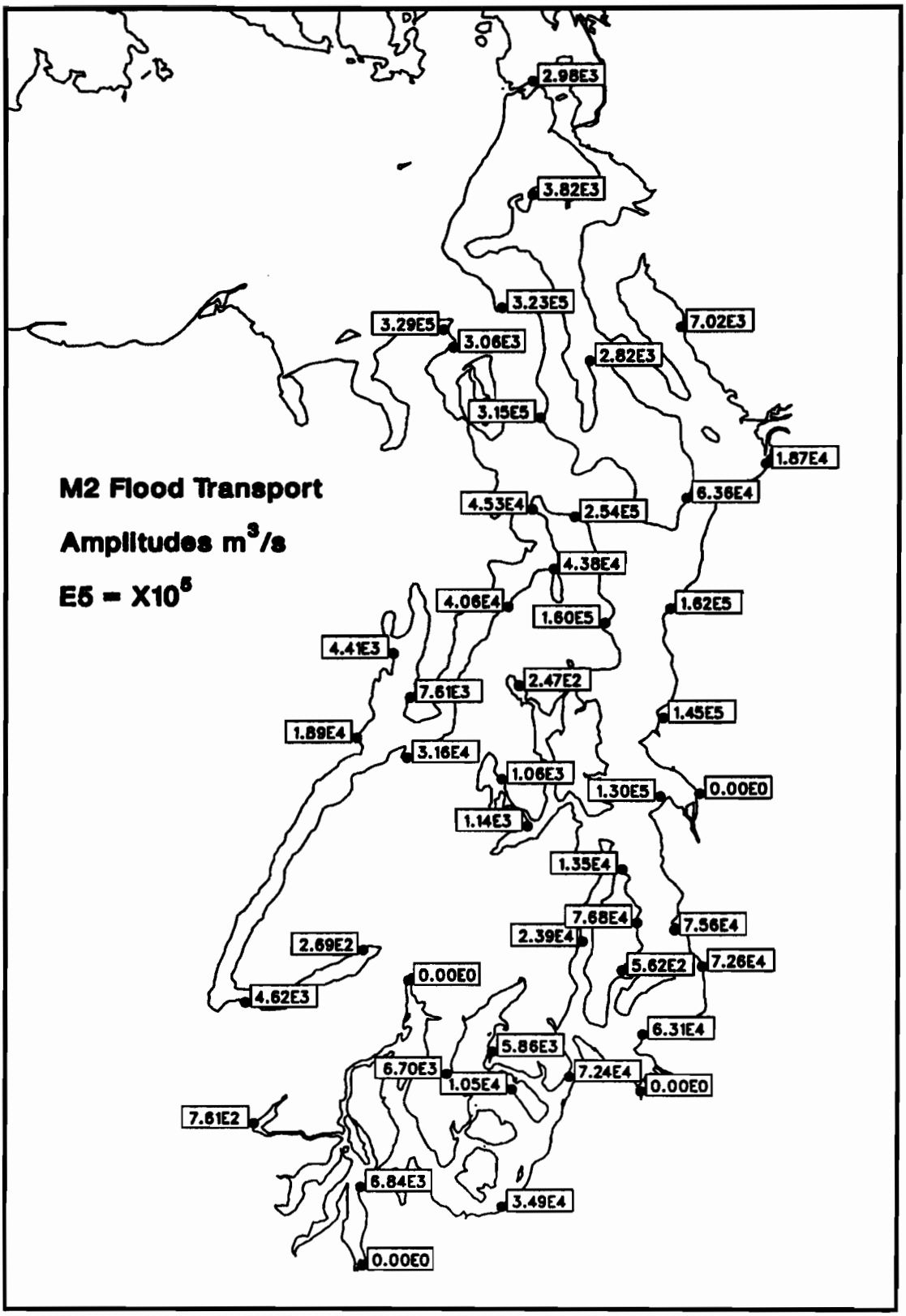

Figure 14a: M_2 transport amplitudes in m^3/s. Transports are those through channel cross-sections that terminate at the points posted. The notation for amplitudes is that, for example, 1.0E5 represents 1.0×10^5 m^3/s.

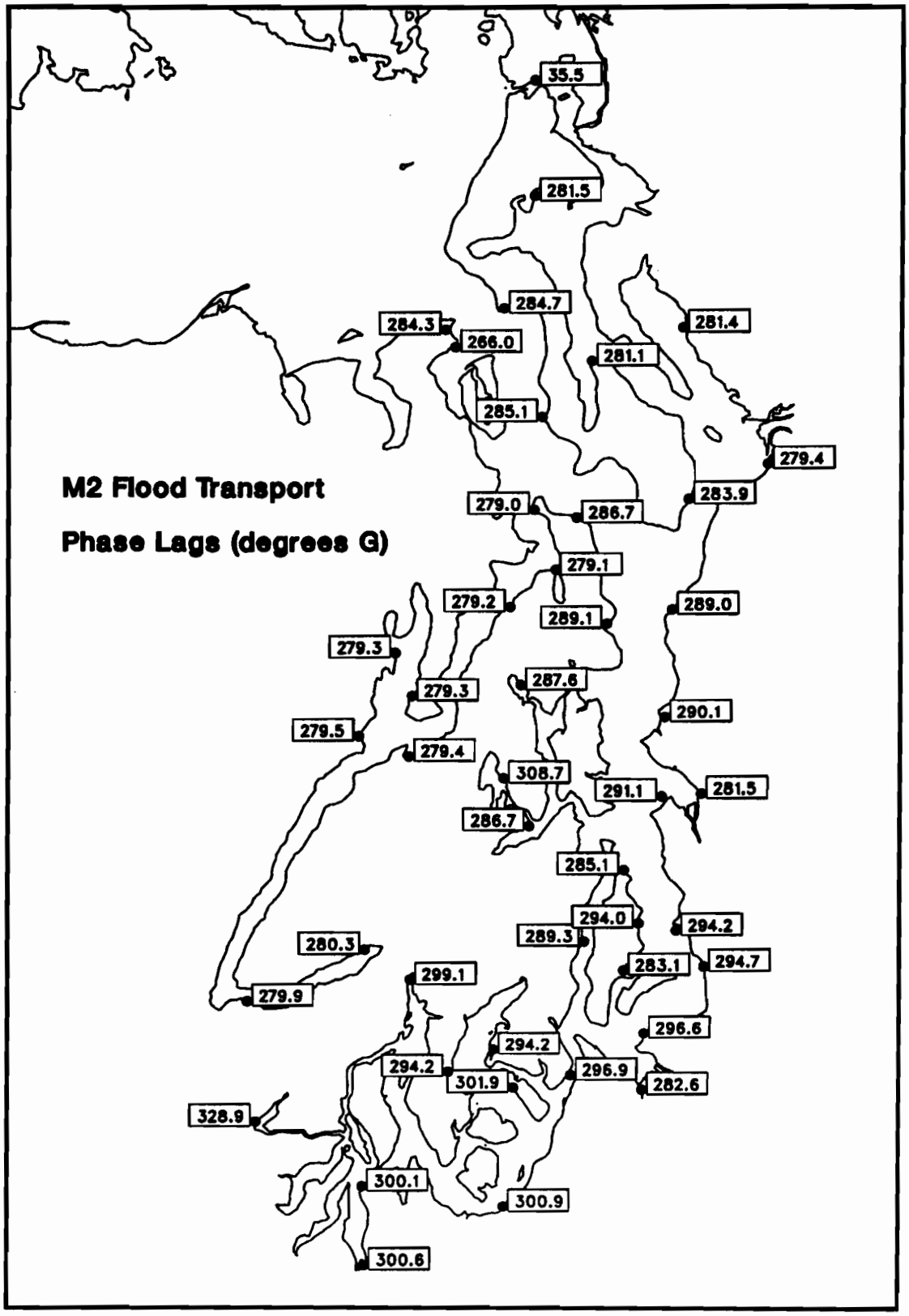

Figure 14b: M_2 transport phases in degrees. Phases are Greenwich phase lags for a flooding tide.

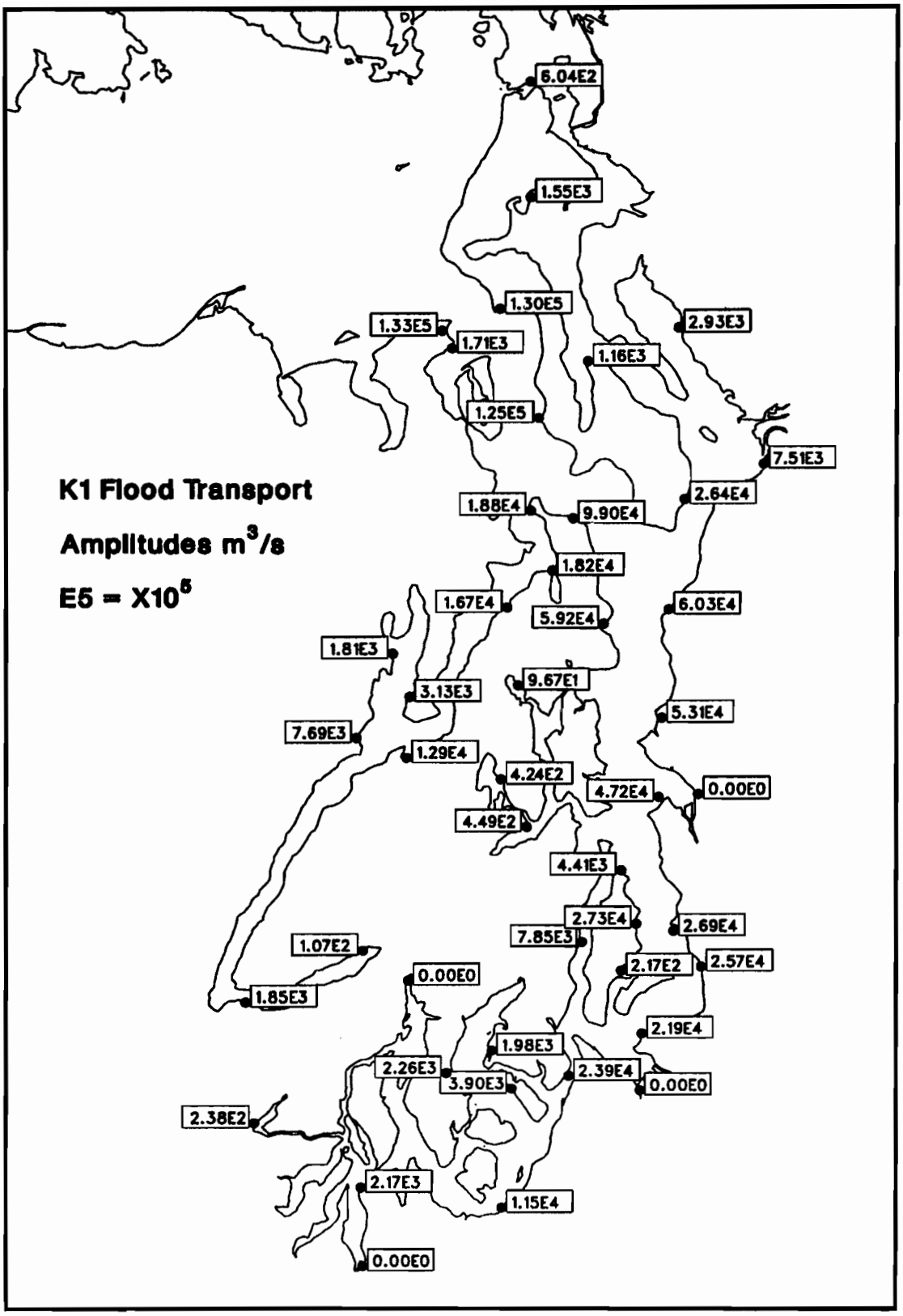

Figure 15a: K_1 transport amplitudes in m^3/s. Transports are those through channel cross-sections that terminate at the points posted. The notation for amplitude is that, for example, 1.0E5 represents 1.0×10^5 m^3/s.

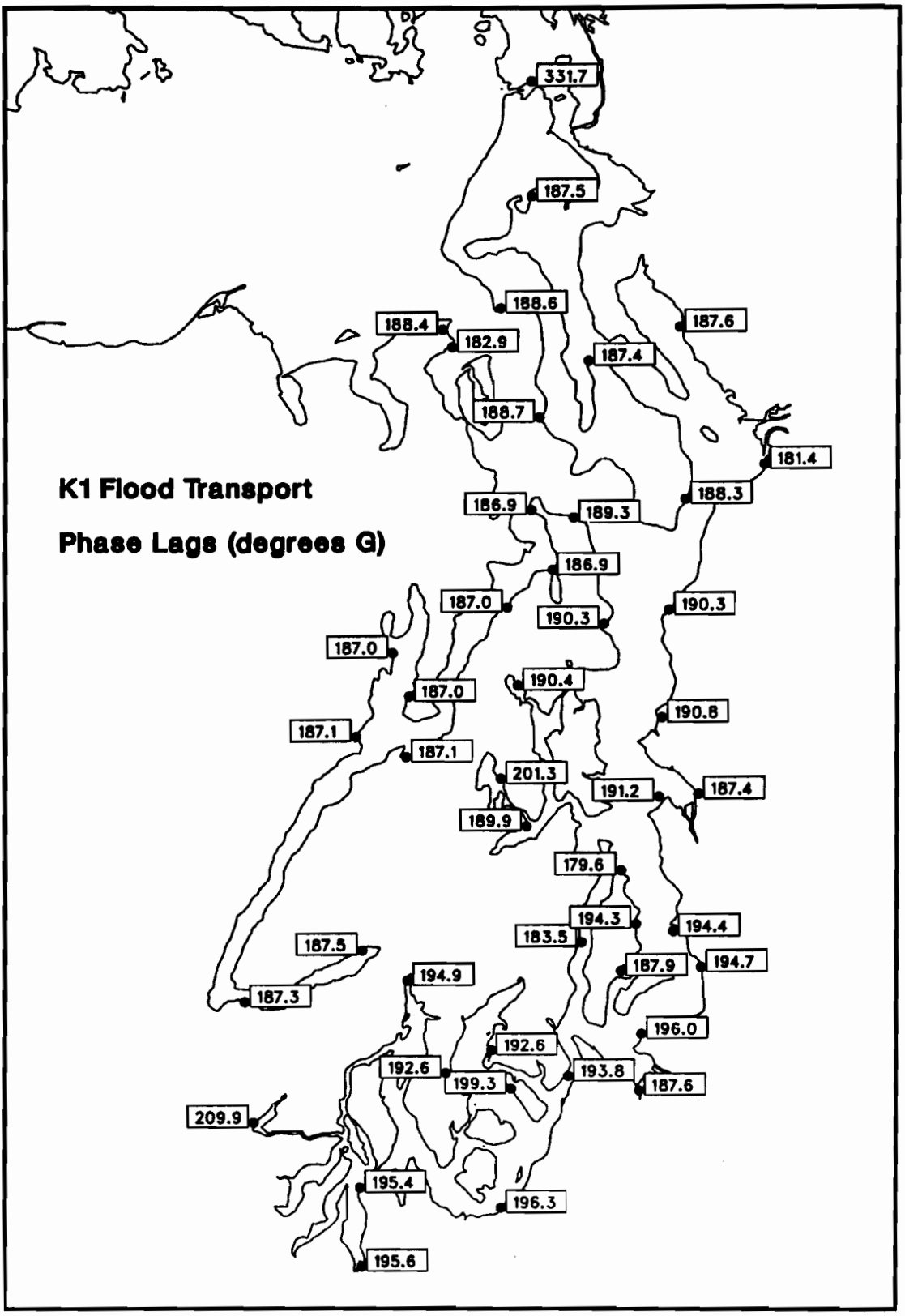

Figure 15b: K_1 transport phases in degrees. Phases are Greenwich phase lags for a flooding tide.

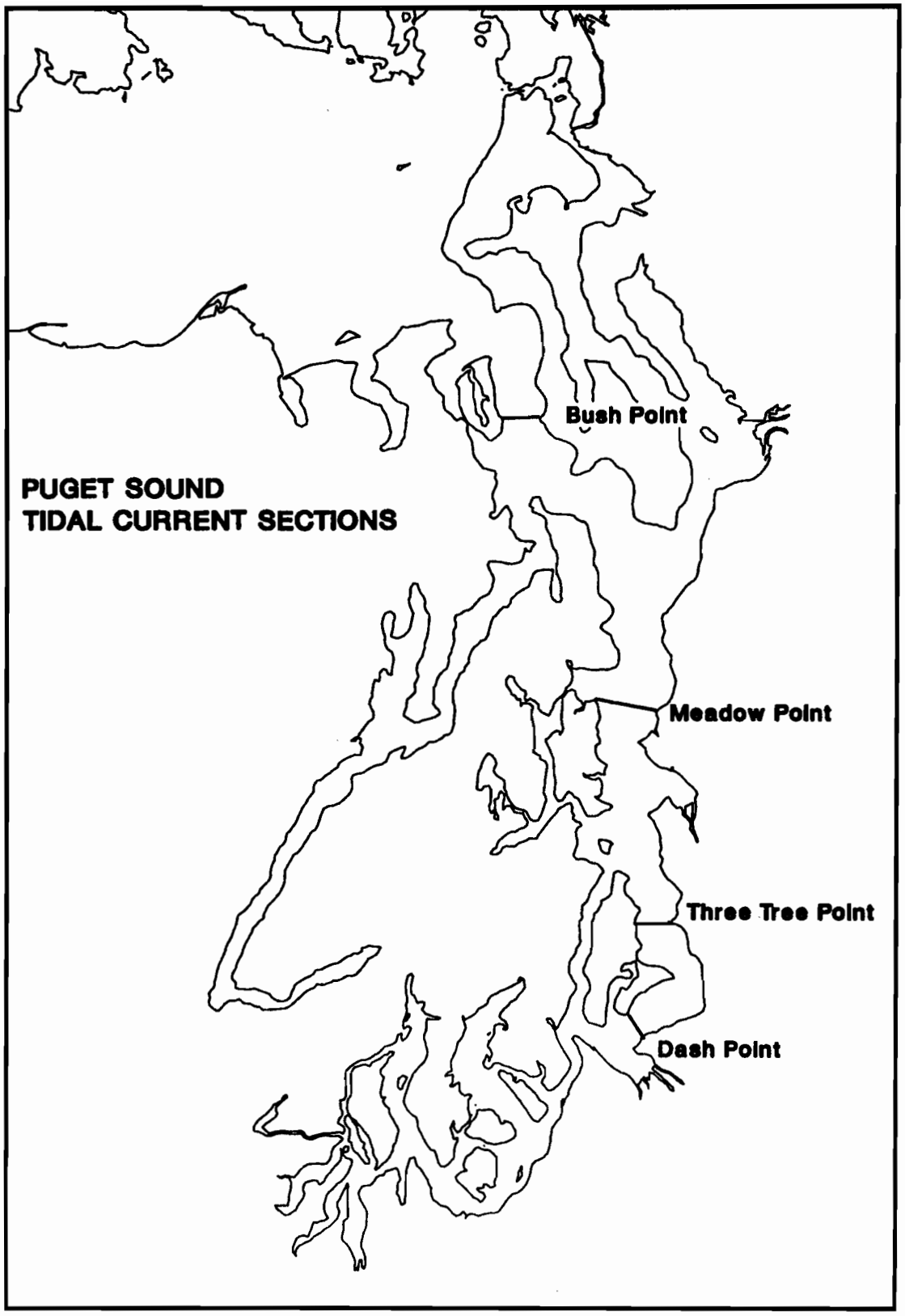

Figure 16: Locations at which cross-sectional arrays of current meters have been situated. Observed currents through these cross sections permit the evaluation of tidal transports at M_2 and K_1 frequencies.

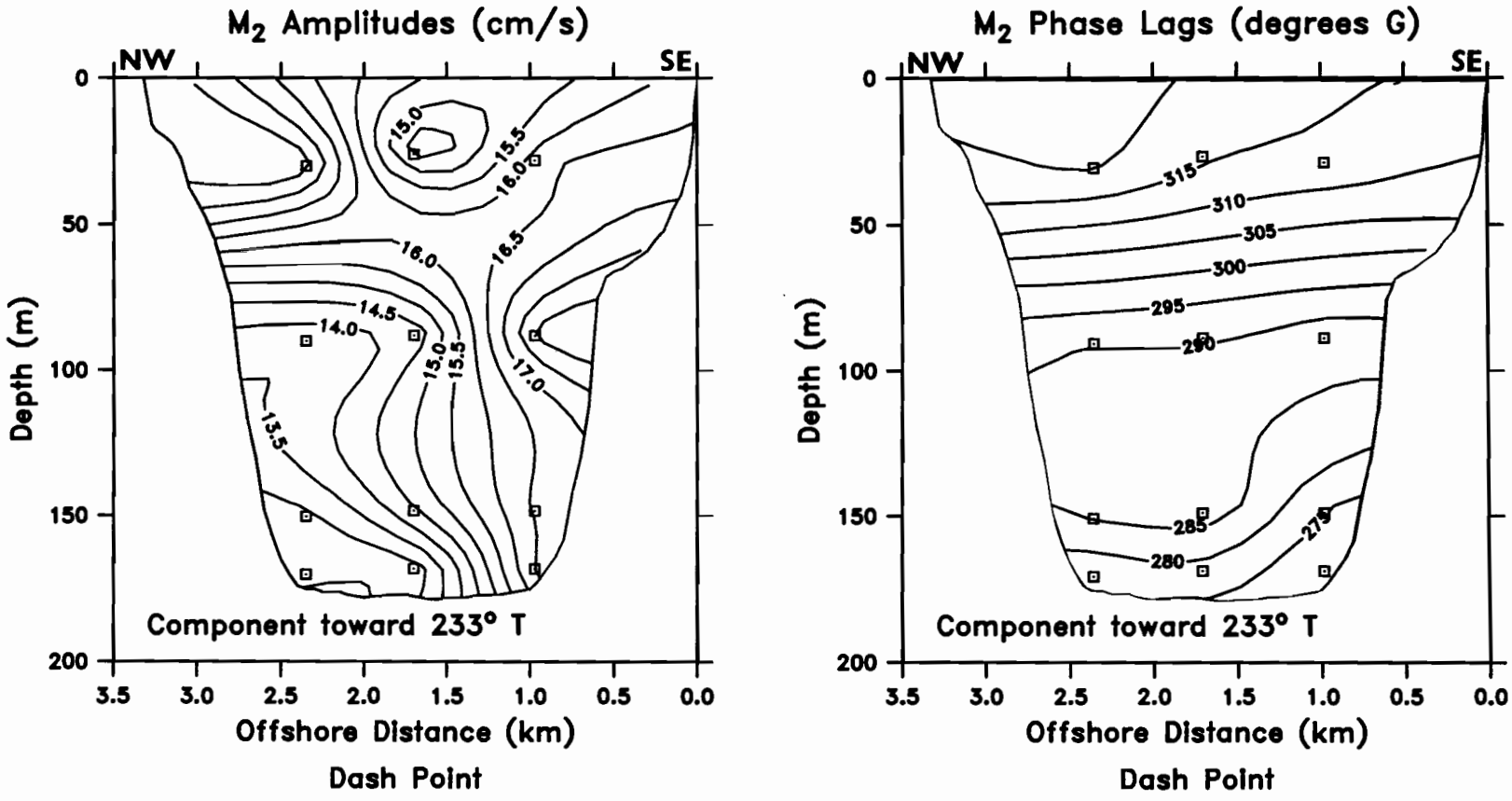

Figure 17: Observed M_2 tidal current amplitudes and phases for a channel cross-section off Dash Point. Amplitudes in cm/s and phases in degrees. Phases are Greenwich phase lags for a flood tide. Location of current meters are indicated by squares. Vertical exaggeration is 17:1.

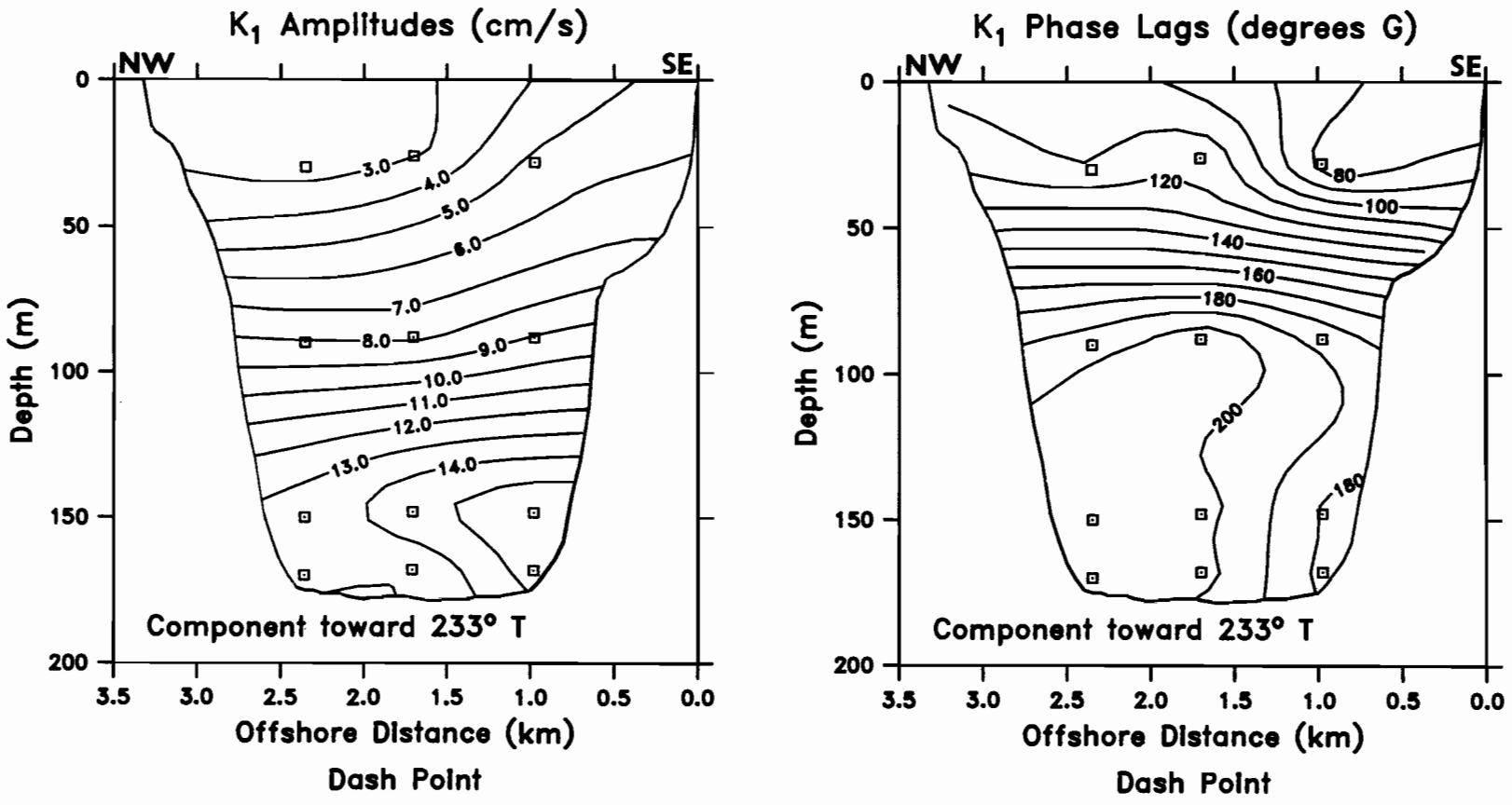

Figure 18: Observed K_1 tidal current amplitudes and phases for a channel cross-section off Dash Point. Amplitudes in cm/s and phases in degrees. Phases are Greenwich phase lags for a flood tide. Location of current meters are indicated by squares. Vertical exaggeration is 17:1.

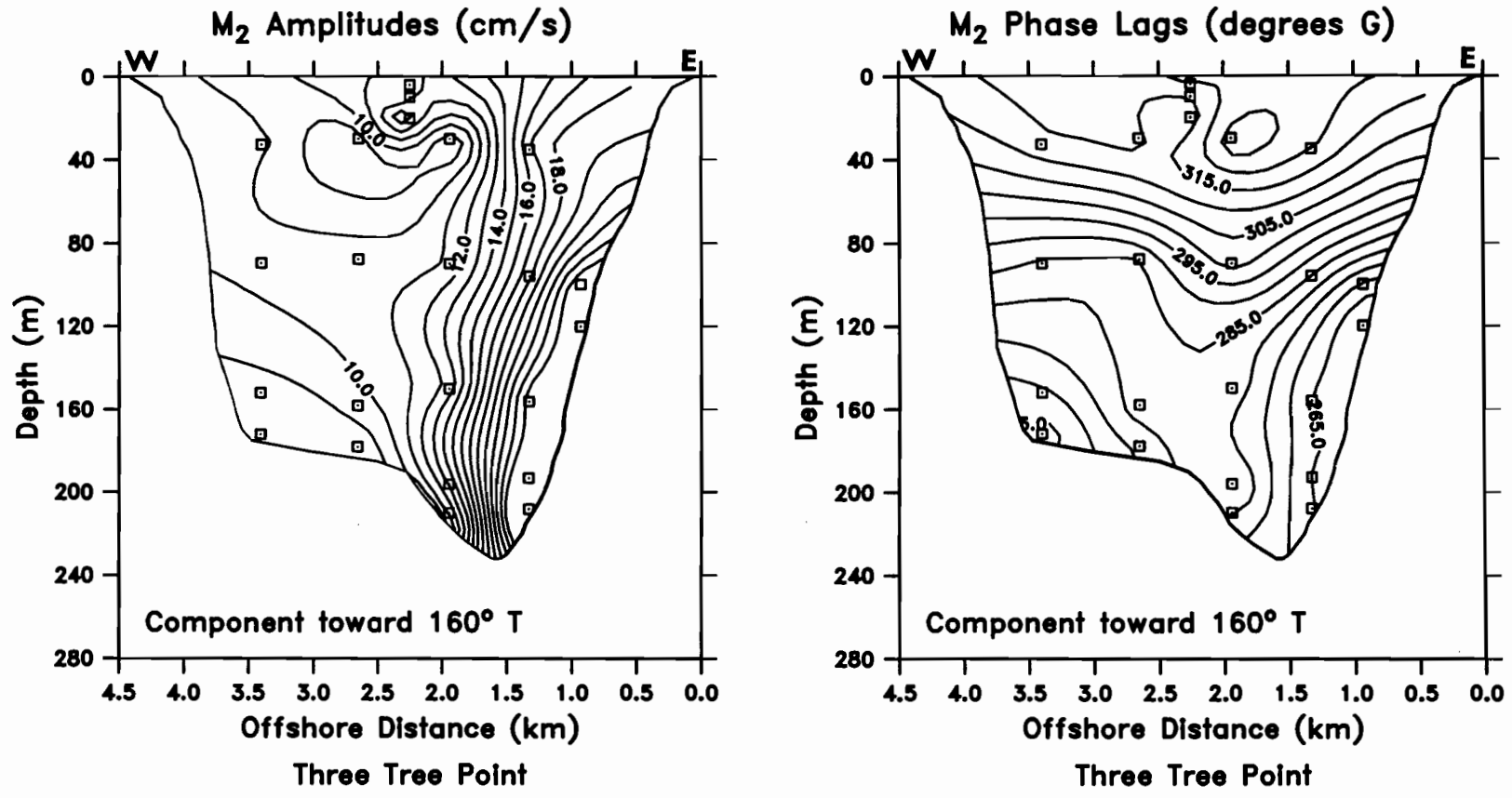

Figure 19: Observed M_2 tidal current amplitudes and phases for a channel cross-section off Three Tree Point. Amplitudes in cm/s and phases in degrees. Phases are Greenwich phase lags for a flood tide. Location of current meters are indicated by squares. Vertical exaggeration is 16:1.

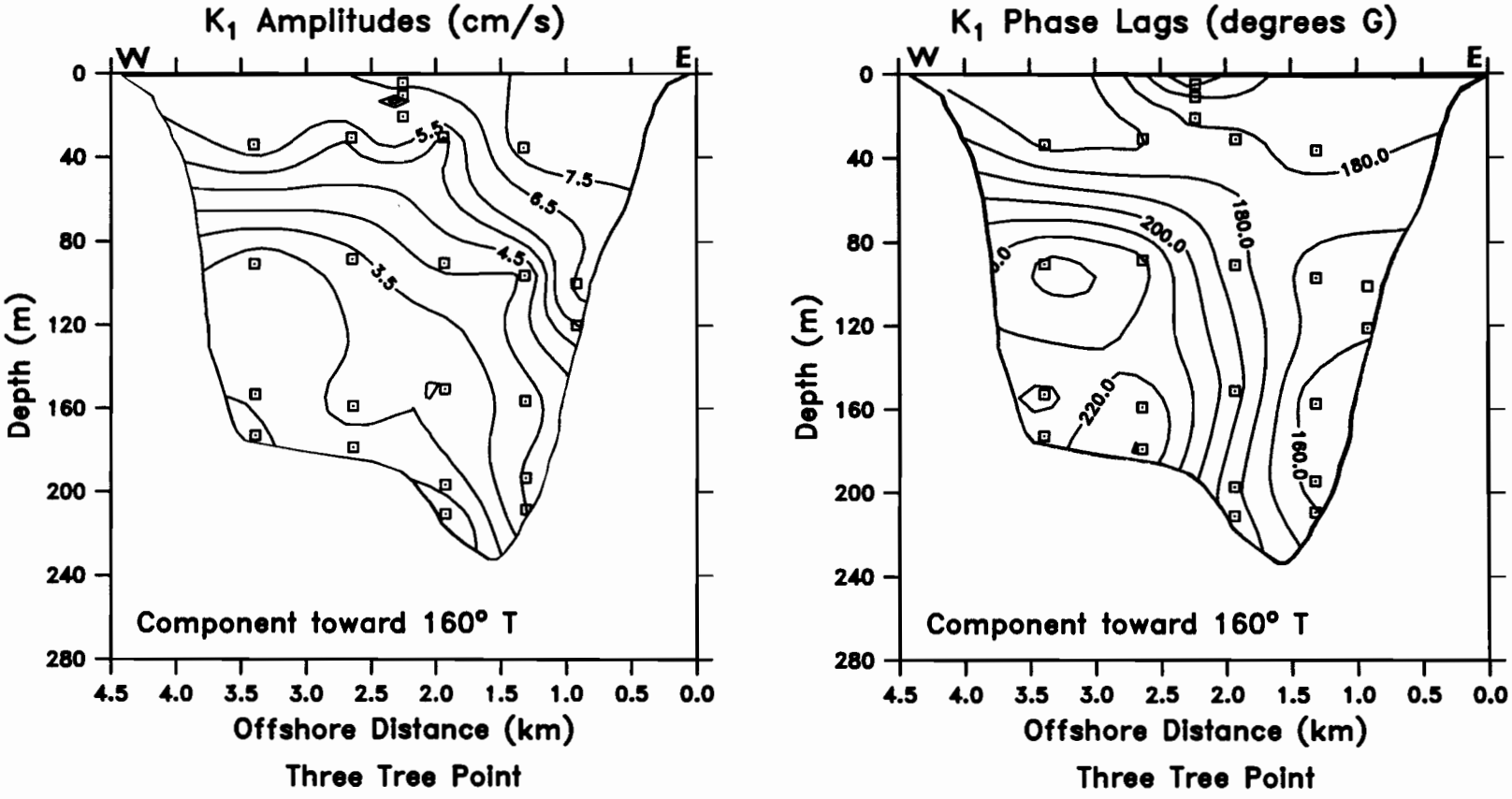

Figure 20: Observed K_1 tidal current amplitudes and phases for a channel cross-section off Three Tree Point. Amplitudes in cm/s and phases in degrees. Phases are Greenwich phase lags for a flood tide. Location of current meters are indicated by squares. Vertical exaggeration is 16:1.

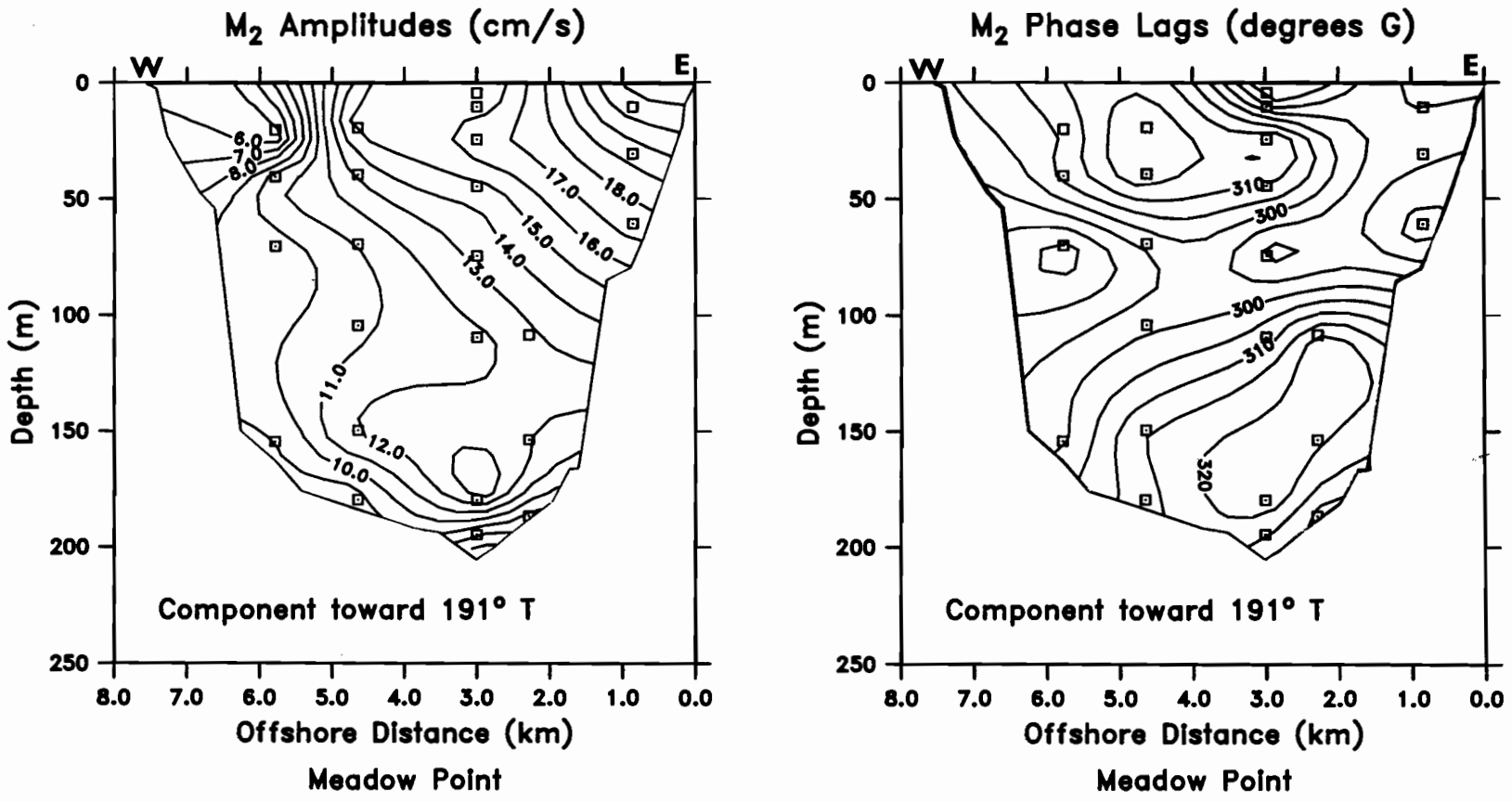

Figure 21: Observed M_2 tidal current amplitudes and phases for a channel cross-section off Meadow Point. Amplitudes in cm/s and phases in degrees. Phases are Greenwich phase lags for a flood tide. Location of current meters are indicated by squares. Vertical exaggeration is 32:1.

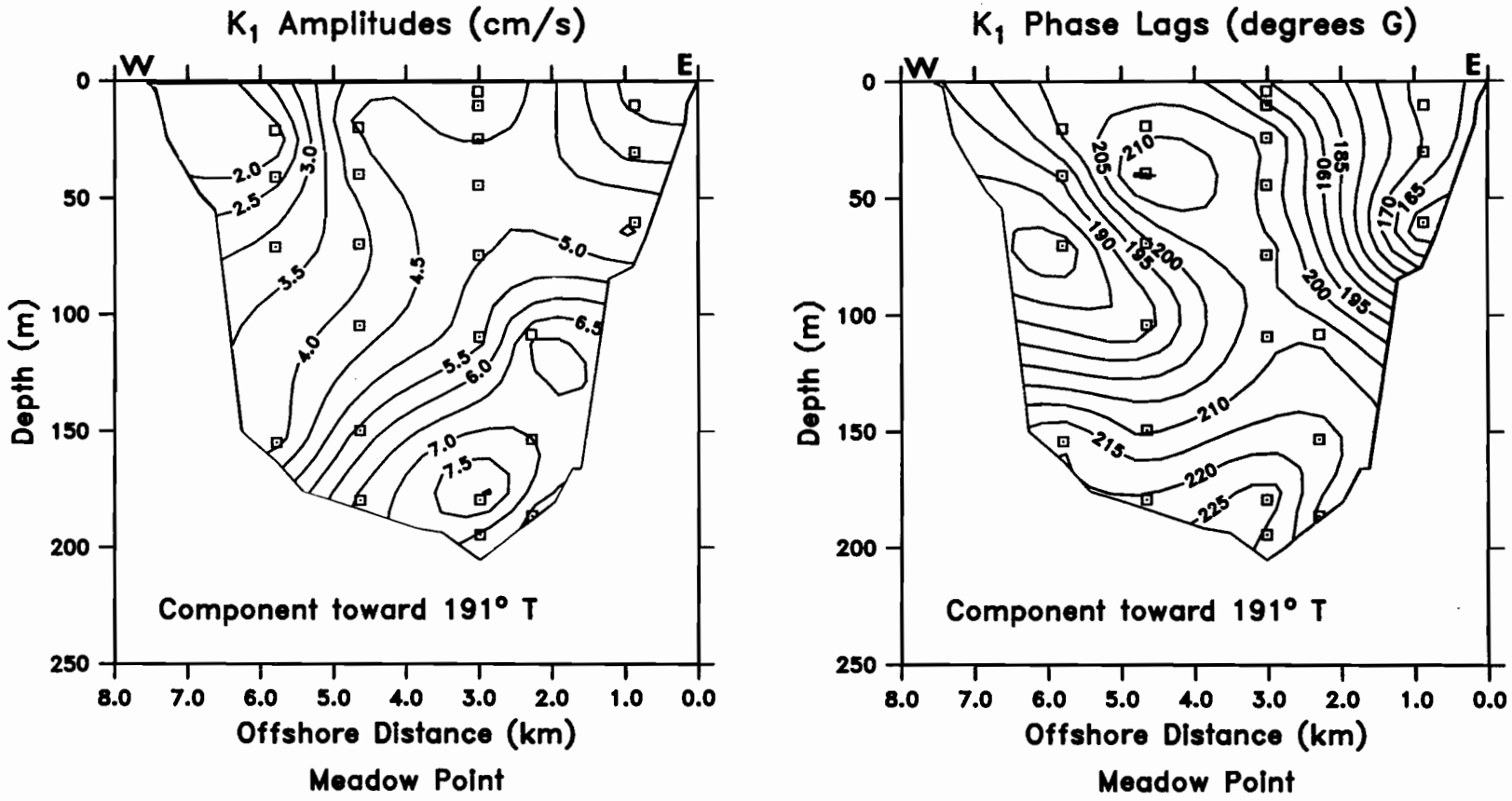

Figure 22: Observed K_1 tidal current amplitudes and phases for a channel cross-section off Meadow Point. Amplitudes in cm/s and phases in degrees. Phases are Greenwich phase lags for a flood tide. Location of current meters are indicated by squares. Vertical exaggeration is 32:1.

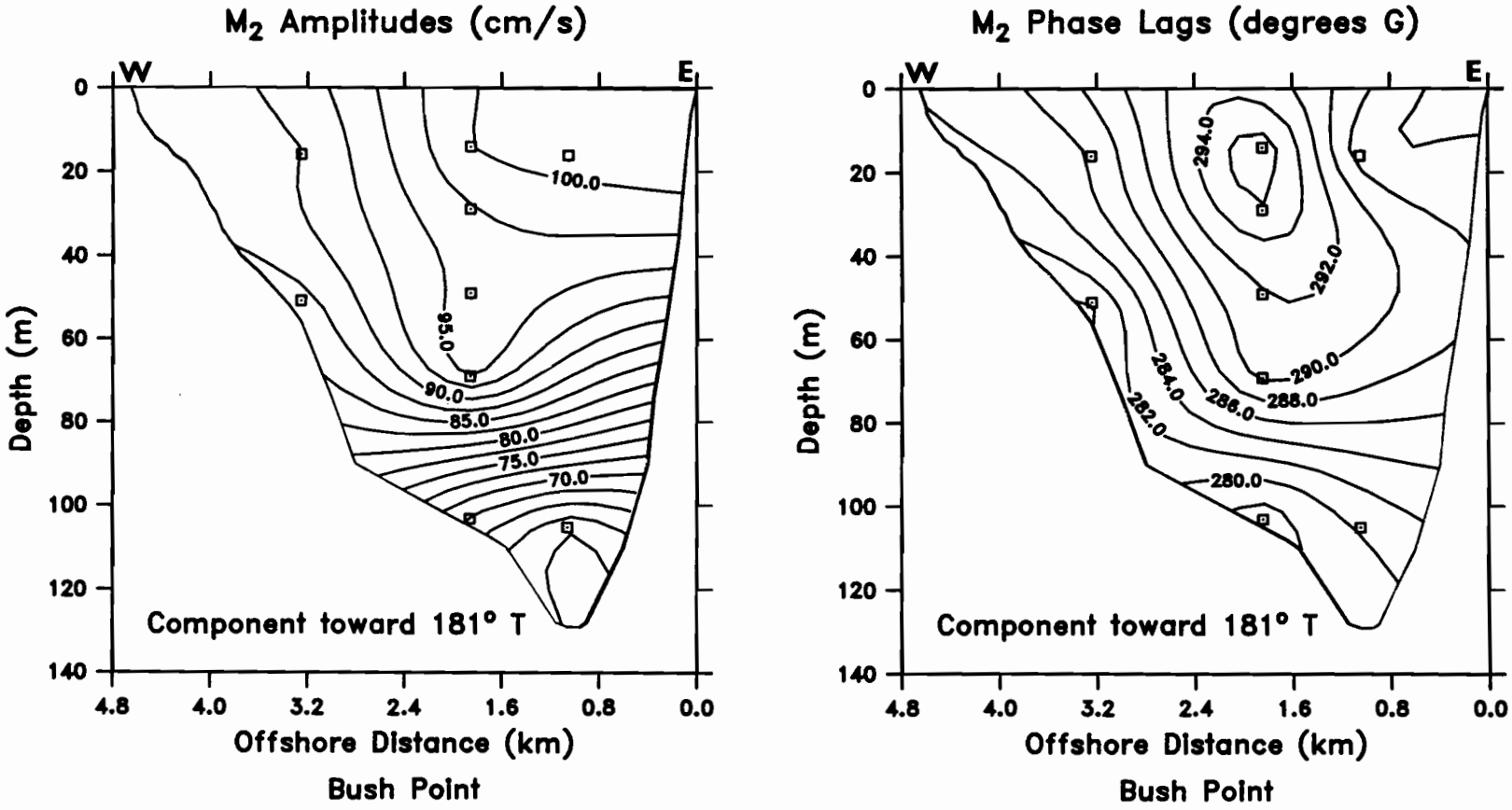

Figure 23: Observed M_2 tidal current amplitudes and phases for a channel cross-section off Bush Point. Amplitudes in cm/s and phases in degrees. Phases are Greenwich phase lags for a flood tide. Location of current meters are indicated by squares. Vertical exaggeration is 34:1.

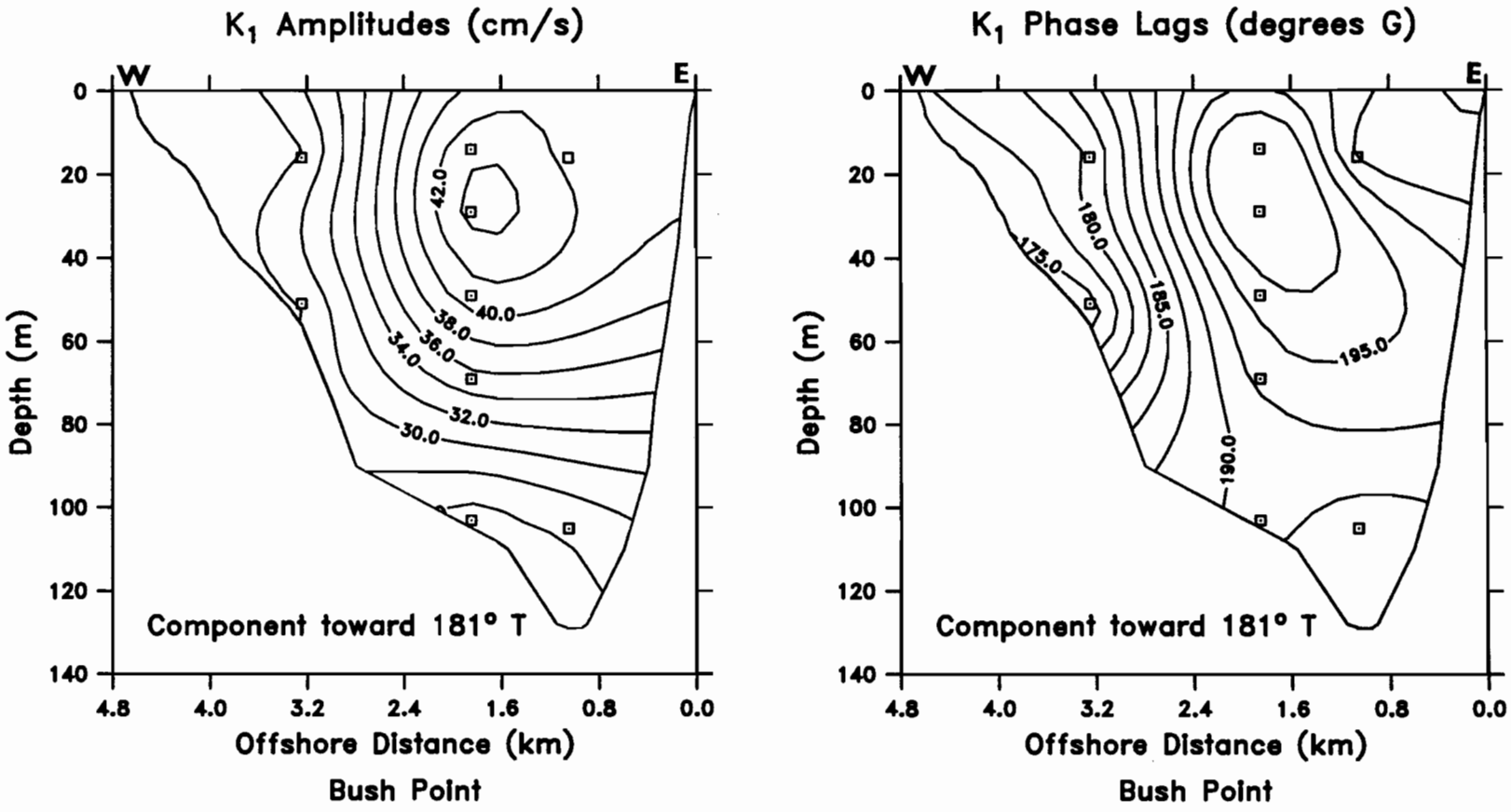

Figure 24: Observed K_1 tidal current amplitudes and phases for a channel cross-section off Bush Point. Amplitudes in cm/s and phases in degrees. Phases are Greenwich phase lags for a flood tide. Location of current meters are indicated by squares. Vertical exaggeration is 34:1.

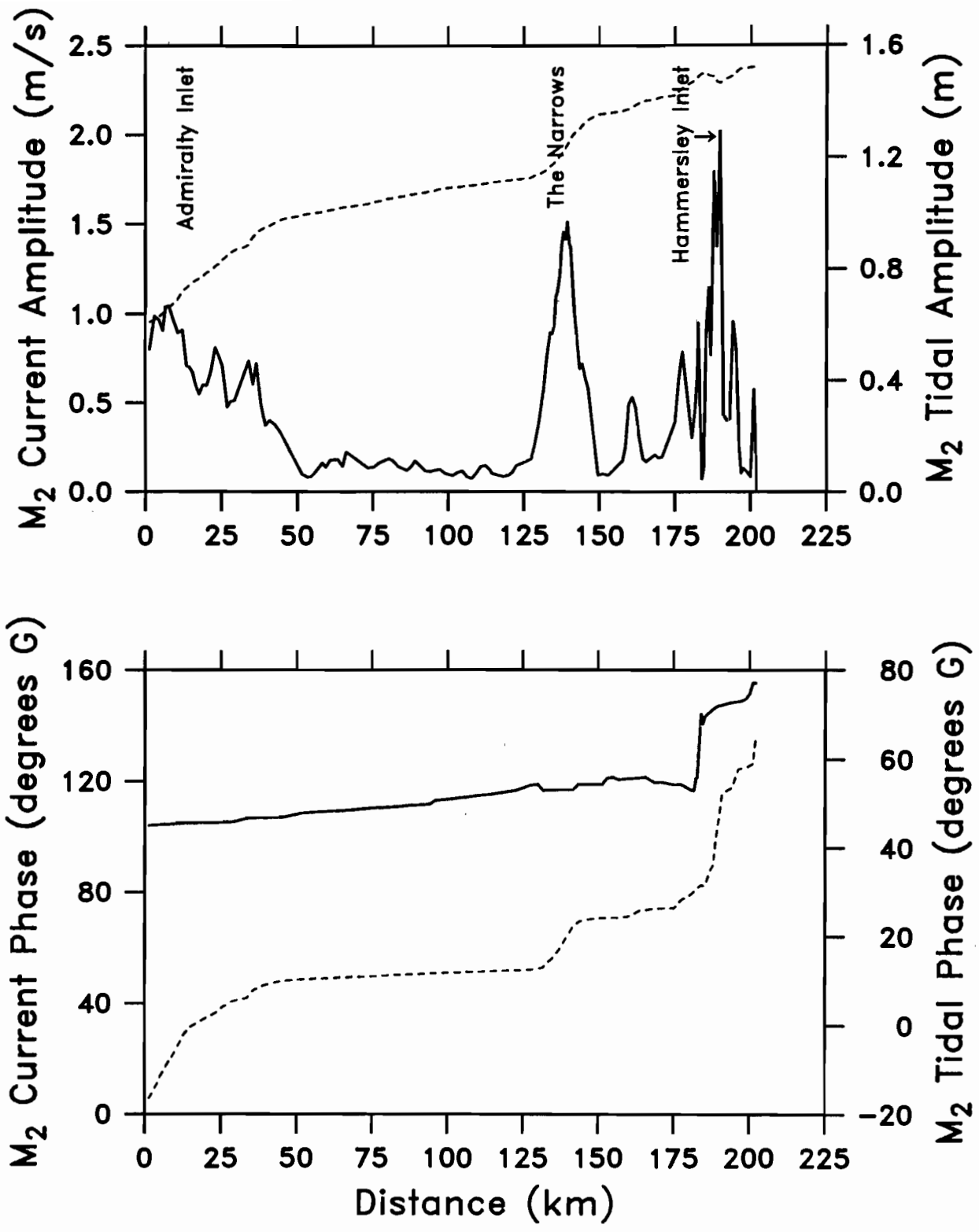

Figure 25: Amplitudes and Greenwich phase lags of the M_2 tide (dashed lines) and cross-sectionally averaged amplitudes and phases of the M_2 tidal current (solid line) down an along-axis transect through Admiralty Inlet, the main basin, The Narrows, and the southern basin into Oakland Bay. Current phases are for the flood direction. Distance is measured from the first model segment near Port Townsend (Fig. 3).

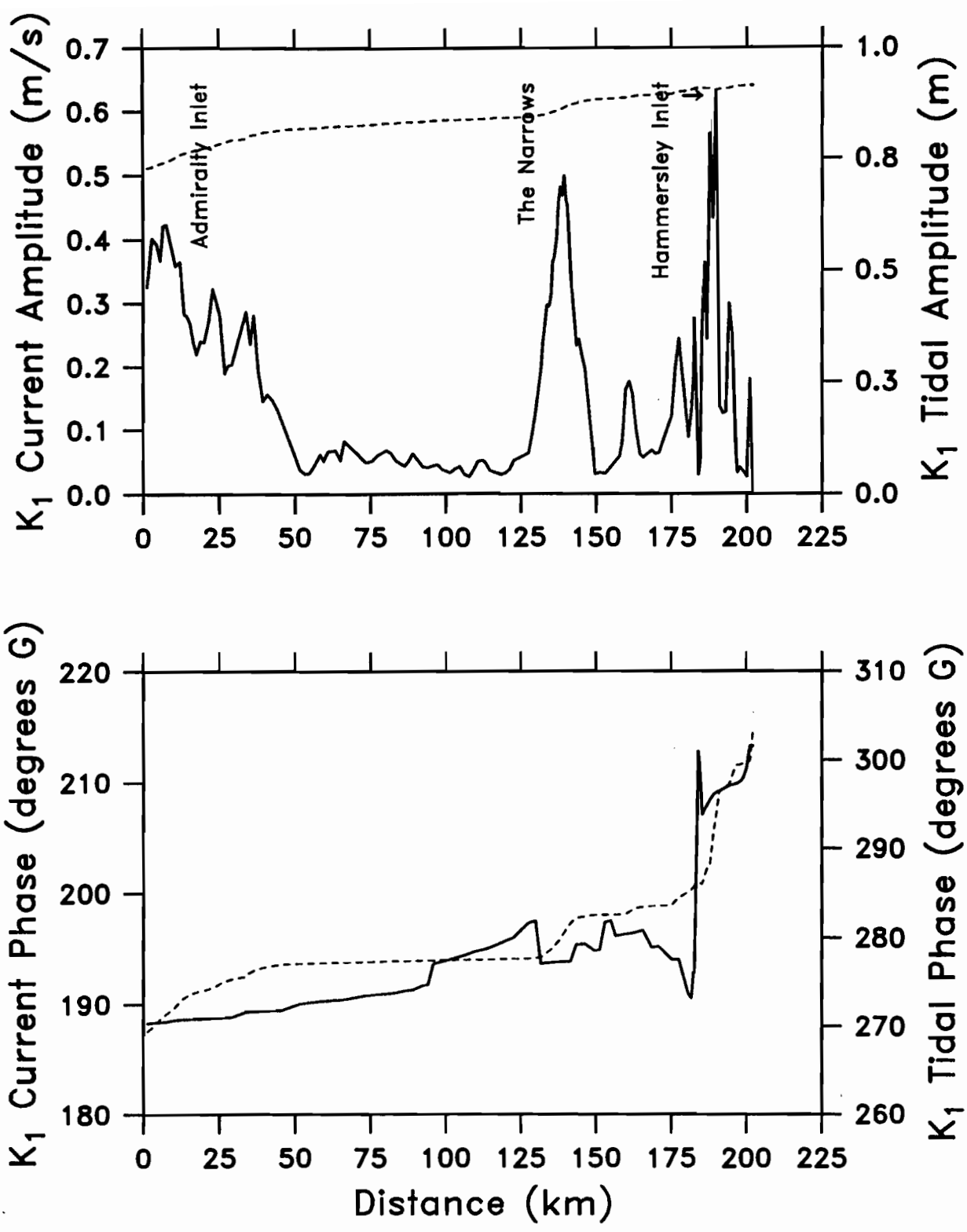

Figure 26: Amplitudes and Greenwich phase lags of the K_1 tide (dashed lines) and cross-sectionally averaged amplitudes and phases of the K_1 tidal current (solid line) down an along-axis transect through Admiralty Inlet, the main basin, The Narrows, and the southern basin into Oakland Bay. Current phases are for the flood direction. Note that the amplitude scales are less than in Fig. 25.

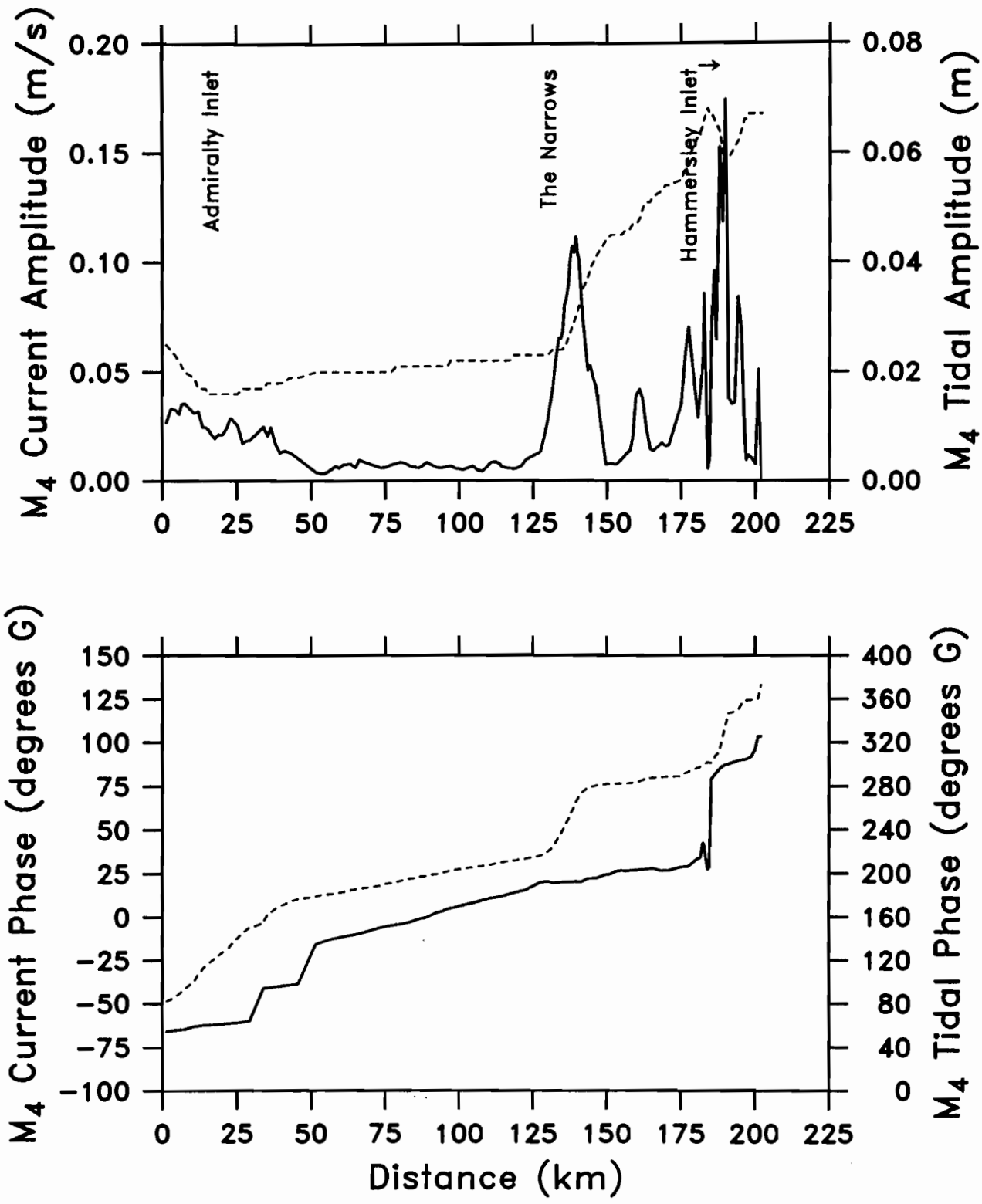

Figure 27: Amplitudes and Greenwich phase lags of the M_4 tide (dashed line) and cross-sectionally averaged amplitudes and phases of the M_4 tidal current (solid line) down an along-axis transect through Admiralty Inlet, the main basin, The Narrows, and the southern basin into Oakland Bay. Current phases are for the flood direction. Note that the amplitude scales are less than in Figs. 25 and 26.

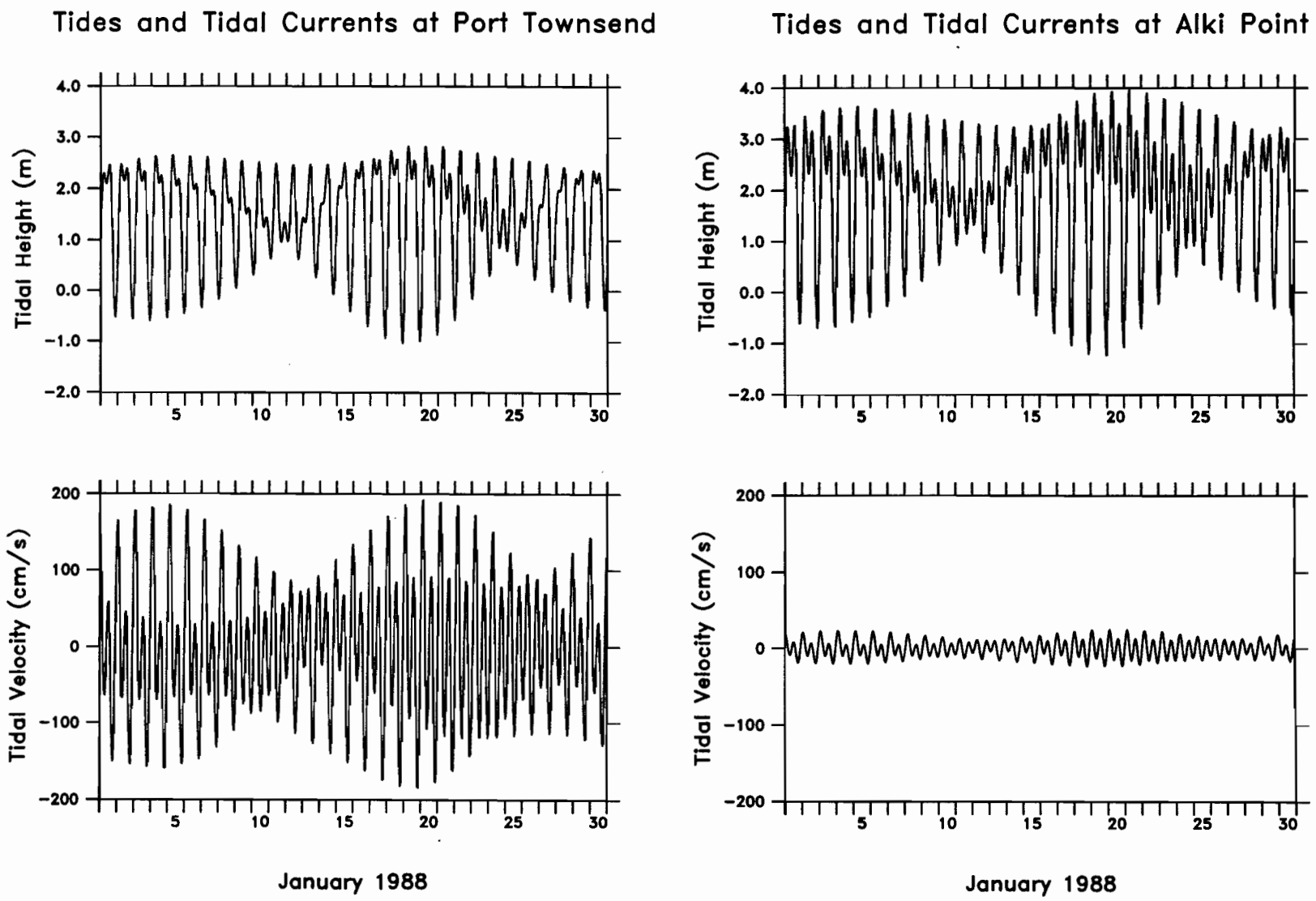

Figure 28: Predicted tidal height and cross-sectionally averaged tidal current velocity during January 1988 a) in Admiralty Inlet near Port Townsend, b) off Alki Point at Seattle.

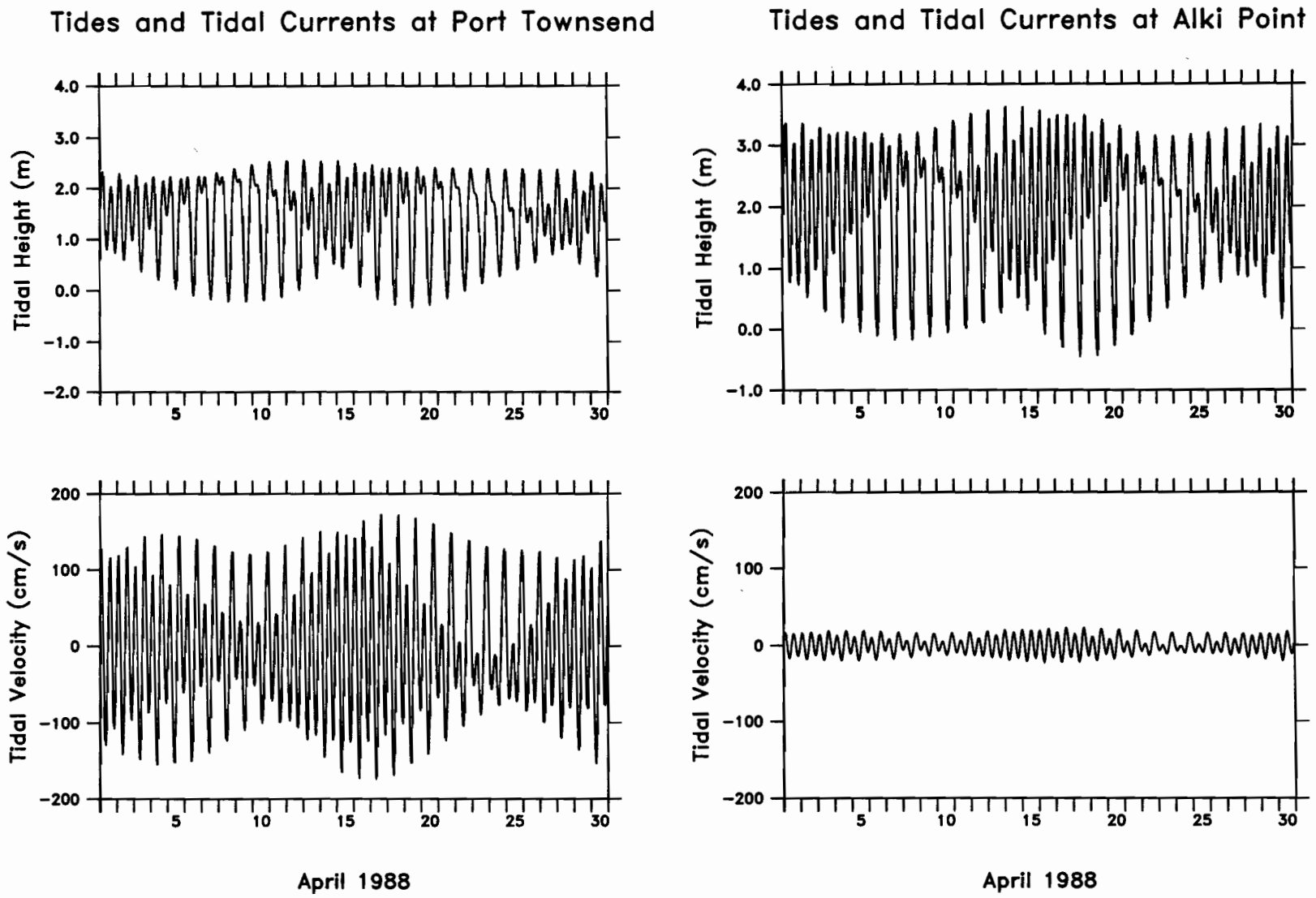

Figure 29: Predicted tidal height and cross-sectionally averaged tidal current velocity during April 1988 a) in Admiralty Inlet near Port Townsend, b) off Alki Point at Seattle.

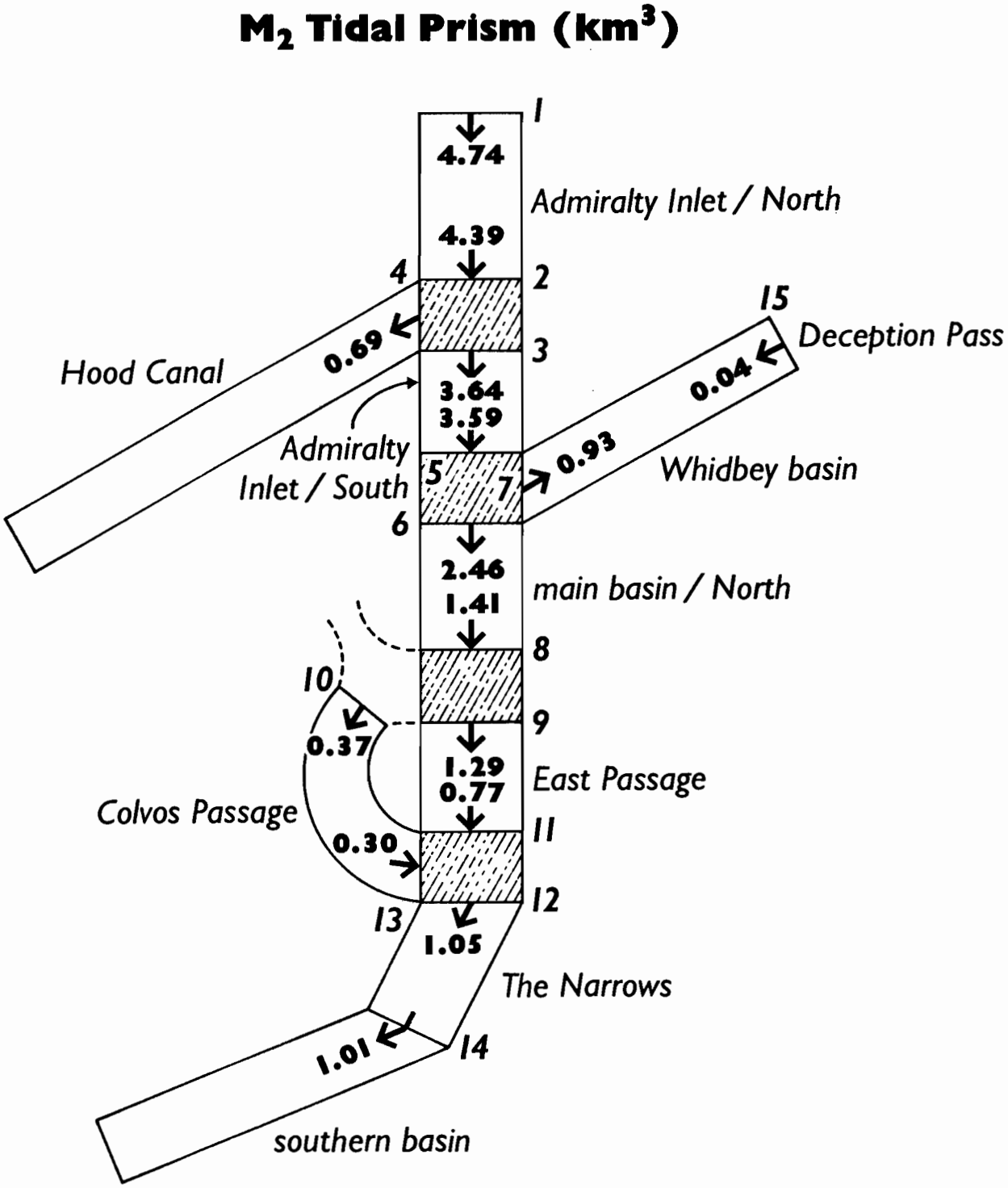

Figure 30: Schematic diagram of the M_2 tidal prism (km^3) from the model landward of the transects indicated.

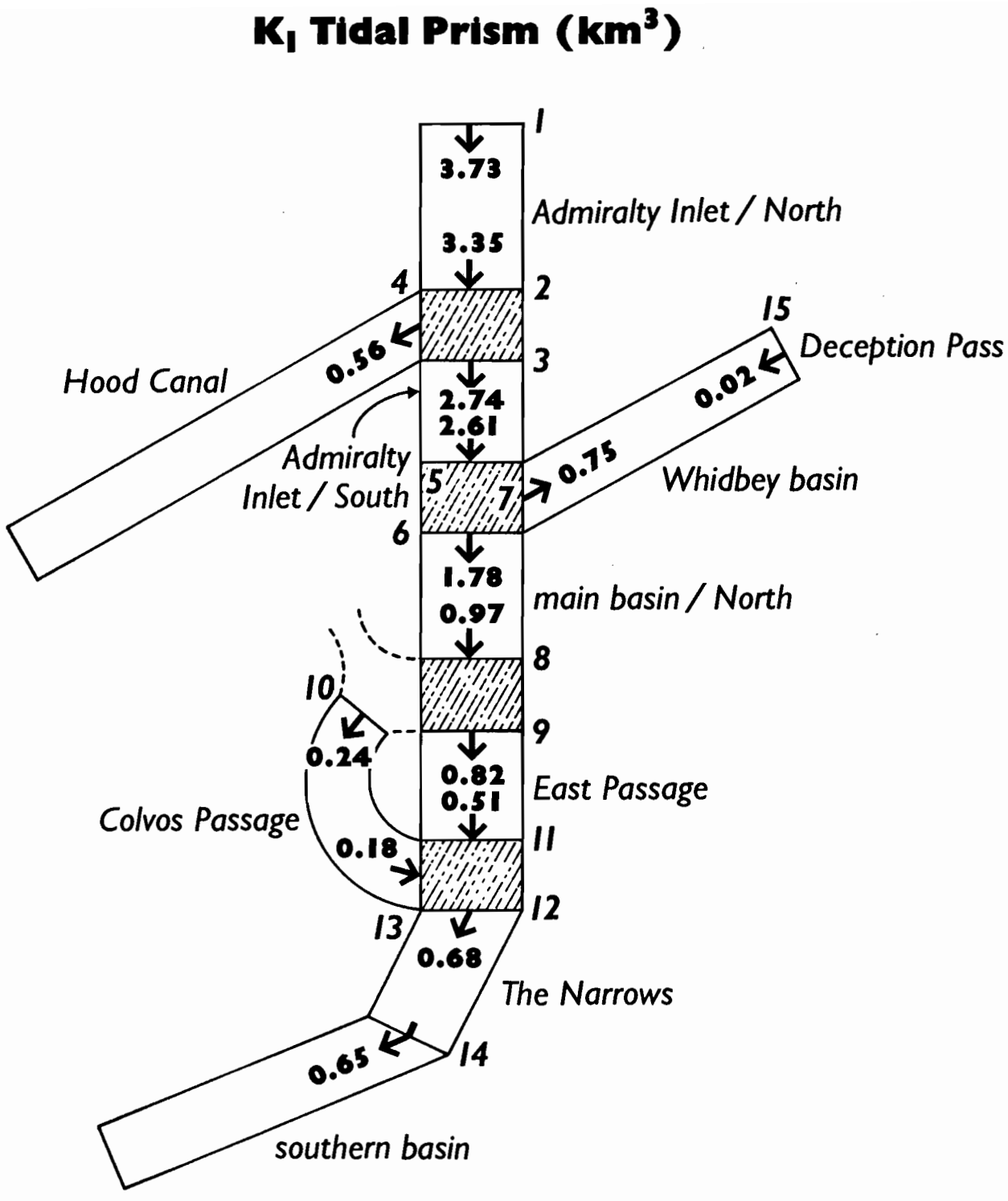

Figure 31: Schematic diagram of the K_1 tidal prism (km^3) from the model landward of the transects indicated.

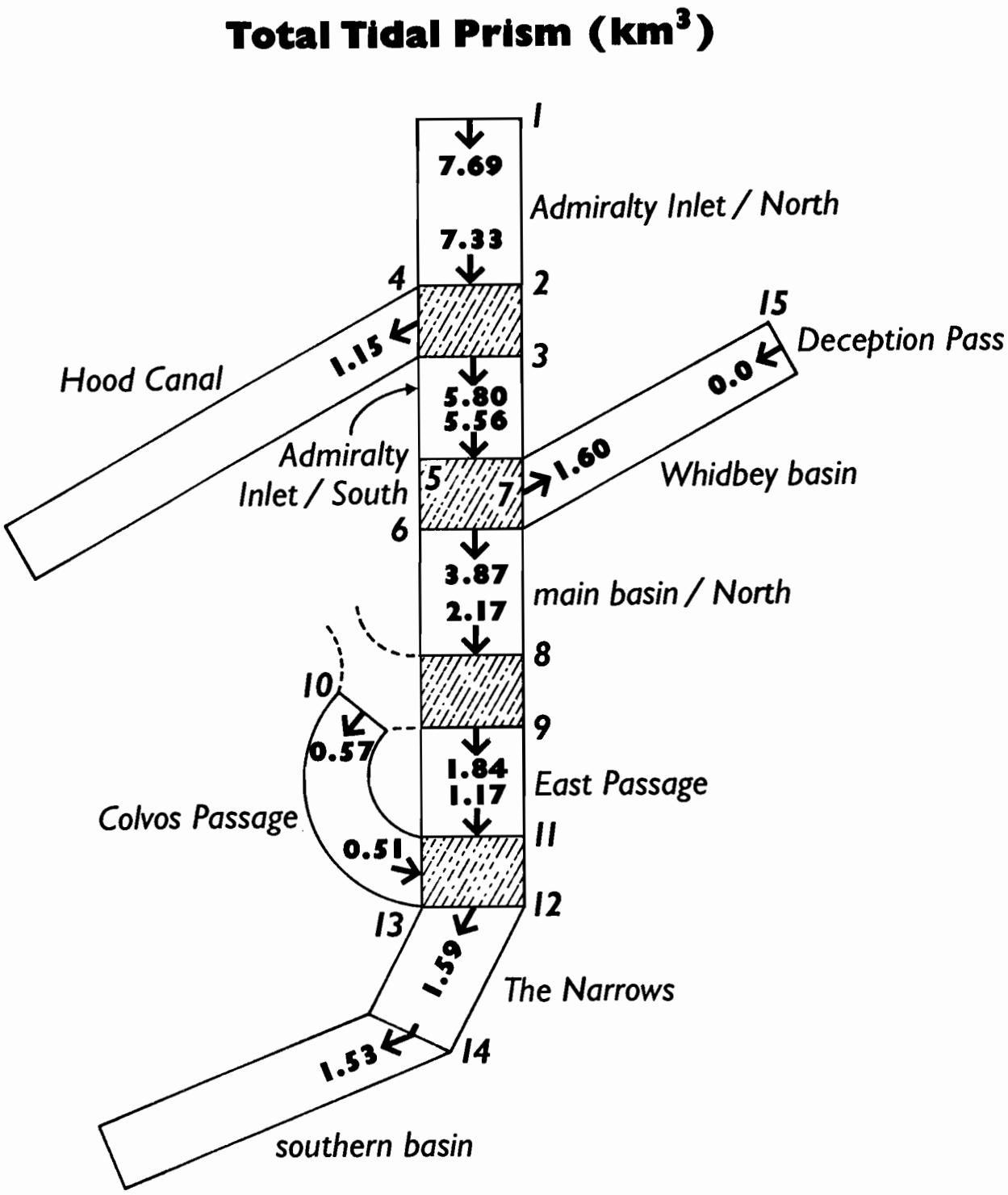

Figure 32: Schematic diagram of the tidal prism (km^3) of the model composite tide landward of the transects indicated.

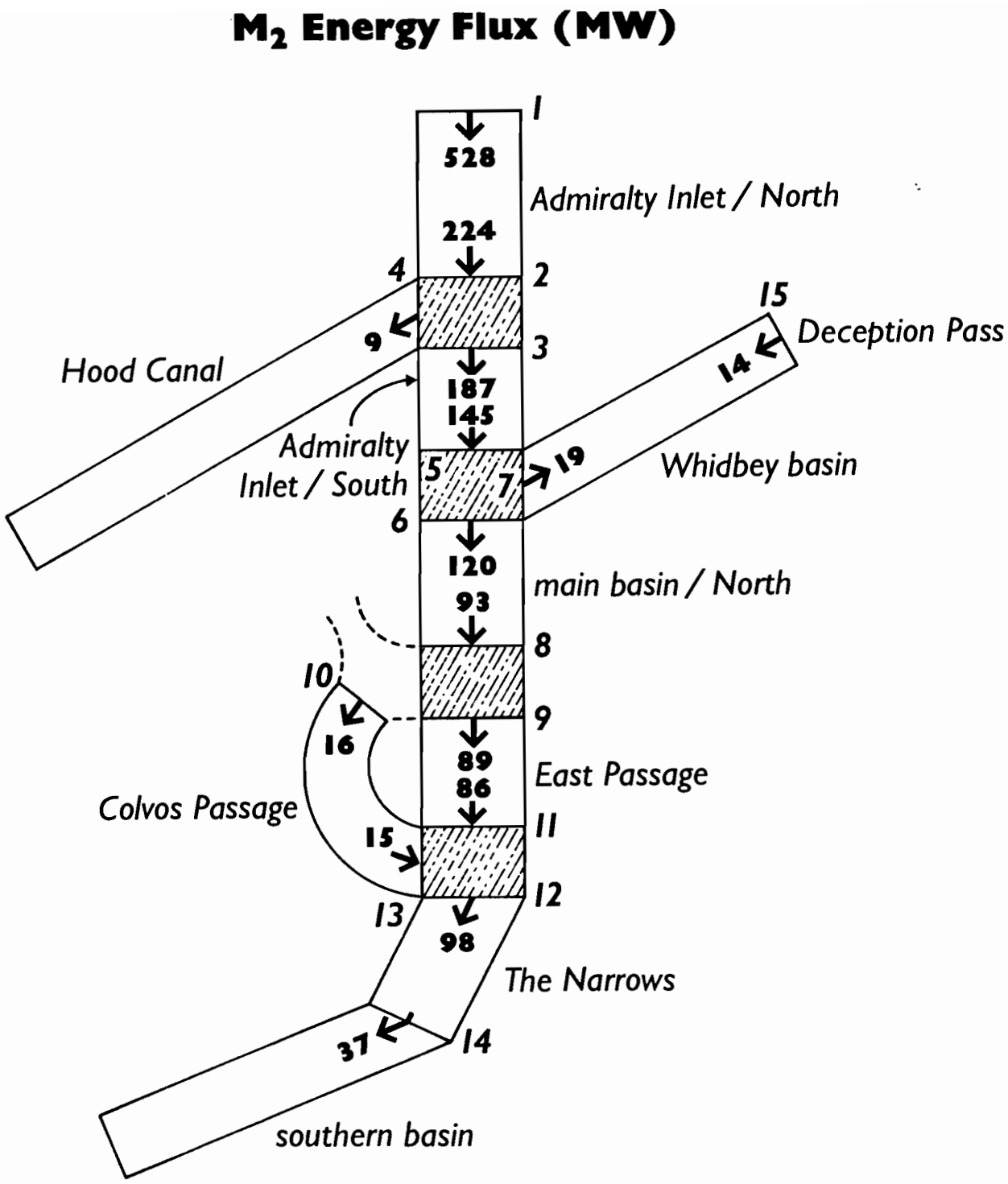

Figure 33: Schematic diagram of the average rate of M_2 tidal energy flux (MW) into the major subregions of Puget Sound. Losses over any section represent tidal energy dissipation by friction.

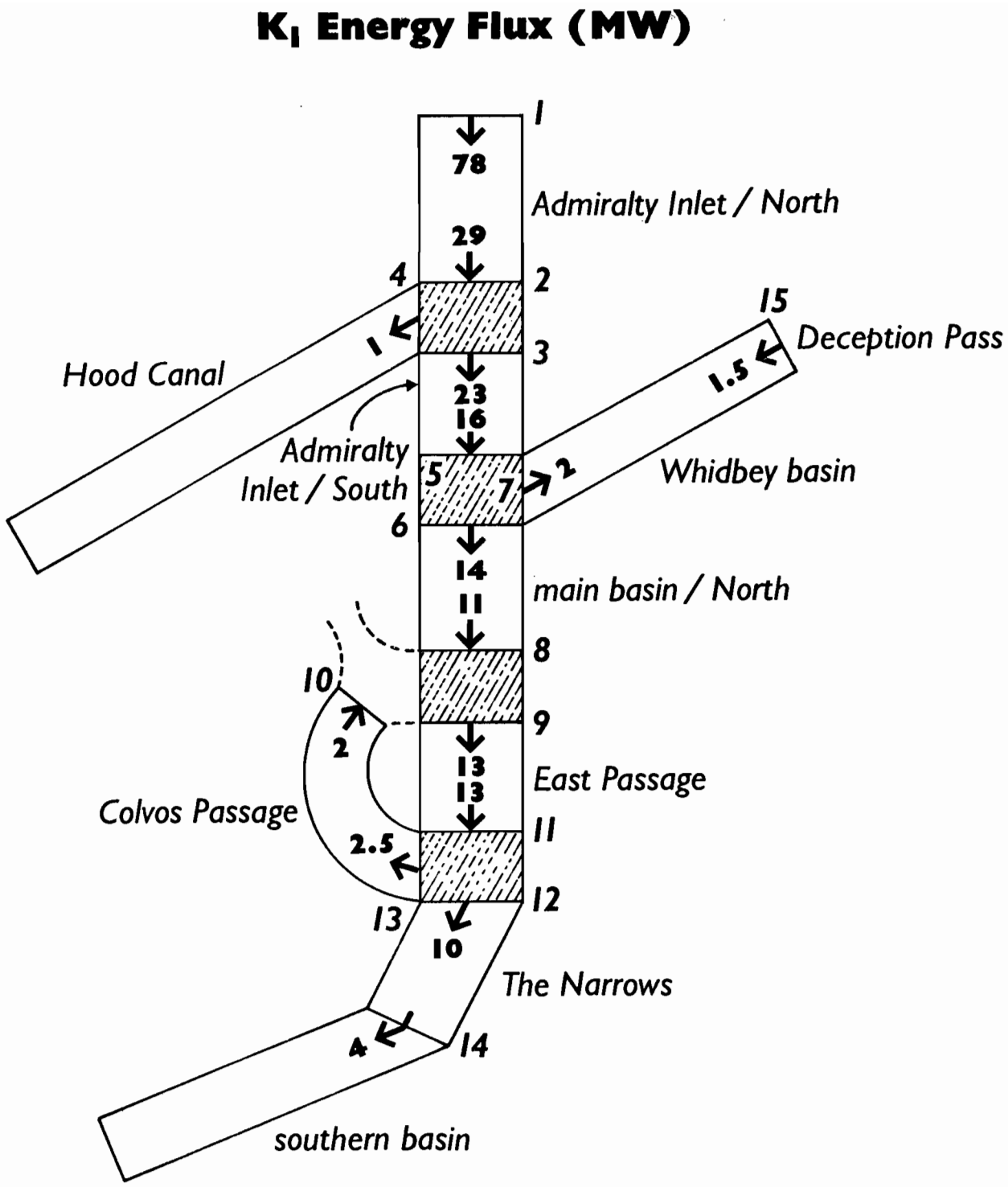

Figure 34: Schematic diagram of the average rate of K_1 tidal energy flux (MW) into the major subregions of Puget Sound. Losses over any section represent tidal energy dissipation by friction.

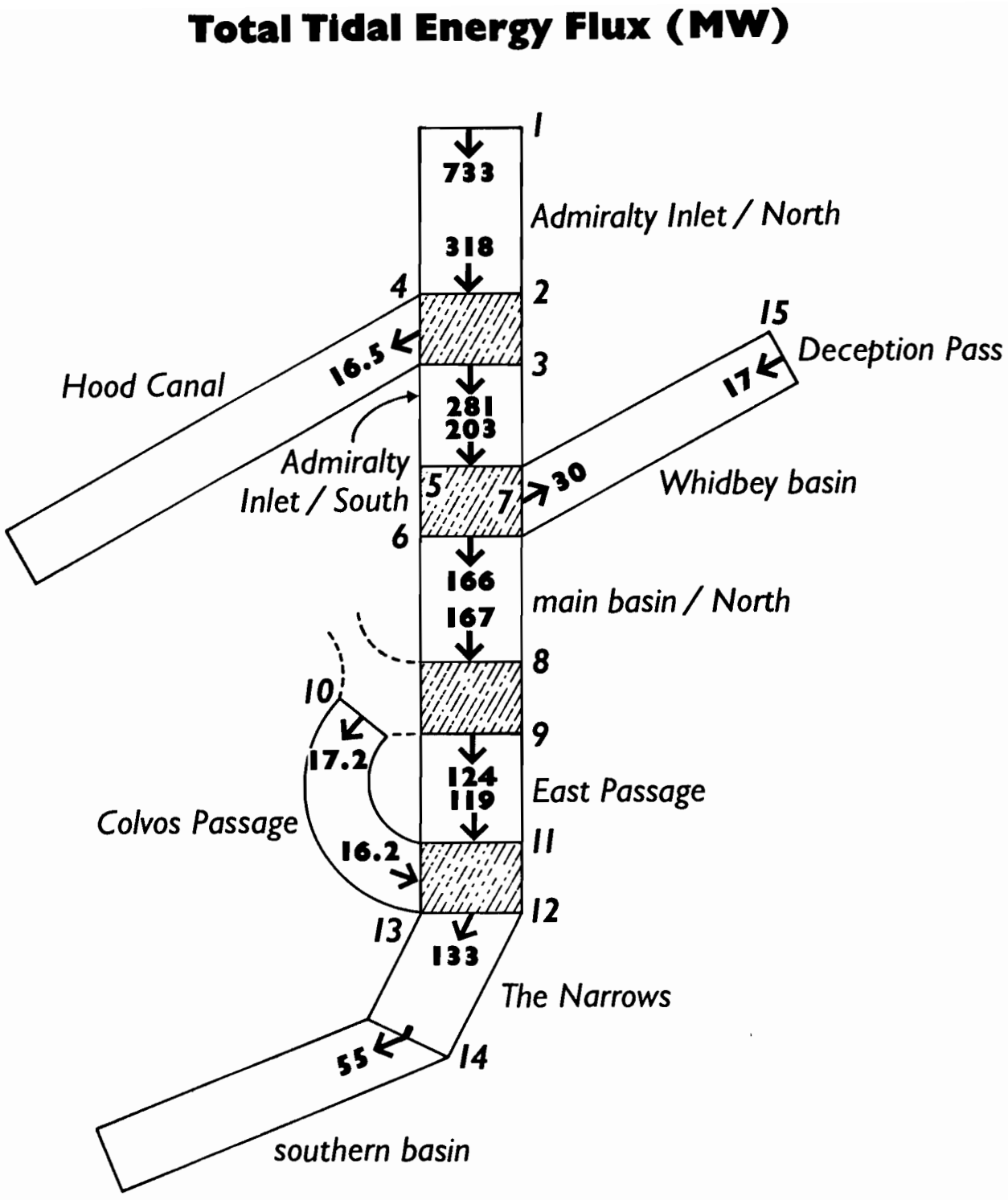

Figure 35: Schematic diagram of the average rate of tidal energy flux (MW) into the major regions of Puget Sound for the model composite tide. Losses over any section represent tidal energy dissipation by friction.

U.S. GOVERNMENT PRINTING OFFICE: 1988 — 673-002/92015